Measurements and Predictions of the Heat Transfer at the Tube-Fin Junction for Louvered Fin Heat Exchangers

Christopher P. Ebeling

Thesis submitted to the Faculty of the Virginia Polytechnic and State University in partial fulfillment of the requirements for the degree of

Master of Science
in
Mechanical Engineering

Dr. Karen A. Thole, Chair
Dr. Brian Vick
Dr. Danesh Tafti

June 13, 2003
Blacksburg, Virginia

Keywords: Compact heat exchanger, Louvered fins, Tube wall

Measurements and Predictions of the Heat Transfer at the Tube-Fin Junction for Louvered Fin Heat Exchangers

Abstract

Compact heat exchangers are usually characterized by a large heat transfer surface per unit of volume. These characteristics are useful when thermal energy between two or more fluids must be exchanged without mixing. Most compact heat exchangers are liquid-to-air heat exchangers, with approximately 85% of the total thermal resistance occurring on the air side of the heat exchanger. To reduce the space and weight of a compact heat exchanger, augmentation strategies must be proposed to reduce the air side resistance. However, before any strategies to augment the air side heat transfer can be proposed, a thorough insight of the current mechanisms that govern air side heat transfer is required.

The tube wall heat transfer results presented in this paper were obtained both experimentally and computationally for a typical compact heat exchanger design. Both isothermal and constant heat flux tube walls were studied. For the experimental investigation, a scaled-up model of the louvered fin-tube wall was tested in a flow facility. Although computational results for the isothermal tube wall are shown, control of the experimental isothermal tube wall proved to be unrealistic and only heat transfer measurements along the constant heat flux tube wall were made. For the constant heat flux tube wall, reasonable agreement has been achieved between the measurements and the steady, three-dimensional computational predictions.

The results of the study showed that high heat transfer coefficients existed at the entrance to the louver array as well as in the louver reversal region. Vortices created at the leading edge of the louvers augmented heat transfer by thinning the tube wall boundary layer. Results indicate that an augmentation ratio of up to 3 times can occur for a tube wall of a louvered fin compact heat exchanger as compared to a flat plate.

Measurements and Predictions of the Heat Transfer at the Tube-Fin Junction for Louvered Fin Heat Exchangers

Preface

Compact heat exchangers are used in a variety of devices where heat exchange must occur between two fluids without mixing. Most compact heat exchanger designs use tubes to carry a liquid, while air passes over external fins attached to the tubes. Currently, the limiting factor in heat transfer performance is the air side thermal resistance. The tube wall, which serves as the boundary between the air and the liquid, has characteristics that could give new insight into possible augmentation techniques. This study is a baseline investigation of the heat transfer that occurs along the tube wall for a typical compact heat exchanger design.

This thesis primarily consists of two sections: a journal article summarizing the results of the investigation and detailed appendices. The main focus of the journal article is to present a comprehensive discussion of both the experimental and computational heat transfer results occurring along the tube wall for a typical compact heat exchanger design. Additional experimental tests and specific detail such as construction techniques used, instrumentation, and recommendations for future study are included in the appendices.

Acknowledgments

There are several people in my life that I wish to thank for helping me through this thesis and degree. First of all, I would like to thank my advisor Dr. Karen Thole for all the guidance and patience she practiced with me. Dr. Thole always had faith in me, especially when challenges seemed overbearing. I have learned an incredible amount from her and I am very thankful for the internship and PhD opportunities she has offered me. I would also like to thank my father, mother, and brother for always supporting me and pushing me to continue my education. You have taught me the value of success and for that I will always love you. To all my dear friends at Gannon University: Ken, Dr. Aggarwal, Sr. Lucille, Mr. Lucky, and JT, thanks for all your encouragement and all the fun times we shared. To my favorite composers, Johann, Wolfgang, and Ludwig, thanks for providing the superb music that helped me get through this thesis. In addition, I would like to thank all my friends at VTExccl, Sac, Eric, Erik, Will, Jesse, Evan, Daniel, Andrew, Joe, William, Erin, and Jeff. I have gained valuable insights from all of you. To my dear girlfriend, Katherine, thanks for all the back massages all those late nights that I worked on this thesis. But on a more serious note, thanks loving me so much and supporting me. I love you. Finally, I have to extend a thank you to Dr. Vick for all the knowledge I gained from his classes and for making the process of learning difficult subject matters fun…also for taking me fishing.

Table of Contents

Nomenclature

A	Louver surface area
$A_{c,f}$	Cross sectional area of a straight fin
F_p	Fin pitch
h	Convective heat transfer coefficient, $h = q'' / (T_w - T_{in})$
$\overline{h_f}$	Average heat transfer coefficient of the first louver (Lyman, et al. 2002)
k_f	Thermal conductivity of the balsa wood
L_p	Louver pitch, length of louver
L_f	Length of the fin
L_{lexan}	Thickness of the lexan tube wall backing
L_{foam}	Thickness of the foam tube wall backing
Nu	Nusselt number based on louver pitch, $Nu = h\ L_p / k$
Nu_L	Average Nusselt numbers of louvers 2-8 (Lyman, et al. 2002)
Nu_o	Baseline Nusselt number given by the flat plate correlation, equation 2 (Incropera and DeWitt, 1996)
P_f	Perimeter of a straight fin
q''_{power}	Applied heat flux boundary condition
q''	Convective heat flux from heated wall
q''_c	Heat flux lost due to conduction
q''_r	Heat flux lost due to radiation
Re	Reynolds number based on louver pitch, $Re = U_{in} \cdot L_p / \nu$
R_p	Resistance of the precision resistor
R_c	Thermal resistance between the conduction guard heater and the tube wall
t	Louver thickness
T_w	Surface temperature of the tube wall (flat plate)
T_{P1}	Surface temperature of the conduction guard heater
T_{P2}	Surface temperature of the radiation guard heater
U_{in}	Inlet face velocity to test section
X', Y', Z'	Fin dimensional coordinate system, see figure 1
X, Y, Z	Normalized fin dimensions, $(X'/L_f, Y'/L_f, Z'/L_f)$

$x',y'z'$	Louver dimensional coordinate system, see figure 11
x,y,z	Normalized louver dimensions, $(x'/L_p, y'/L_p, z'/L_p)$

Greek

θ	Louver angle, non-dimensional temperature (see equations 3, C.1)
ν	Kinematic viscosity
χ_L	Fraction of tube wall-louver radiation losses to applied heat flux (as given by RTE)
χ_W	Fraction of tube wall-lexan wall radiation losses to applied heat flux
ε_L	Emissivity of the louvers
ε_w	Emissivity of the milled lexan wall
σ	Stefan-Boltzmann constant
σ_s	Radiation scattering coefficient of air
ΔT	Temperature difference between strip 1 and the inlet air
η_f	Effectiveness for an infinitely long fin (Incropera and DeWitt, 1996)

Superscripts

$\bar{}$	Averaged value
$'$	Dimensional values

List of Tables

List of Figures

Measurements and Predictions of the Heat Transfer at the Tube-Fin Junction for Louvered Fin Heat Exchangers

Christopher P. Ebeling, Graduate Research Assistant
Virginia Tech, Mechanical Engineering Department
Blacksburg, VA 24061
(540)231-4775
cebeling@vt.edu

K.A. Thole, Professor
Virginia Tech, Mechanical Engineering Department
Blacksburg, VA 24061
(540)231-7192
thole@vt.edu

Submitted for review to the International Journal of Compact Heat Exchangers, May 2003

Measurements and Predictions of the Heat Transfer at the Tube-Fin Junction for Louvered Fin Heat Exchangers

Abstract

The dominant thermal resistance for most compact heat exchangers occurs on the air side and thus a detailed understanding of air side heat transfer is needed to improve current designs. Louvered fins, rather than continuous fins, are commonly used to increase heat transfer by initiating new boundary layer growth and increasing surface area. The tube wall from which the fins protrude has an impact on the overall heat exchanger performance. The boundary layer on the external (typically, air) side of the tube is subjected to repeated interruptions at the louver-tube junction. This paper discusses baseline results of a combined experimental and computational study of heat transfer along the tube wall of a typical compact heat exchanger design. A scaled-up model of a multi-louver array protruding from a heated flat surface was used for the experiments. The results of this study indicate reasonable agreement with steady, three-dimensional computational predictions.

1. INTRODUCTION

Understanding the mechanisms that dominate heat transfer in a louvered fin heat exchanger provides the potential for reducing the heat exchanger's size and weight. This reduction in size can clearly benefit many industries, including transportation, heating, and air conditioning. Because more than 85% of the total thermal resistance in a typical air-cooled heat exchanger occurs on the air side, the performance of compact heat exchangers depends highly on the heat transfer occurring on the air side.

Louvered fins, rather than continuous fins, are commonly used in compact heat exchangers to break up boundary growth along the fins and increase the air side heat transfer surface area. The increase in surface area results because of the fin thickness that is exposed as a result of the louvers being stamped out of the fins. Figure 1 illustrates a typical compact heat exchanger geometry comprised of louvered fins, where air passes along, and tubes, where water passes through. Unlike most studies concerning louvered fin heat exchangers, this study focuses on the spatial details of the flow and local heat transfer of these louvers at the louver-tube junction. The louver-tube junction influences compact heat exchanger performance in two ways: first the tube wall provides approximately 10% of the total heat transfer surface area, and second, the tube wall boundary layer governs a portion of the fin heat transfer near the junction. Even though the tube wall consists of only 10% of the total heat transfer surface area, several geometric aspects of the tube-fin junction serve to reduce resistance on the air side. Unlike continuous fins, louvered fins interrupt the boundary layer growth along the tube wall, which could be thought of as a flat plate. Generally, the aspect ratio of the tubes is such that the tube wall boundary layers do not intersect and the flow can be thought of as an external flow. The interruption of the louvers governs the thickness of the tube wall boundary layer and affects the tube wall heat transfer as well as fin performance near the junction.

This paper presents results of a combined experimental and computational study of tube wall heat transfer with the wall being subjected to boundary layer interruptions from the louvered fins. The experiments were performed in a test rig with a scaled-up model of the louver-tube junction, which was simulated as a heated flat plate with nearly adiabatic louvers protruding from the plate. Studies were performed for one louver fin geometry, specifically for a ratio of fin pitch to louver pitch of $F_p/L_p = 0.76$ at a louver angle of $\theta = 27^o$ and Reynolds number range of $230 < Re < 1016$ where Re is based on the inlet velocity and the louver pitch.

1.1 Literature Review

The overall performance of various compact heat exchanger geometries are found in a large number of publications. Since the majority of this data focuses on heat exchangers as an entire system, ε-NTU and LMTD methods are often applied. Kays and London (1984) compiled overall performance data, including heat transfer and pressure drop, for a large number of commercial heat exchangers. While this compilation is extremely useful to heat exchanger companies, the data does not present details on the individual flow field and heat transfer mechanisms that occur within each heat exchanger design. A few studies will be highlighted in this section, which provide insights as to the important mechanisms affecting the louver heat transfer.

Most studies that have evaluated the details of heat transfer for a louvered surface have been completed in two-dimensional test rigs whereby the area of interest has been along the louver surface itself. Beauvais (1965) performed detailed experiments with the use of smoke visualization and showed how the louvers direct the air flow under certain conditions and geometries (louver directed) as opposed to the flow being axially directed. The experiments of Beauvais disposed of the idea that the main flow direction was axial and that the louvers only acted as rough surfaces within the main flow. By repeating Beauvais' experiments, Davenport (1983) was able to show the degree to which the flow is louver directed. Davenport noticed that louver directed flow is a function of Reynolds number. At low Reynolds numbers, the flow tended to remain axially directed, whereas at higher Reynolds numbers the flow tended to become louvered directed.

In general, later studies of Webb and Trauger (1991) identified that the flow tends to be louver directed at high Reynolds numbers, low louver angles, and large fin pitches. Achachia and Cowell (1988) investigated overall heat transfer and friction factors for a large range of louvered fin geometries. They found that at Reynolds numbers below 200, heat transfer performance flattened off considerably. This tendency was attributed to the flow remaining axially directed. In contrast, as the flow becomes louver directed at high Reynolds numbers, the overall average heat transfer coefficients increase above that of the axially directed flow.

Fewer studies have addressed three-dimensional effects in louvered fins relevant to compact heat exchangers. Flow visualization studies by Namai, et al. (1998) were completed in which three-dimensional fin models were used. These three-dimensional models included several different geometries at the tube-wall junction. Their overall conclusions were that there are strong three dimensional characteristics in louvered fin flows. Atkinson, et al. (1998) performed computational simulations of both two and three-dimensional models whereby the three-dimensional model included the effects of the tube. Their results indicated that the three-dimensional models gave predictions that were in better agreement with experimental observations of both pressure losses and heat transfer reported by Achachia and Cowell as compared with their two-dimensional predictions. Tafti, et al. (2000) solved three-dimensional computational models of multilouvered fins for a fully-developed flow and predicted a number of interesting flow features at the tube-wall junction. Their study incorporated a geometric transition zone between the louver and the tube wall that served to produce vortices such that the heat transfer was increased along the louver. In later studies, Taft and Cui (2002) investigated the effects the transition zone had on tube wall heat transfer. It was found that by creating a high energy vortex jet, the transition zone significantly increases tube wall heat transfer. As an extended study, Taft and Cui (2003) repeated their previous investigation into the transition zone's impact on the heat transfer at the tube wall for four different geometries. Their baseline geometry was composed of a straight louver-tube junction with no transition zone, similar to the geometry studied in this investigation. However, the studies of Taft and Cui (2002 and 2003) consider only fully-developed flow conditions and ignore the effects at the entrance, reversal, and exit louvers.

Since the performance of compact heat exchangers is directly governed by the air side flowfield, it is important to understand the fluid structures that exist. Because publications of the heat transfer in the developing regions along the tube wall with protruding fins are non-existent, the work presented in this paper was warranted.

2. EXPERIMENTAL METHODOLGY

The studies discussed in this paper were performed on a louvered fin and tube design as was illustrated in figure 1 and summarized in table 1. Louvered fins are typically stamped and bent to meet the design louver angle (θ), louver pitch (L_p), and fin pitch (F_p) before being attached to the tube. Once attached to the tubes, the ends of the louvers create the tube-fin junction. Our model does not include any type of transition from the louver to the tube wall, but rather a direct contact between the louver and tube wall.

The flow facility used for the study, except for the test section, was identical to the set-up reported by Lyman et al. (2002). As shown in figure 2, the flow facility primarily consisted of an inlet contraction, a louvered fin test section, a laminar flow element, and a centrifugal blower.

The inlet contraction, which had a 16:1 area reduction, was designed through the use of computational fluid dynamics (CFD) simulations in which the goal was to provide a uniform velocity profile at the inlet to the test section. This uniformity was verified through laser Doppler velocimeter measurements by Lyman (2000). A variable speed centrifugal blower located at the exit of the test rig provided the flow through the test rig with the speed of the blower being controlled using an AC inverter. The flow rate was measured using a laminar flow element (LFE) located just downstream of the test section.

The louvered fin test section, which was designed to measure the heat transfer along a wall with protruding louvers, was constructed as shown in figure 3. Note that this test section is designed to follow the flow path, which was shown to be primarily louver directed, such that an infinite stack of louvers are simulated (Springer and Thole, 1998). Balsa wood louvers, painted silver, were used to reduce any conduction and radiation losses from the wall heat transfer surface. The silver paint used to coat the balsa wood louvers and the black paint used to coat the tube wall had emissivities of 0.3 and 0.98, respectively (Siegel and Howell, 1981). The louvers were held in position by inserting them into milled slots in a lexan wall on one side of the test section and inserting them into specially designed, low thermal conductivity lexan plugs glued onto the heat transfer surface on the other side of the test section. Glued plugs, rather than slots, were needed on the side having the heat flux surface because the foils on that surface could not be slotted. The louvered fin plugs were made of lexan and held balsa wood louvers at the tube wall. The combination of lexan plugs and balsa wood louvers provided reduced heat loss through the louvers at the louver-wall junction. Defined as $\eta_f = \left(k_f P_f / \bar{h}_f A_{c,f}\right)^{1/2}$, the fin effectiveness for an infinitely long fin was calculated to ensure losses through the fin were negligible. The infinitely long fin assumption was valid since CFD studies predicted that 85% of the louver's width was outside the tube wall's thermal boundary layer. For the smallest averaged heat transfer coefficients along the louver, $\bar{h}_f$ (Lyman et al. 2002), the fin effectiveness for Re = 230 and 1016 were η_f = 2 and 1.8, respectively. These values represent the largest fin efficiencies expected within the test section. Since the use of fins are rarely justified unless $\eta_f > 2$, it was assumed that balsa wood fins were ineffective in conducting heat from the tube wall.

A constant heat flux boundary condition was placed on the experimental tube-wall by using heating foils, as was indicated in figure 3. This heated surface started at the leading edge of the entrance louver, where X = 0. To create the heat transfer surface, we attached stainless steel foil heaters to a lexan sheet with double-sided tape. Each strip heater was cut from 0.0508 mm thick grade 316 stainless steel foil with nominal electrical resistance of 74 μΩ-cm. To ensure uniform current distribution through the foils and provide a terminal for lead wires soldered copper bus bars 1.58 mm thick were soldered to the foil. The tube wall required twenty foil heaters having a width of 28 mm and height of 295 mm to completely cover the flat wall from entrance to exit louver. All strip heaters were connected in series to provide a constant current through the heater circuit. The resistances of the strip heaters were calculated by applying a current to the foils and measuring the resulting voltage drop. 20 different foils were sampled showing that each had a nominal resistance of R = 0.14 Ω ± 1%. We considered the power output to be equal as a result of this resistance uniformity. Current through the heater circuit was determined by measuring the voltage drop across a precision resistor, R_p =1Ω ± 1%, connected in series with the heater circuits. Knowing the voltage drop and resistance, the total power dissipated was calculated. The surface area of the strips was also known thereby providing the known total heat flux from the strips.

To minimize the effects of heat losses due to conduction and radiation, two guard heaters were included in the test section design. Both guard heaters consisted of two patch heaters taped to an aluminum plate that was encased in an insulating wooden box. The aluminum plate served to spread out any temperature gradients that might have existed between the patch heaters. Each guard heater was instrumented with thermocouples located at the same wall location as the center thermocouples on the heat transfer surface. Power to the guard heaters was adjusted to insure that the guard heater temperatures were set as close as possible to the tube wall temperature. In this manner, both the heat conduction and radiation losses were minimized within the experimental facility. Radiation losses to both the louver surfaces and the milled lexan wall were reported as fractions of the applied tube wall. From the computational predictions, the fraction of the louver radiation losses to total applied heat flux, χ_L, was used to account for radiation losses to the louvers. Radiation losses to the milled lexan wall were based on the view factor between the two parallel walls. The fraction of radiative heat loss to the milled lexan wall is represented by χ_w. A simple one-dimensional energy balance, shown as equation 1, sums the applied heat fluxes and losses.

$$q'' = q''_{power} - q''_c - q''_r = \frac{I^2R}{A_t} - \left[\frac{T_w - T_{p1}}{R_c}\right] - \left[q''_{power}(\chi_w + \chi_L)\right] \qquad (1)$$

Since the goal of the experimental measurements was to minimize the conductive heat losses, the purpose of the conduction guard heaters were to minimize the temperature difference $T_w - T_{p1}$, thereby causing the applied heat flux to be removed entirely by convection along the tube wall. Temperatures along the aluminum plate (shown in figure 3), were recorded. For all Reynolds numbers tested, the fraction of lost heat flux due to conduction ranged from 1% to 10% along the tube wall. This minimal loss was achieved by adjusting the power input to the conduction guard heater until the temperature difference between the tube wall and the guard heater was minimal. In a similar manner, radiation losses to the milled lexan wall were minimized by adjusting the power to the radiation guard heater. The view factor between the tube and the milled lexan wall was determined to be negligible by experimentally studying the tube wall temperature response to the radiation guard heater. Radiation losses were therefore highly dependent on the numerical estimation of χ_L, which is further discussed under the computational methodology section of this paper.

Type E thermocouples, placed beneath the foil, provided surface temperature measurements. High thermal conductive paste that is electrically insulating was used to insure contact between the foil and the thermocouples without reducing the integrity of the thermocouple measurements. The thermal resistance across the heater foils and paste was calculated to be negligible. Thermocouples used for the reported heat transfer coefficients were positioned in the center of the channel, shown as black dots in figure 4, while periodicity was checked by recording the temperatures above and below the center thermocouples, shown as red dots in figure 4.

The thermocouples were accurately calibrated relative to one another in an ice bath and at room temperature. Thermocouple biases remained constant to within 0.19 ^{o}C over a temperature range of 25 ^{o}C. Data acquisition hardware used to acquire the thermocouple voltages consisted of a National Instruments SCXI-1000 chassis into which three SXCI-1102 modules were inserted. An SXCI-330 terminal block was inserted into each of the modules. The data sample size to compute the mean temperatures consisted of 100 data points, which were acquired after the test surface came to steady state. It typically took 3 hours for the test section to reach steady state.

The uncertainties of experimental quantities were estimated by using the method presented by Moffat (1988). The uncertainty was calculated by acquiring the derivatives of the desired variable with respect to individual experimental quantities and applying known uncertainties. The combined precision and bias uncertainty of the individual temperature measurements was ± 0.19 ºC, which dominated the other uncertainties. The uncertainties in the Nusselt numbers for the Re = 230 was 8% at strip 1, which fell to 4.8% at strip 20. The reduction in uncertainty is contributed to a larger temperature difference between the tube wall and free stream as the tube wall boundary layer develops along the X-direction. Similarly, for the Re = 1016 flow condition, the uncertainties in the Nusselt numbers ranged from 8% at strip 1 to 5.9% at strip 20. Uncertainty of the Reynolds numbers ranged from 3.3% at Re = 230 to 1.9% at Re = 1016. Reynolds number uncertainties were primarily due to acquiring an accurate volumetric flow rate from pressure drop measurements across the LFE.

3. COMPUTATIONAL METHODOLOGY

Three-dimensional computational simulations were completed using the commercial package (Fluent 6.1, 2002). Fluent is a pressure-based, incompressible flow solver that can be used with structured or unstructured grids. CFD predictions were obtained by solving the momentum equations, energy equation, and the radiation transport equation (RTE), using second order discretization. The flow was simulated as three-dimensional, laminar, and steady. To replicate the experiments, a single row of 17 streamwise louvers, including one entrance louver, one reversal louver, and one exit louver, made up the computational domain. Periodic boundary conditions were used to computationally simulate the infinite stack of louvers. The inlet to the computational domain was located 3 louver pitches upstream of the entrance louver while the exit was located 6.5 louver pitches downstream of the exit louver. A constant velocity boundary condition was applied to the inlet at the matched Reynolds numbers. The exit to the fin channel was assigned an outflow boundary condition. A constant heat flux was applied to the tube wall (flat plate) surface and a symmetry boundary condition was applied at the channel's midspan. The louver surfaces and the tube wall were assigned emissivity values of 0.3 and 0.98 to replicate the silver louvers in the experimental test section. Since the effectiveness of the louvers was calculated to be small, the base of the louvers was considered to be adiabatic.

To ensure a high quality mesh, several steps were taken. First, a quadrilateral grid was attached along the tube wall surface. This grid allowed for higher resolution along the heat transfer surface while capturing the tube wall boundary layer. Through previous simulations, the tube wall boundary layer thickness was computed; thus, the depth of quadrilateral meshing was known. Second, the volume of the channel was meshed using an unstructured scheme with constant grid density.

Grid insensitivity was obtained through a number of grid density studies. These studies included repeatability of the predictions of the heat transfer at the tube wall. Five adaptations on velocity and temperature gradients rendered a final grid containing approximately 2.2 million cells. The difference in the average tube wall Nusselt number between the initial mesh (consisting of 1.1 million cells) and the final mesh was 7%.

Further grid independency studies were limited by computational memory restrictions. The convergence criterion used was that residuals for u, v, w, and continuity dropped by four orders of magnitude and seven orders of magnitude for energy and radiation intensity. All computations were performed in parallel and required approximately 250 iterations to ensure convergence.

3.1 Radiation Modeling

Radiation exchange between the tube wall and the louvers required that additional radiation modeling needed to be included with the CFD predictions. Fluent's Discrete Ordinates (DO) model solves the radiation transfer equation for a discrete number of finite solid angles. By including the DO model, the intensity of radiation at any position along a path through an absorbing, emitting, and scattering medium is accounted for. Although scattering and absorption through air was minimal, the emissivity of the louvers posed a potential for radiation absorption. The discretized version of the RTE in the DO model, directly accounts for directional dependence of radiation exchange to the louver surfaces, therefore accounting for radiation absorption within the louver array. Convergence of the DO model required two iterations of the RTE per flow iteration.

Credibility in the DO model was obtained by experimentally comparing the tube wall Nusselt numbers for different ΔT conditions. ΔT is the temperature difference between the local surface temperature of strip heater 1 and the inlet air temperature. By adjusting the surface heat flux to the tube wall, the desired ΔT condition was obtained. All experiments were conducted at a ΔT of approximately of 9 ^oC. For the lowest Reynolds number investigated, Re = 230, experimental tests were conducted at both ΔT = 9 ^oC and 15 ^oC. By conducting the experiment at Re = 230 and ΔT =15 ^oC , calculation of the tube wall Nusselt number from equation 1 was more dependent on predictions of χ_L than in any other case. The ability of the DO model to accurately predict the radiation losses for different ΔT conditions is well illustrated in figure 5. As illustrated, the DO model predicts lager values of χ_L for the larger ΔT case. The repeatability in Nusselt number, as shown in figure 5, verifies that radiation losses to the louvers can be directly accounted for as expressed in equation 1.

4. EXPERIMENTAL AND COMPUTATIONAL RESULTS

Heat transfer measurements and predictions were made along the tube wall for three different inlet Reynolds numbers (Re = 230, 625, 1016). Nusselt numbers, based on the louver pitch, were used to compare the tube wall heat transfer coefficients. Since experimentally the tube wall consisted of twenty strip heaters, each instrumented with one center thermocouple, experimental measurements of heat transfer represent the local heat transfer at the center of the strip. All heat transfer coefficients were based on using the inlet air temperature as the reference temperature.

4.1 Tube Wall Heat Transfer Coefficients

Figures 6 through 8 show the experimental measurements and computational predictions of the convective heat transfer at the tube wall as a function of the non-dimensional fin length for Re = 1016, 625, and 230. Note that the non-dimensional axial distance, X, is the streamwise distance scaled with the entire fin length of the 17 louvers. The Nusselt number in each graph has been calculated for each thermocouple position (center, top, and bottom) corresponding to figure 4. This allowed for the periodicity in the heat transfer measurements to be evaluated. The CFD predictions were plotted in two different forms on figures 6-8. The local values are the predicted Nusselt numbers at the location of the thermocouples whereas the pitch-wise averaged Nusselt numbers are the pitch-wise averaged values at each given axial location. The spikes in the local Nusselt numbers that were predicted using CFD indicate the variation in the heat transfer coefficients caused by the louvers. The contour plot in figure 9 for Re = 1016 indicate that there is a large spatial variation of the local heat transfer coefficients. Also given in figures 6-8 is the Nusselt number one would achieve for a laminar boundary layer along a flat plate with a constant heat flux boundary condition, (Incropera and DeWitt, 1996) as given by:

$$Nu_o = \frac{hx'}{k} = 0.453\left(Lp/x'\right)Re_{X'}^{0.5}\,Pr^{0.33} \qquad (2)$$

Note that the Nusselt number is a scaling of the local heat transfer coefficients and that the normalizing length scale is the louver pitch, which is a constant.

Based on the measurements shown in figure 6 for the Re = 1016 case it is clear that there is relatively good periodicity indicated for the Re = 1016 case with the center, top, and bottom thermocouples in good agreement. To ensure that the heat transfer occurring at the tube wall was not influenced by natural convection, experiments were conducted for different test section orientations. Measurements taken at the center, top, and bottom thermocouples remained in good agreement for the different test section orientations and indicated that only a forced convective environment was present. There is also relatively good agreement between the measurements and the CFD predictions, but both the measurements and predictions are much higher than those predicted by using equation 2. The heat transfer at the entrance region of the tube wall, ($0 < X < 0.1$), is quite high as expected from being a thin boundary layer at the entrance as shown in figure 6. At X = 0.1 the flow is introduced to the effects caused by the turning segment of the entrance louver, which causes an increase in the wall heat transfer coefficients. Between $0.1 < X < 0.25$ the flow changes from axial to louvered directed. Within this region, the tube wall heat transfer is dependent on two mechanisms. First, the transition of the flow from axial to louver directed assists to mix out the boundary layer. Second, vortices occurring at the leading and trailing edges of the louvers augment the surface heat transfer. The predicted Nusselt number contours in figure 9 indicate very high gradients at the entrance louver, but seem to decrease near the fourth louver position where the flow is louver directed, which agrees with the experimentally measured heat transfer coefficients along the louver (Lyman et al., 2002).

In the louver directed flow region ($0.25 < X < 0.45$) for Re = 1016 in figure 6, heat transfer from the tube wall is highly dependent on the leading edge vortices, which is also well illustrated in the contours of predicted Nusselt numbers on the tube wall (figure 9). For $0.25 < X < 0.45$, there is a similar decrease in the heat transfer coefficients as predicted by the flat plate correlation only with levels being much higher than the correlation. Midway through the passage (X = 0.45) there is a sudden spike in the heat transfer coefficients as the flow experiences the effects of the reversal louver. The peak of the spike coincides with the center of the reversal louver. Note that the local and pitch-wise averaged spikes are in a slightly different location because the thermocouple density was not high enough to detect the local spike in the vicinity of the reversal louver.

CFD predictions also show higher spikes in the Nusselt number at the flow reversal louver than what was experimentally measured. Differences in agreement between measurements and CFD predictions at the reversal louver were attributed to flow separation, as discusses in a later section of this paper. It is believed that CFD simulations over predicted effects of separation within the vicinity of the flow reversal louver. Beyond the reversal louver, there is again a decrease in the tube wall Nusselt numbers until the exit where the flow experiences the exit louver. As the flow develops in the second half of the channel, trends of heat transfer at the tube wall are similar to the developing region before the reversal louver, but less pronounced. The lower heat transfer coefficients along the second half of the tube wall are attributed to the thicker tube wall boundary layer.

Figure 7 shows trends at Re = 625 very similar to that already discussed for Re = 1016 shown in figure 6. The measurements and CFD predictions agree fairly well and are both much above that predicted for a flat plate. Although the predicted wall contours are not shown, similar trends are indicated with the high gradients in heat transfer coefficients at the entrance, reversal, and exit louvers. The predictions indicate that by the fourth louver, the heat transfer contours indicate a repeating pattern and as such indicates that the flow is once again louver directed. As one would expect, the primary difference between figures 6-8 are the occurrence of lower heat transfer coefficients at the lower Reynolds number.

4.2 Augmentation of the Tube Wall Heat Transfer

The augmentation of the tube wall heat transfer coefficients can be calculated relative to the heat transfer coefficients for a flat plate and relative to the heat transfer coefficients occurring along each individual louver. Figure 10 shows the augmentation of the tube wall heat transfer coefficients relative to that occurring along a flat plate at Re = 230, 625, and 1016. As can be expected from the presence of additional secondary flow motions, which will be discussed in the next section, there is a definite enhancement of the heat transfer coefficients relative to what would occur for a flat plate with values ranging between 1 and 2 over most of the tube wall surface.

Figure 11 compares the ratio of the heat transfer coefficients along the tube wall to that of the heat transfer coefficients occurring along each individual louver. Note that spatially resolved heat transfer coefficients were previously reported by Lyman et al. (2002) along the louver for the same Reynolds number and geometry. These heat transfer coefficients were spatially-averaged along each of the louver surfaces (from louver 2 to 8). The averaged Nusselt numbers for each louver were then used in the denominator of the augmentation ratio, as shown in figure 11. Since data regarding the heat transfer coefficients are unavailable for Re = 625, only augmentation ratios for Re = 230 and 1016 are shown in figure 11. Note that the louver heat transfer coefficients used the local bulk temperature as the reference temperature, which is more relevant for the louvers since the bulk temperature takes into account the added heat from the upstream louvers. The results indicate that the heat transfer coefficients are much lower on the tube wall than along the louver surfaces, which is most likely a result of the boundary layer beginning at the start of each louver in contrast to a more continuous boundary layer along the tube wall. Within the vicinity of ($0.3 < X < 0.45$), where the flow is louver directed, the ratio of tube wall to louver heat transfer is approximately 0.4 for Re = 1016 and 0.3 for Re = 230. These values are almost double the predicted values reported by Tafti and Cui (2003) in the louver directed region. The differences between our study and that of Tafti and Cui (2003) can mainly be attributed to the following: First, Tafti and Cui (2003) heated both the tube wall and the louvers; thus surrounded the tube wall with a warmer thermal field than in this study. Second, the developing flowfield and heat transfer effects at the entrance, reversal, and exit louvers are included in our study, whereas Tafti and Cui (2003) considered only fully developed flow.

Although it is not presented here, the velocity and thermal boundary layer thicknesses were calculated from the CFD predictions along the tube wall in number of axial locations and compared with what would be expected for a flat plate boundary layer. The thicknesses in the pitch wise center of the louvers were found to be significantly thinner than that expected from flat plate correlations. As an example, consider the fifth louver where the boundary layer thickness was 13% of the louver pitch, as compared with that predicted for a flat plate, which was 31% of the louver pitch.

4.3 Thermal Fields Along the Tube Wall

With the intention of understanding the effects augmenting the tube wall heat transfer, an analysis was completed of the predicted thermal fields in various locations along the louver array. These thermal fields were analyzed at the key locations shown in figure 12 as P1 through P5 for Re = 1016. Note that these planes were placed normal to the tube wall surface where the local coordinates are defined as (x', y', z') . The thermal fields shown in figures 13 – 15 are presented in terms of a non-dimensional temperature, θ, which is based on the inlet temperature and the local wall temperature. θ is given by equation 3 as

$$\theta = \frac{T - T_{in}}{\overline{T_w} - T_{in}} \tag{3}$$

Note $\overline{T_w}$ was calculated along the thermal field of interest.

Figures 13 – 15 show the thermal fields, resulting from the complicated flow structures along the tube wall, as analyzed on planes P1 through P5. Starting with P1, the thermal field between louver 1 (shown as the black vertical bar at y = 0.3) and the entrance louver (shown as dotted lines at y = 0.7) is shown in figure 13. A fairly consistent and thin thermal field exists on both sides of the first louver. As one moves past the first louver on the y-axis the thermal field suddenly thickens, particularly in the region of $(0.5 < y < 0.7)$. This phenomenon can be attributed to two effects. First, as the axial directed flow approaches bend in the entrance louver, it no longer remains attached to the entrance louver and separates. Second, as the flow passes the entrance louver, a wake is produced. It is believed that both of these phenomena thicken the thermal fields within the $(0.5 < y < 0.7)$ region as illustrated in figure 13. This thickening of the boundary layer causes high gradients in the heat transfer coefficient as illustrated in figure 9.

As mentioned earlier, it is suspected that leading edges of the louvers help augment heat transfer along the tube wall. This effect is apparent from figures 6 – 8 as well as in the contour plot of the tube wall Nusselt number shown in figure 9. To better understand the mechanism that augments heat transfer at the leading edges, thermal fields at locations P2 and P3 were created. From figure 14a, it is obvious that as the flow approaches the leading edge of louver 5, a vortex is created and the surrounding thermal field is thinned. As shown in figure 14a, the thermal field is considerably uniform from ($-0.3 < x < -0.1$) until approximately $x = -0.09$, where there is a significant downturning of cooler fluid towards the wall. The leading edge vortex causes a sudden decrease in θ and is the mechanism responsible for high Nusselt numbers at the leading edges of all the louvers in figure 9. In addition to augmentation at the leading edge, the downwash caused by the leading edge vortex also augments heat transfer along the louver pitch. So strong are the effects of the leading edge vortex, that boundary layer thinning is still evident in figure 14b ($0.1 < y < 0.5$), of which P3 is located 30% of a louver pitch upstream of the leading edge. Figure 9 shows the augmentation along the louver pitch due to the downwash of cooler fluid by the leading edge vortex. The wake of the trailing edge of louver 4 (represented by dotted lines) is also well illustrated in figure 14b within ($0.62 < y < 0.76$) where the thermal field is slightly extended. Since the increase in the thickness of the thermal boundary layer is only slightly increased within this region there is not a dramatic decrease in Nusselt number at the trailing edges of the louvers as shown in figure 9.

Comparable to the separation effects occurring within the vicinity of the entrance louver are the flow structures resulting from the flow reversal louver. For the case of the reversal louver, separation and the extension of the surrounding thermal fields are more pronounced than at the entrance louver. The larger separation was expected since the flow reversal louver imposes a 54^o change rather than 27^o change to the flow path as imposed by the entrance louver. Extension of the thermal field is well illustrated in the contours of θ shown in figures 15a-b. As shown in figure 15a, the underside of the flow reversal louver ($-0.32 < Y'/L_p < 0$) serves to thin the thermal boundary layer, whereas along the top surface of the reversal louver, the thermal boundary layer is extended. Since the strongest effect of separation was expected to occur at the final bend of the flow reversal louver, plane P5 (figure 15b) was used to capture any separation affects that might occur. Figure 15b, clearly shows that before the solid vertical bar (representing reversal louver), the thermal boundary layer thickness is thin ($0 < y < 0.2$). θ also becomes smaller as the louver is approached. However, on the opposite side of the vertical bar ($0.3 < y < 0.84$), the thermal boundary layer is extended. The larger values of θ, which result from a thicker thermal field, are comparable to that of the entrance louver.

5. CONCLUSIONS

In this paper, experimental and computational results of the heat transfer at the tube-fin junction for louvered fin heat exchangers have been presented. Commonly used as a method to increase fin heat transfer, it has been determined that louvered fins also augment tube wall heat transfer. For all Reynolds numbers investigated, reasonable agreement with steady, three-dimensional computational predictions where achieved. Through thorough experimental measurements and computational predictions, it has been determined that an augmentation ratio of up to 3 times can occur for a tube wall with fins as compared to a flat plate. Secondary flow patterns caused by vortices and separation were defined as the mechanisms that augment tube wall heat transfer. Vortices near the leading edge of the louvers have been determined to increase heat transfer by thinning the tube wall boundary layer. While the entrance and reversal louver cause separation, it has been determine that these louvers are vital in re-starting the boundary layer for the tube wall located downstream of them.

Acknowledgments

The authors gratefully acknowledge Modine Manufacturing Company for sponsoring the work that was presented in this paper.

Nomenclature

A	Louver surface area
$A_{c,f}$	Cross sectional area of a straight fin
F_p	Fin pitch
h	Convective heat transfer coefficient, $h = q'' / (T_w - T_{in})$
k_f	Thermal conductivity of the balsa wood
L_p	Louver pitch, length of louver
L_f	Length of the fin
Nu	Nusselt number based on louver pitch, $Nu = h\,L_p / k$
Nu_L	Average Nusselt numbers of louvers 2-8 (Lyman, et al.)

Nu_o	Baseline Nusselt number given by the flat plate correlation, equation 2 (Incropera and DeWitt, 1996)
P_f	Perimeter of a straight fin
q''_{power}	Applied heat flux boundary condition
q''	Convective heat flux from heated wall
q''_c	Heat flux lost due to conduction
q''_r	Heat flux lost due to radiation
Re	Reynolds number based on louver pitch, $Re = U_{in} \cdot L_p / \nu$
R_p	Resistance of the precision resistor
R_c	Thermal resistance between the conduction guard heater and the tube wall
t	Louver thickness
T_w	Surface temperature of the tube wall
T_{P1}	Surface temperature of the conduction guard heater
T_{P2}	Surface temperature of the radiation guard heater
U_{in}	Inlet face velocity to test section
X',Y',Z'	Fin dimensional coordinate system, see figure 1
X,Y,Z	Normalized fin dimensions, $(X'/L_f, Y'/L_f, Z'/L_f)$
$x',y'z'$	Louver dimensional coordinate system, see figure 11
x,y,z	Normalized louver dimensions, $(x'/L_p, y'/L_p, z'/L_p)$

Greek

θ	Louver angle, non-dimensional temperature (see equation 3)
ν	Kinematic viscosity
χ_L	Fraction of tube wall-louver radiation losses to applied heat flux (as given by RTE)
χ_W	Fraction of tube wall-lexan wall radiation losses to applied heat flux
ε_L	Emissivity of the louvers
ε_w	Emissivity of the milled lexan wall
σ	Stefan-Boltzmann constant
ΔT	Temperature difference between strip 1 and the inlet air
η_f	Effectiveness for an infinitely long fin (Incropera and DeWitt, 1996)

Superscripts

$\overline{\ }$	Averaged value
$'$	Dimensional values

References

Achachia, A., Cowell, T. A. 1988. Heat Transfer and Pressure Drop Characteristics of Flat Tube and Louvered Plate Fin Surfaces. *Experimental Thermal and Fluid Science*. 1: 147-157.

Atkinson, K. N., Drakulic, R., Heikal, M. R., Cowell, T. A. 1998. Two and Three dimensional Numerical Models of Flow and Heat Transfer Over Louvred Fin Arrays in Compact Heat Exchangers. *International Journal of Heat and Mass Transfer.* 41: 4063-4080.

Beauvais, F. N. 1965. An Aerodynamic Look at Automobile Radiators. SAE 650470.

Davenport, C.J. 1983. Correlations for Heat Transfer and Flow Friction Characteristics of Louvered Fin Heat Transfer. AICHE Symposium Series. 79: 19-27.

FLUENT/UNS User's Guide. 2002. Release 6.1. Fluent Inc., Lebanon, New Hampshire.

Incropera, F.P. and DeWitt, D.P. 1996. *Fundamentals of Heat and Mass Transfer*. pp.120-122, 352, 358. New York: Wiley.

Kays, W. M. and London, A.L. 1984. *Compact Heat Exchangers*. pp. 1-75. New York: McGraw-Hill.

Kline, S.J. and McClintock, F.A. 1953. Describing Uncertainties in Single Sample Experiments. *Mech. Engineering*. pp. 3-8.

Lyman, A. C., Stephan, R. A., Thole, K. A., Zhang, L., Memory, S. 2002. Scaling of Heat Transfer Coefficients Along Louvered Fins. *Experimental Thermal Fluid Science*. 26 (5): 547-563.

Lyman, A. 2000. Spatially Resolved Heat Transfer Studies in Louvered Fins for Compact Heat Exchangers, MSME Thesis.Virginia Tech, USA.

Moffat, R. J. 1988. What's New in Convective Heat Transfer? *International Journal of Heat and Fluid Flow*. 19: 90-101.

Namai, K., Muramoto, H., Mochizuki, S. 1988. Flow Visualization in the Louvered Fin Heat Exchanger. SAE 980055.

Siegel, R. and Howell, J. 1981. *Thermal Radiation Heat Transfer*. pp. 833-837. New York: HPC.

Springer, M. E., K.A. Thole. 1998. Experimental Design for Flowfield Studies of Louvered Fins. *Experimental Thermal and Fluid Science*. 18: 258-269.

Tafti, D.K., Zhang, L.W., Huang, W., Wang, G. 2000. Large-Eddy Simulations of Flow and HeatTransfer in Complex Three-Dimensional Multilouvered Fins. *ASME Fluids Engineering Division Summer Meeting.* FEDSM2000-11325. Boston, Massachusetts, 11 15 June.

Tafti, D.K. and Cui, J. 2002. Computations of flow and heat transfer in a three dimensional multilouvered fin geometry. *International Journal of Heat and Fluid Flow*.

45: 5007-5023.

Tafti, D.K. and Cui, J. 2003. Fin-tube junction effects on flow and heat transfer in flat tube multilouvered heat exchangers. *International Journal of Heat and Fluid Flow*. 46: 2027-2038.

Webb, R. L.,Trauger, P. 1991. Flow Structure in the Louvered Fin Heat Exchanger Geometry. *Experimental Thermal and Fluid Science*. 4: 205-214.

TABLE 1. Summary of Louvered Fin Geometry

Louver Angle (θ)	27˚
Fin Pitch to Louver Pitch (F_p/L_p)	0.76
Fin Thickness to Louver Pitch (t/L_p)	0.08
Number of Louvers	17
Channel depth to Louver Pitch (d/L_p)	6.3
Scale factor for testing	20

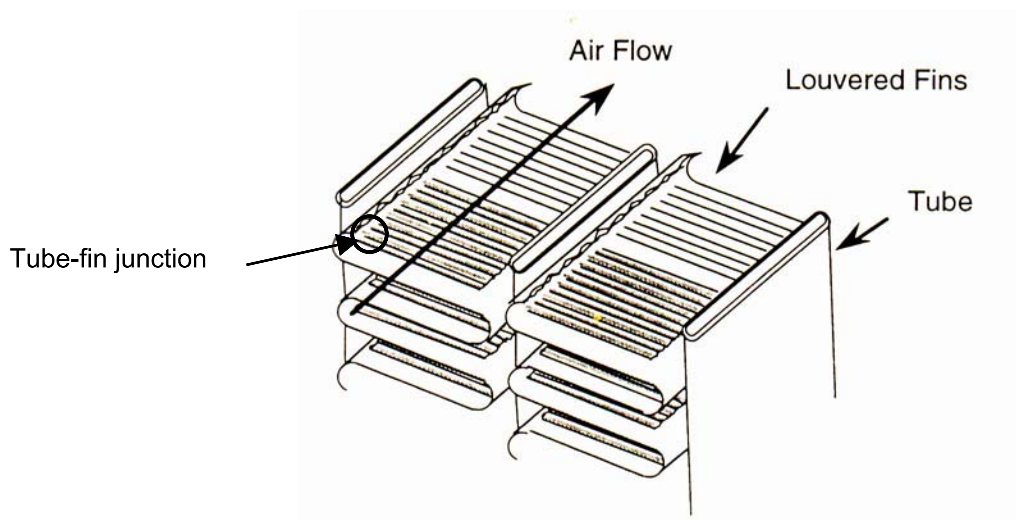

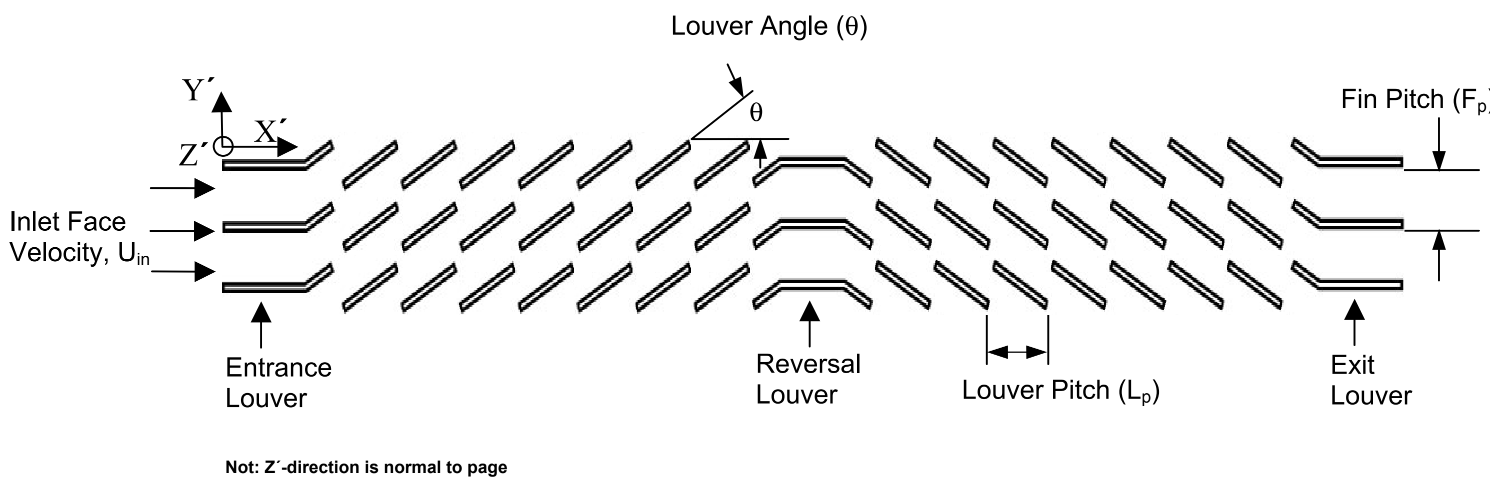

FIGURE 1. Typical louvered-fin compact heat exchanger: (a) assembly and (b) side view of louvered fins.

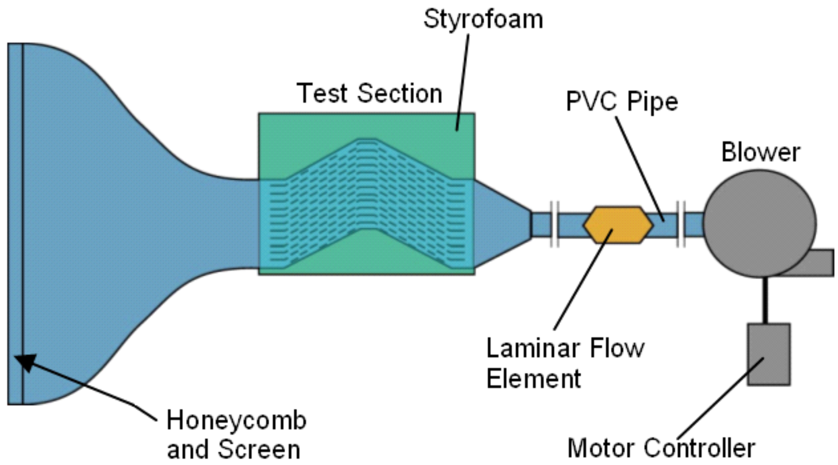

FIGURE 2. Schematic of flow facility for the louvered fin tests.

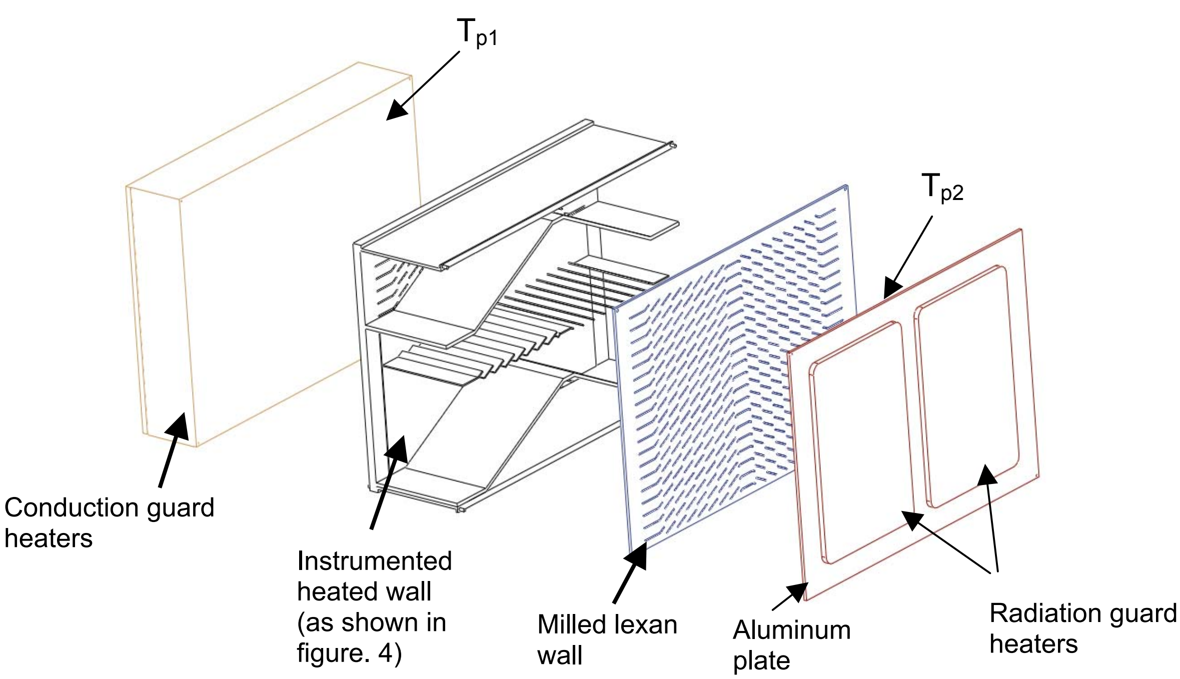

FIGURE 3. Schematic of the test section components.

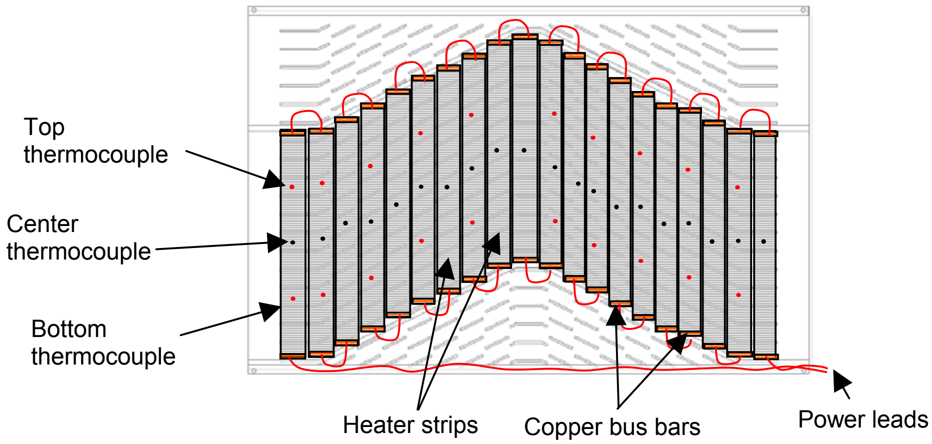

FIGURE 4. Wiring diagram and thermocouple map of heat transfer surface.

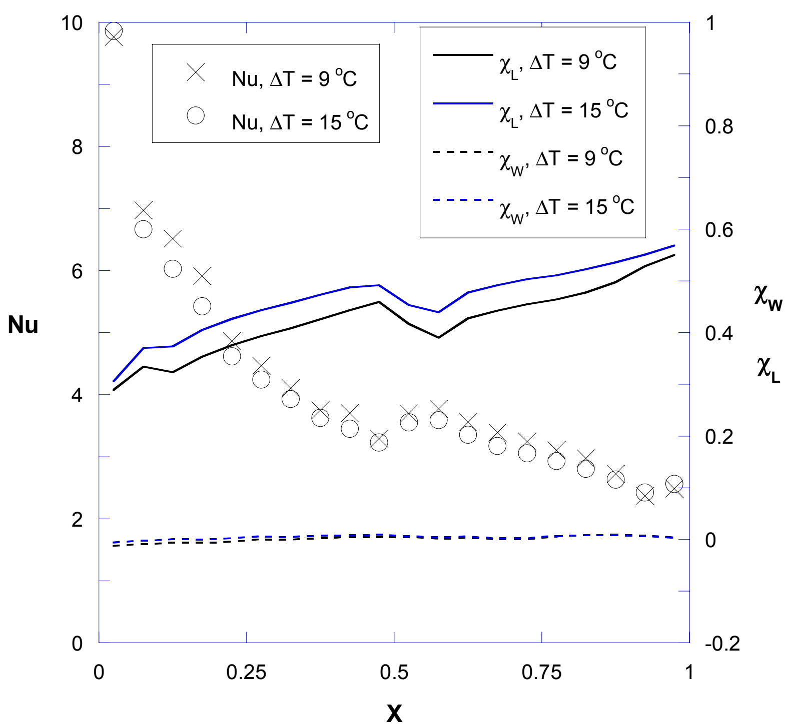

FIGURE 5. Experimental measurements of the tube wall Nusselt number and predictions of χ_w and χ_L as a function of ΔT for Re = 230.

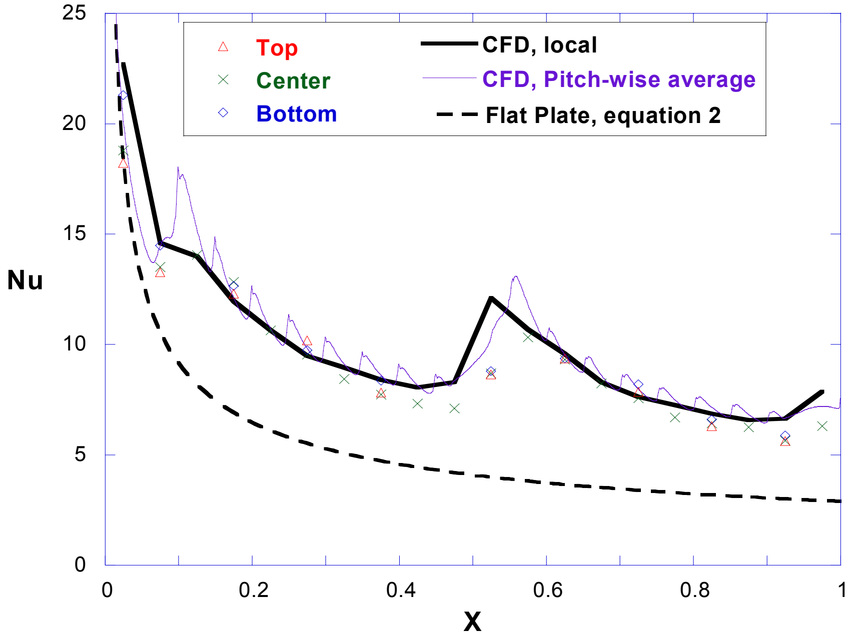

FIGURE 6. Measurements and CFD predictions of Nusselt numbers along the tube wall compared to the flat plate correlation for Re = 1016.

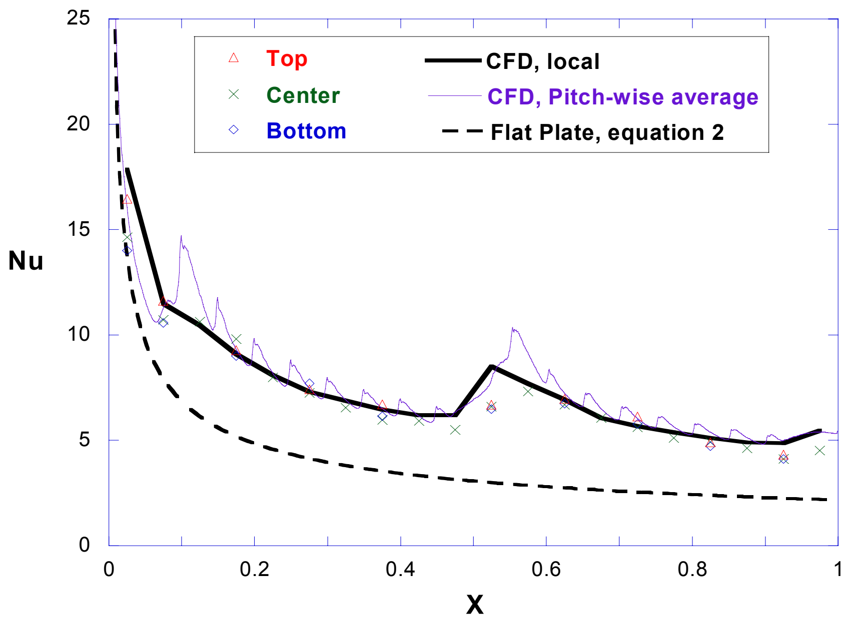

FIGURE 7. Measurements and CFD predictions of Nusselt numbers along the tube wall compared to the flat plate correlation for Re = 625.

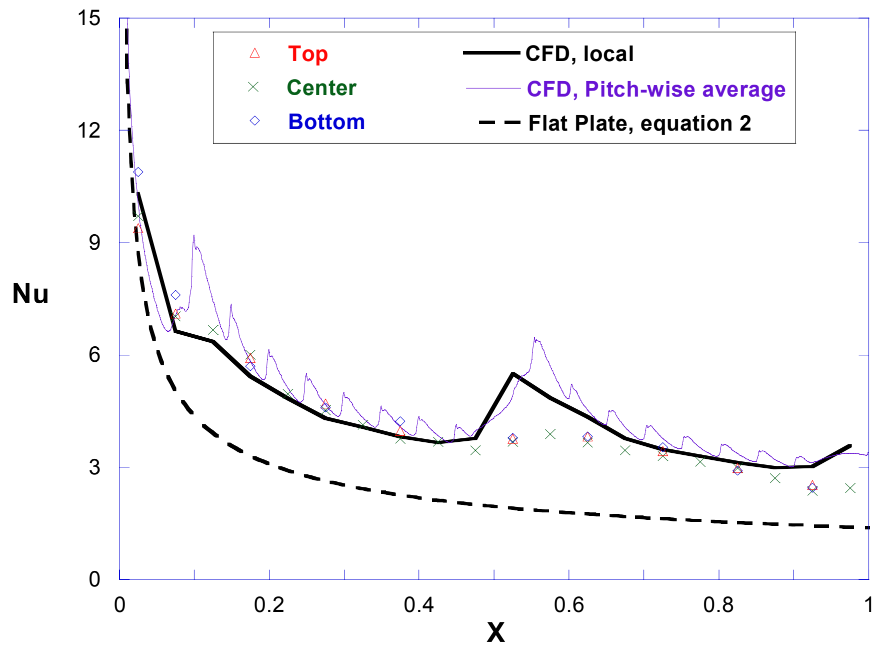

FIGURE 8. Measurements and CFD predictions of Nusselt numbers along the tube wall compared to the flat plate correlation for Re = 230.

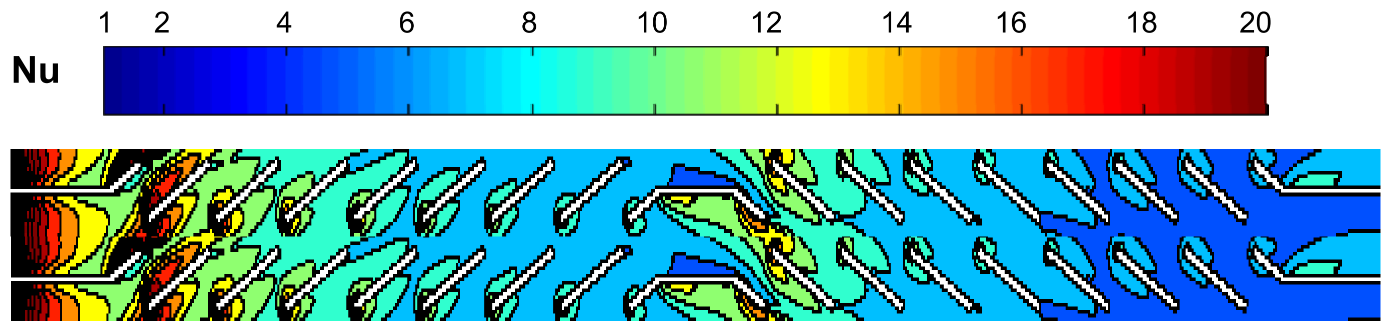

FIGURE 9. CFD contours of Nusselt numbers along the tube wall for Re = 1016.

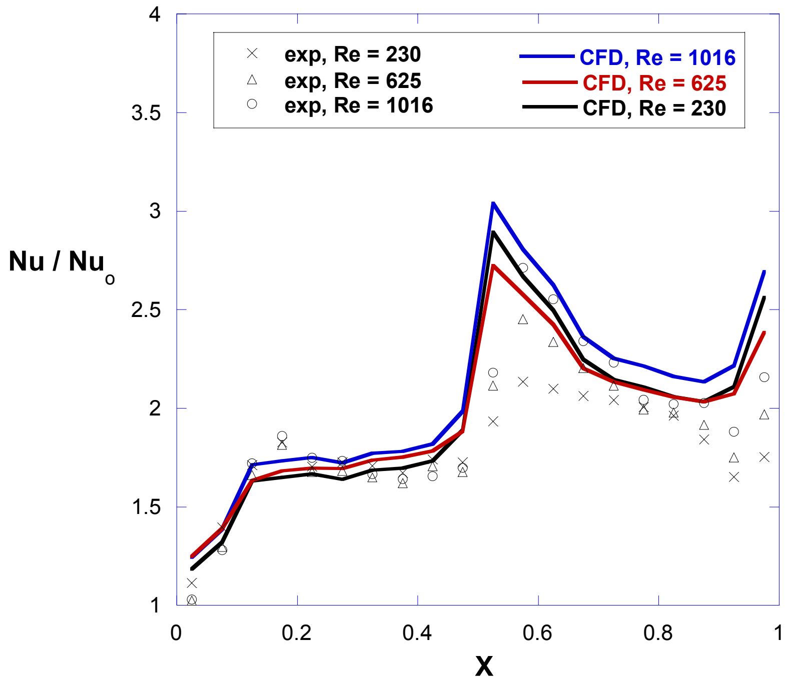

FIGURE 10. Augmentation ratio of the tube-wall as compared to that of the flat plate correlation.

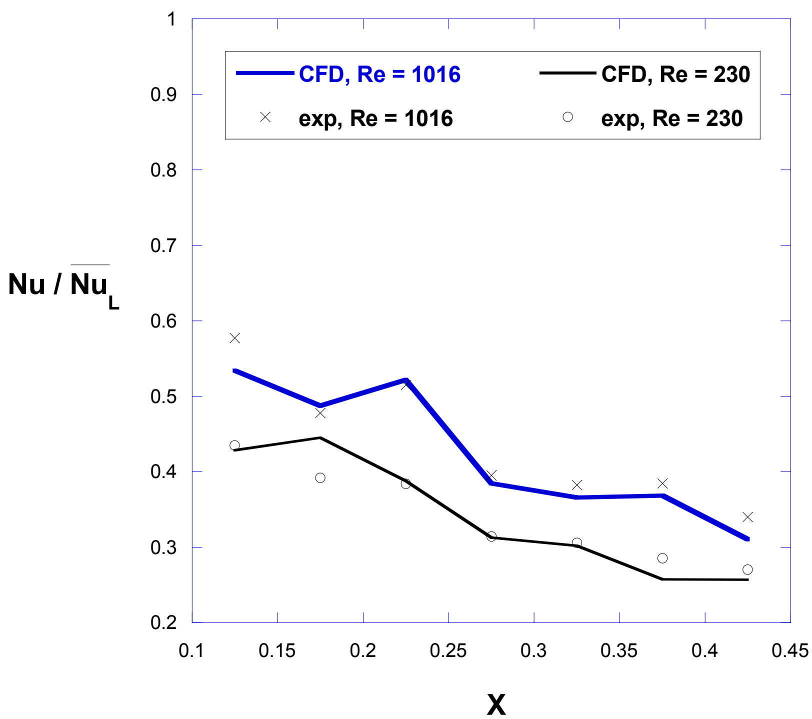

FIGURE 11. Augmentation ratio of the tube-wall as compared to the average louver heat transfer coefficient.

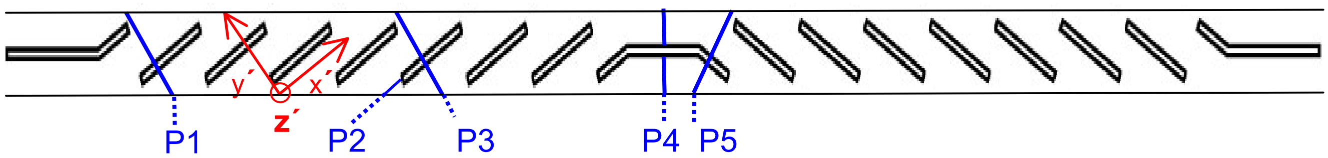

FIGURE 12. Locations of thermal field planes that were analyzed.

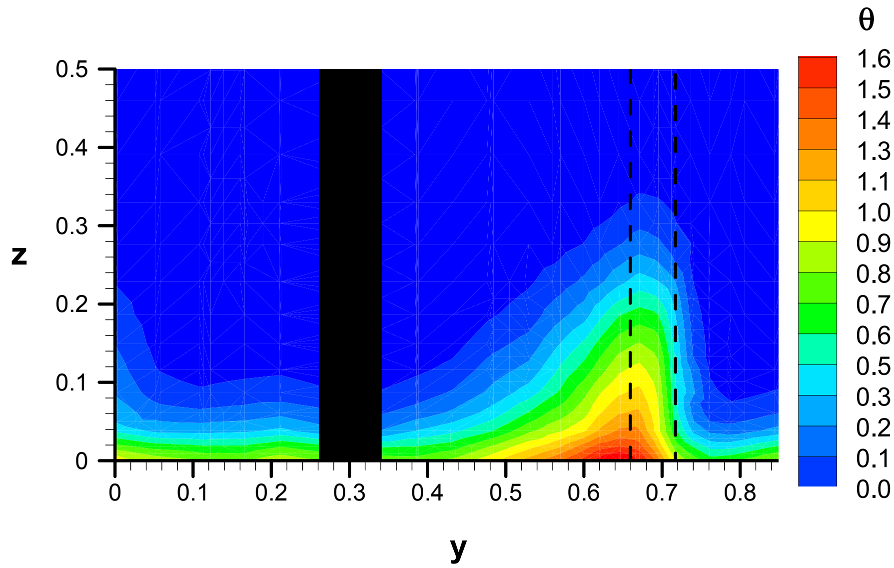

FIGURE 13. Thermal field for plane P1, Re = 1016.

a) Plane P2

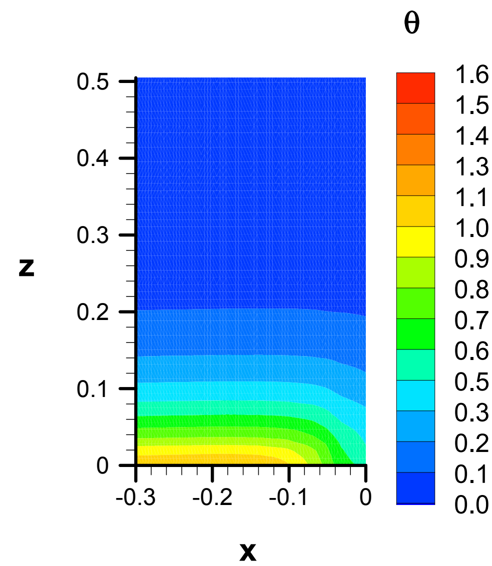

b) Plane P3

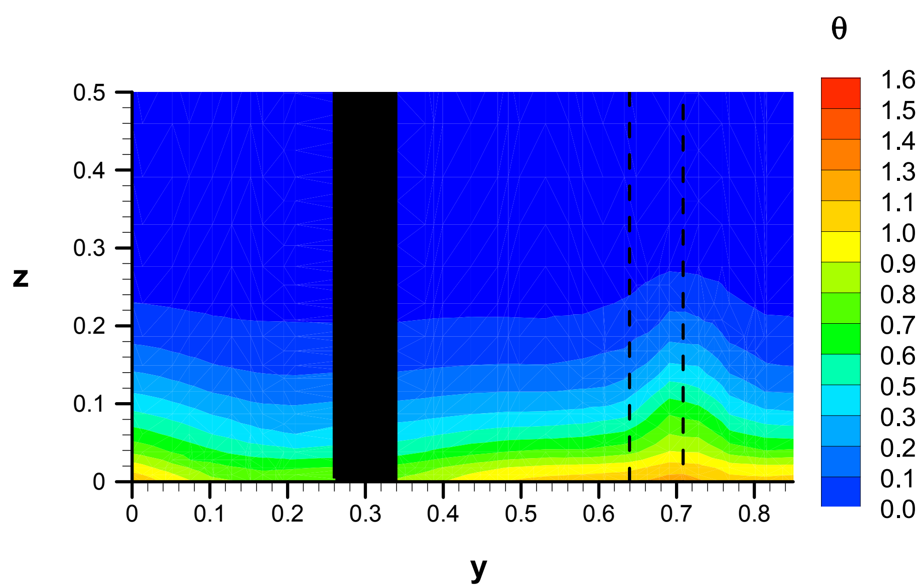

FIGURES 14a-b. Thermal fields for planes P2 and P3, Re = 1016.

a) Plane P4

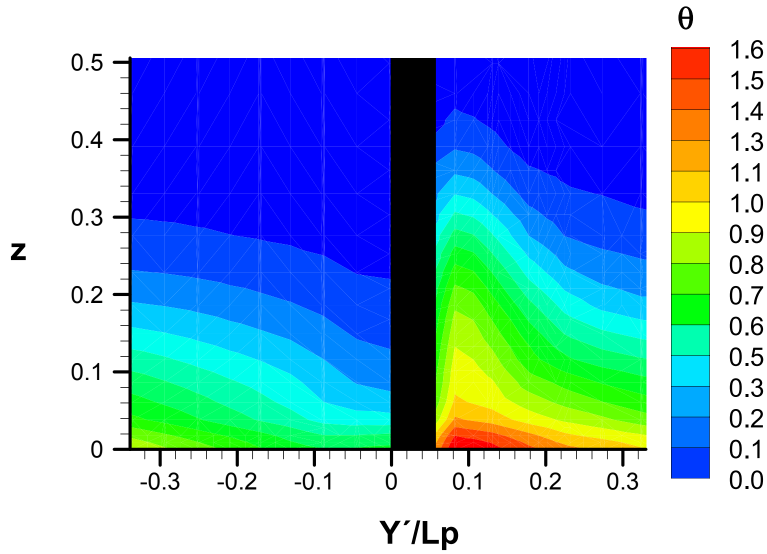

b) Plane P5

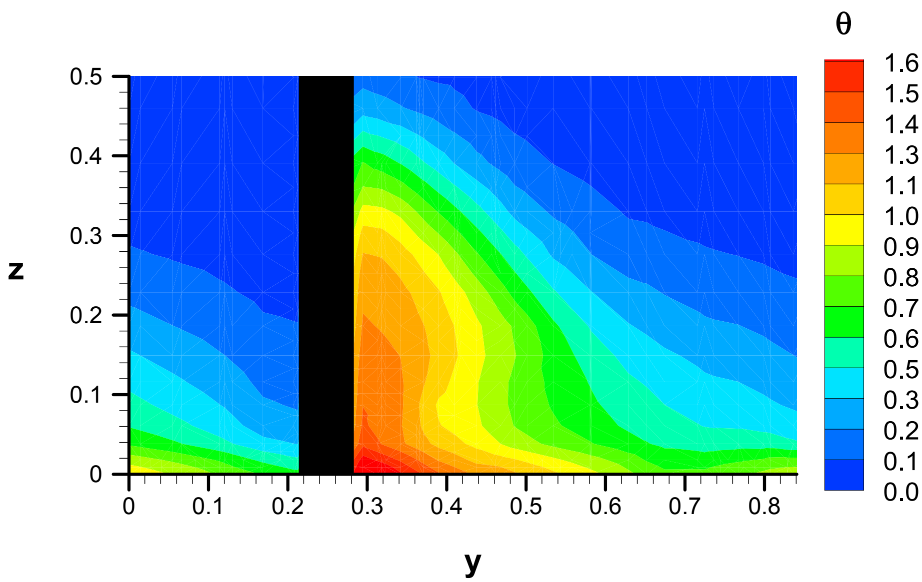

FIGURES 15a-b. Thermal fields for planes P4 and P5, Re = 1016.

Appendix A

Introduction

Compact heat exchangers are usually characterized by a large heat transfer surface per unit of volume. These characteristics are useful when thermal energy between two or more fluids must be exchanged without mixing. A classic example of a compact heat exchanger is an automobile radiator. Figure A.1 depicts an automobile radiation as well as its geometry. For the case of an automobile, antifreeze usually cools the internal components of an engine. After heat is added to the antifreeze, the antifreeze is sent to the radiator where heat is rejected to air. This entire process occurs without the air and the antifreeze mixing. To prevent the fluids from mixing, tubes within most compact heat exchangers usually carry a liquid, while a gas passes over external fins extending from the tube.

Most compact heat exchangers are liquid-to-air heat exchangers, with approximately 85% of the total thermal resistance occurring on the air side of the heat exchanger. The distribution of the thermal resistance in a typical compact heat exchanger is shown in Figure A.2. To reduce the space and weight of a compact heat exchanger, augmentation of heat transfer on the air side must occur. However, before any strategies to augment the air side heat transfer can be proposed, a thorough insight of the current mechanisms that govern air side heat transfer is needed. The attached paper, "Measurements and Predictions of the Heat Transfer at the Tube-Fin Junction for Louvered Fin Heat Exchangers," is a methodical baseline study of the air-side heat transfer that occurs along the tube wall, which leads to potential design improvements. Importance is placed on the tube wall because it provides 10% of the total heat transfer area and the tube wall boundary layer governs a portion of the fin heat transfer near the junction.

The studies in the attached paper represent only one experimental and computational methodology that was investigated for this thesis. Although actual compact heat exchangers experience mixed isothermal and constant heat flux tube wall boundary conditions, discussions with the sponsor suggested that an isothermal tube would represent true operating conditions more adequately. Unlike the experimental setup described in the paper, the initial experimental design incorporated an isothermal tube wall. Experimentally, the isothermal tube wall boundary condition posed several challenges. A completely different methodology from what is described in the attached paper was proposed and unfortunately, implementing the experimental isothermal tube wall was nearly impossible to achieve. Appendix B details the design procedures and experimental tests carried for the isothermal tube wall.

Besides information on the isothermal tube wall boundary condition, this appendix contains additional detail on the design of the constant heat flux tube wall, which was ultimately used for the studies in the attached paper. Appendix C further expands on many topics already discussed in the paper. In particular, more details on the test section, guard heaters, instrumentation and the uncertainty analysis is discussed in Appendix C. Also investigated were strategies of spatially resolving the tube wall Nusselt number around one tube-louver junction. Details of the attempted IR camera measurements are given in the last section of Appendix C. Appendix D begins by further explaining the definition of the heat transfer coefficient used in the paper. Due to the dependence of numerical estimations on the radiation exchange between the tube wall and the louver surfaces, a complete section of Appendix D describes the approaches used to model radiation exchange. Appendix D concludes with discussions on repeatability and periodicity. Comparisons of the predicted heat transfer at the tube wall for both the isothermal and constant heat flux tube wall boundary conditions are given in Appendix E. Concluding remarks and recommendations for future work are discussed in Appendix F.

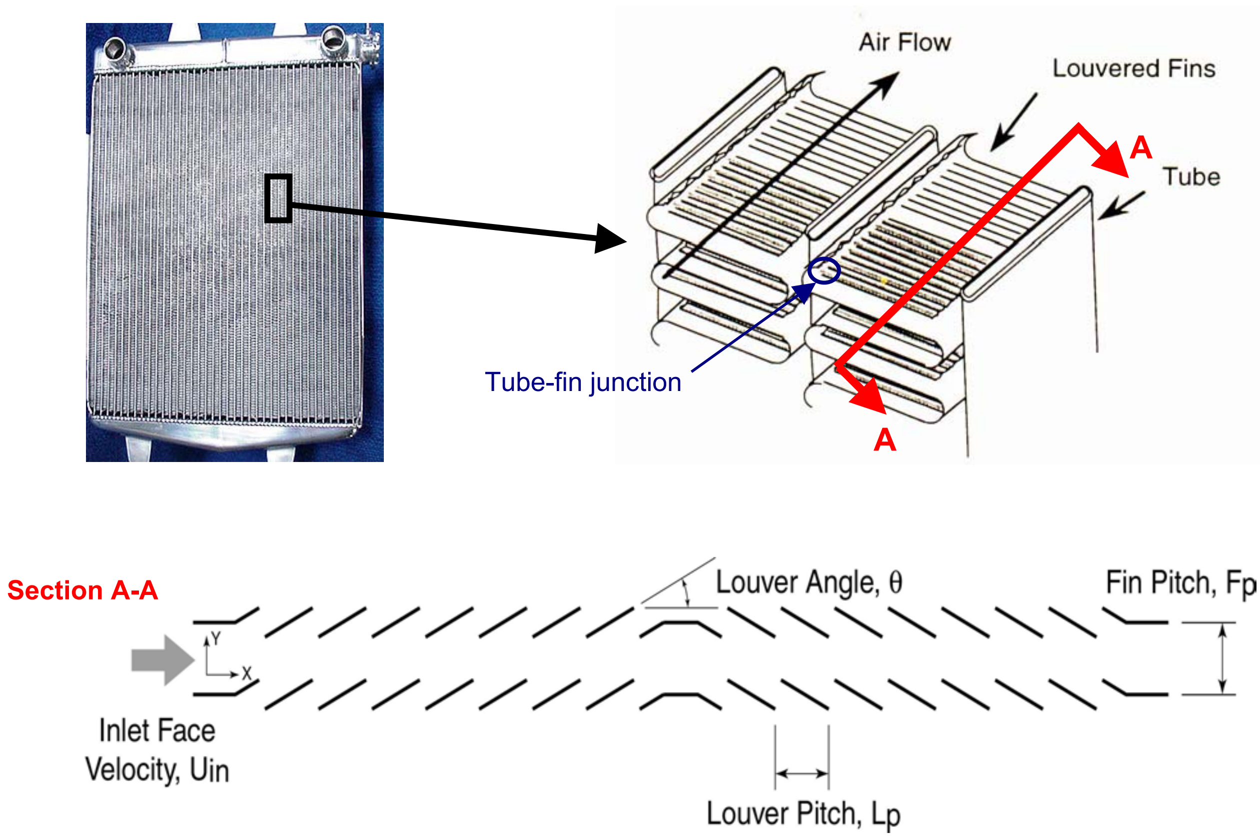

Figure A.1 Typical geometry of a louvered fin heat exchanger used in the automobile industry.

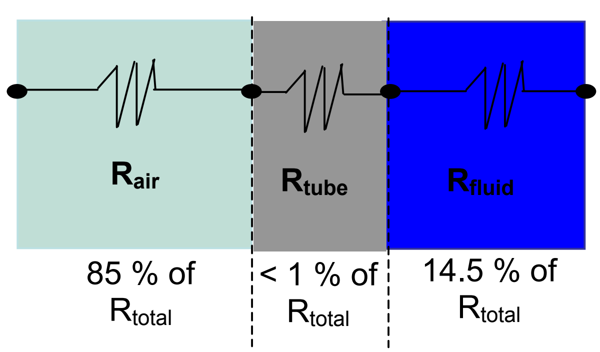

$$R_{total} = R_{air} + R_{fin} + R_{tube}$$

$$R_{total} = \frac{1}{\eta_a h_a A_a} + \frac{1}{k_m A_m} + \frac{1}{h_w A_w}$$

$$R_{total} = 0.23 \cdot 10^{-2} + 2.7 \cdot 10^{-6} + 3.9 \cdot 10^{-4} \quad \left({}^{o}C / W\right)$$

Figure A.2 Thermal resistance network in a typical louvered fin compact heat exchanger

Appendix B

Isothermal Tube Wall Design

As was previously mentioned in the paper, the flow facility used for the study, except for the test section was identical to the set-up reported by Lyman et al. (2002). Initially, the test section was designed to include an isothermal boundary condition along the experimental tube wall. To perfectly maintain a surface exposed to a convective environment at a uniform temperature requires spatial control over the surface heat flux. Since infinite spatial control is impossible, this chapter discuses a method of implementing a nearly isothermal boundary condition with variable width resistive heaters. Selection of the proper strip heater widths is given in Section B.1, along with a brief description of the computational simulations that aided the isothermal tube wall design. The experimental methodology used for the isothermal tube wall is detailed in Section B.2. Finally, the control of the isothermal tube wall is discussed in Section B.3 as well as concluding remarks as to why the isothermal boundary condition failed.

B.1 Selection of Electrical Heaters

The main objective of the isothermal experiments included reducing temperature gradients in the streamwise direction as much as possible. By allowing the strip heater width to vary, temperature variations in the streamwise direction along the strip were minimized. For example, regions experiencing high gradients of the heat transfer coefficient required smaller width strip heaters as compared to regions where the heat transfer coefficients were relatively constant. Before the strips heaters could be assigned a width, the surface heat transfer coefficients along a flat plate was calculated as a function of X´ by equation B.1 (Incropera and DeWitt, 1996).

$$h_{X'} = \frac{k}{X'}\left(\frac{0.3387\,\mathrm{Re}_{X'}^{1/2}\,\mathrm{Pr}^{1/3}}{\left[1+\left(\frac{0.0468}{\mathrm{Pr}}\right)^{2/3}\right]^{1/4}}\right) \tag{B.1}$$

By assuming a temperature difference of 10^{o}C between the surface and the inlet, the local surface heat flux was given by

$$q''_{X'} = h_{X'}\Delta T \tag{B.2}$$

With both the local heat transfer coefficient and surface heat flux known, the tube wall was divided into banks of constant width strips. The local surface heat flux along each strip was then averaged and is represented by $\overline{q''_s}$. To check for temperature uniformity across a strip, temperatures at the leading and trailing edges of the strip were calculated by

$$T_{strip}(X') = \frac{\overline{q''_s}}{h_{X'}} \tag{B.3}$$

By using equation B.3 to calculate the temperature variation across the strip, the width of the strip was varied until the temperature difference between the leading and trailing edges of the strip exceeded no more than 0.5 ^{o}C. By using this tolerance, the analysis indicated that four different width strip heaters were needed. According to width, the strip heaters were then grouped into banks of equal electrical resistance. The properties of each strip heater are listed in Table B.1.

Computational simulations of the tube wall were performed for the heat fluxes given by equation B.2. The computational domain described in the paper is the same as the domain used for the isothermal studies, except for the tube wall boundary condition. Using this domain as a template, two models associated with the isothermal tube wall studies were created. The first model included a tube wall formed by the widths of each of the strips given in Table B.1. Therefore, this model's tube wall contained 29 discrete areas (representing the strips) upon which corresponding isothermal flat plate heat fluxes were assigned as given by equation B.2. The second model did not consist of the discrete heater strip areas; instead a constant surface temperature was imposed on the entire tube wall. By imposing a constant surface temperature along the entire tube wall, the second model allowed for the calculation of the predicted tube wall Nusselt number. The computational results for the second model are discussed in Appendix E. For each strip heater, Figure B.1 illustrates the surface heat flux required to maintain a flat plate at nearly isothermal conditions as well as the response in temperature difference for the flat plate and the tube wall at Re = 230. It is apparent from Figure B.1 that the calculated surface heat fluxes from equation B.3 can not maintain an isothermal tube wall surface. A maximum temperature variation of 2.8 ^{o}C was predicted along the tube wall, while a variation of only 0.3 ^{o}C was calculated for the flat plate. The larger variations along the tube wall are attributed to the louvers ability to augment the thermal fields near the tube wall. For the same surface heat flux, therefore, ΔT was smaller for the tube wall than the flat plate. Although small temperature variations existed along the tube wall for the flat plate heat fluxes, it was believed that further control of the applied heat flux in the test section would significantly minimize temperature variations. A drawing of the test section for the isothermal wall design, detailing the banks of strip heaters and the entrance region where high gradients were predicted to exist, is shown in Figure B.2.

B.2 Experimental Methodology

To build the experimental tube wall, each strip listed in Table B.1 was cut from a roll of grade 316 stainless steel foil. A 6.35 cm thick lexan sheet served as the supportive backing for the strips as illustrated in Figure B.3. To check for temperature uniformity from one strip to another, type E thermocouples were placed underneath each foil in the center of the channel. Periodicity was checked by recording the temperatures above and below the center thermocouples. Omega 2000 paste, which is both highly thermal conductive and electrically insulating, was used to insure contact between the foil and the thermocouples without reducing the integrity of the thermocouple measurements. Figure B.4 illustrates the positions of the thermocouples used along the tube wall.

To experimentally control the applied heat flux to each strip heater, a circuit consisting of 29 precision potentiometers was wired in series with each strip heater. The precision potentiometers were manufactured by Precision Electronic Components Ltd. and had an adjustable resistance of up to 100Ω ± 5%. Each potentiometer was rated at 2 Watts and had ten-turn rotation limit. In addition to the precision potentiometers, each strip heater was wired in series with a precision resistor, which allowed for the current flow to be measured. All the precision resistors used had a nominal resistance of R_p =0.1Ω ± 1%. A National Instruments SXCI-1100 module measured the voltage drops across the 29 precision resistors. The currents through the circuits were then found using Ohm's law

$$I = \frac{V_p}{R_p} \tag{B.4}$$

The heat flux of each strip heater was calculated from equation B.5 where R_s and A_s are the resistance across a strip and the surface area of a strip, respectively.

$$\overline{q_s''} = \frac{I^2 R_s}{A_s} \tag{B.5}$$

Three Hewlett-Packard 6024A power supplies powered the tube wall. With the aid of CFD simulations, discussed in Appendix E, the predicted tube wall heat transfer coefficients were used to calculate the approximate current required by each strip for a $\Delta T = 10\ ^{o}C$. Since each power supply had a maximum of 10 ampere output and CFD simulations predicted 26 amps were needed for Re = 1016, all three power supplies were required to power the tube wall heaters. In addition to the amperage limiting factor of the power supplies, splitting the strip heaters among three power supplies provided more control over the current by isolating groups of potentiometers to dedicated power supplies. Strip heaters from each of the four banks were divided among the three power supplies, thus creating three electrical circuits. The amperage used by each power supply was evenly distributed along the tube wall by wiring strip heaters from different banks together in series. For example, if one power supplied needed 2 ohms, a circuit consisting of one strip from bank 1 and two strips from bank 4 would be required. In this manner, the control of the isothermal wall was simplified. The advantage of being able to switch the wiring configuration is discussed in the next section. An electrical diagram of one circuit is shown in Figure B.5. Note all the strip heaters are wired in parallel with respect to the positive and negative terminals. The actual control panel used for the experiment is depicted in Figure B.6.

B.3 Control of the Isothermal Tube Wall

Control of the current flow through each strip heater caused major difficulties due to implementing the isothermal boundary condition. At the beginning of each experiment, all power supplies were turned off and the resistance of each potentiometer was set to zero. Each power supply was then turned on causing the tube wall to warm up. By monitoring the temperatures of the strip heaters, the potentiometers were adjusted with the intent of reaching temperature uniformity. Unfortunately, temperature uniformity across the tube wall was never obtained. For each of the three heater circuits, any adjustment of one precision potentiometer would influence the circuit's current distribution. As an example, consider Figure B.5. First assume that the potentiometers, R_{pot}, for strips 1-3 and 6 are adjusted in such a way that temperature measurements of strips 1-3,and 6 indicate that near isothermal conditions exist. However, the temperatures of strips 4 and 5 may be cooler than strips 1-3 and 6. Now, imagine an adjustment is made to the potentiometer of strip 4 to allow more current flow. While this adjustment might bring an increase in the temperature of strip 4, strips 1-3 and 6 lose current and become colder. In addition, an adjustment still has not been made for strip 5. The complexity surrounding this example existed for all 29 strips. The initial circuits of the strip heaters were arranged such that strips of nearly equal resistance were grouped together. As the adjustments were made along the tube wall, the current flow on upstream and downstream strips would fluctuate, thus making the experiment nearly impossible to conduct, as demonstrated in the previous example. Regions of high temperature gradients, as experienced near the entrance louver, proved to be extremely difficult to maintain temperature uniformity. As a result of not achieving temperature uniformity, the tube wall Nusselt number did not agree with CFD predictions and trends in the experiment data were erratic, as shown in Figure B.7 for Re = 1016.

Implementing the isothermal tube wall boundary condition was only attempted for the Re = 1016 case. None of the experimental tests conducted showed acceptable repeatability. Different circuit configurations were also implemented by wiring more resistive (thin) strips in series with less resistive (wide) strips. By changing the circuit configuration, control of the higher resistive strips was made less complex since strips with approximately the same resistance were no longer wired in series. However, the slightest change in current to the wider strips (which had a larger convective surface area and required more current) would instantly exceed the potentiometer's 2 Watt power rating. Exceeding the power rating of the potentiometers resulted in multiple burnouts of the internal wirewound of the potentiometer and caused the potentiometer to loose its nominal precision. A thorough search for potentiometers with greater power ratings was performed; unfortunately, precision potentiometers with power ratings of greater than 2 Watts could not be found. The only other adjustable resistance devices available were rheostats, which generally lacked the precision of a potentiometer and therefore were considered unacceptable.

Since implementing the isothermal boundary condition along the tube wall was proven to be unrealistic, the tube wall was redesigned for a constant heat flux boundary condition. To maintain a constant heat flux along the tube wall, new strip heaters of equal electrical resistance replaced the variable width strip heaters used for the isothermal boundary condition. Further detail on the new strip heater resistivities, thermocouple positions, and experimental procedures are given under the "Experimental Methodology" section of the attached paper.

B.4 References

Incropera, F.P. and DeWitt, D.P. 1996. *Fundamentals of Heat and Mass Transfer*. p. 352. New York: Wiley.

Lyman, A. C., Stephan, R. A., Thole, K. A., Zhang, L., Memory, S. 2002. Scaling of HeatTransfer Coefficients Along Louvered Fins. *Experimental Thermal Fluid Science*. 26 (5): 547-563.

Table B.1 Summary of the heater strips used to maintain an isothermal tube wall.

Strip #	Width (mm)	Area (m^2)	Resistivity (Ohms)	
1	3.00	0.0008	1.4	Bank 1
2	3.00	0.0008	1.4	
3	3.00	0.0008	1.4	
4	5.00	0.0013	0.9	Bank 2
5	5.00	0.0013	0.9	
6	5.00	0.0013	0.9	
7	5.00	0.0013	0.9	
8	5.00	0.0013	0.9	
9	5.00	0.0013	0.9	
10	10.00	0.0026	0.6	Bank 3
11	10.00	0.0026	0.6	
12	10.00	0.0026	0.6	
13	10.00	0.0026	0.6	
14	30.00	0.0078	0.3	Bank 4
15	30.00	0.0078	0.3	
16	30.00	0.0078	0.3	
17	30.00	0.0078	0.3	
18	30.00	0.0078	0.3	
19	30.00	0.0078	0.3	
20	30.00	0.0078	0.3	
21	30.00	0.0078	0.3	
22	30.00	0.0078	0.3	
23	30.00	0.0078	0.3	
24	30.00	0.0078	0.3	
25	30.00	0.0078	0.3	
26	30.00	0.0078	0.3	
27	30.00	0.0078	0.3	
28	30.00	0.0078	0.3	
29	30.00	0.0078	0.3	

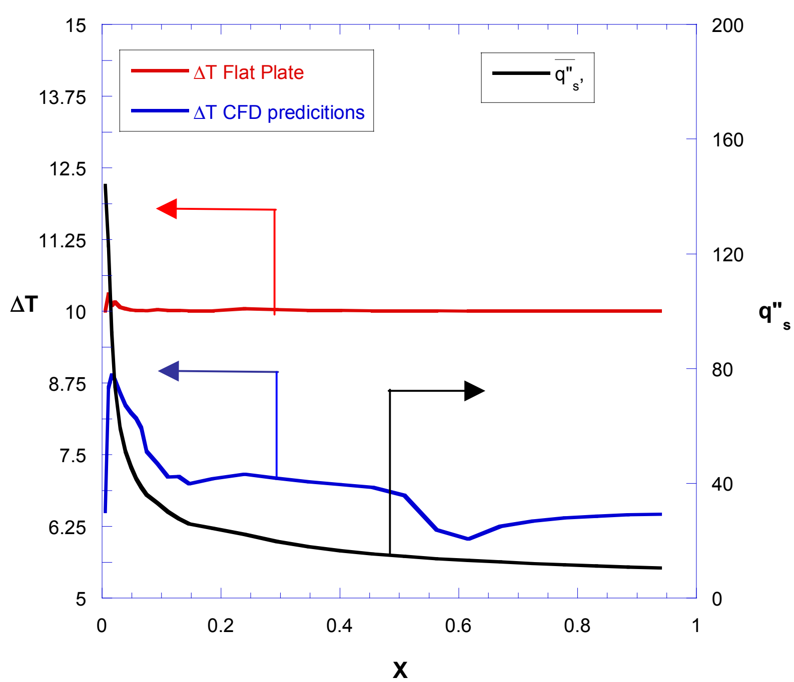

Figure B.1 Temperature variations predicted for the tube wall and the flat plate for isothermal flat plate heat fluxes.

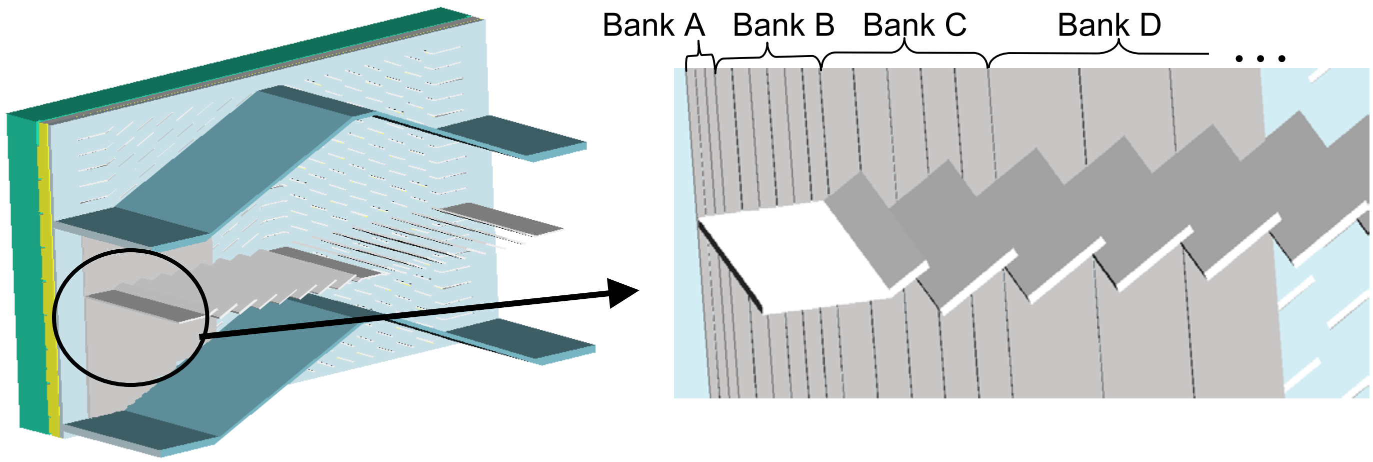

Figure B.2 Illustration of the four different banks of strip heaters used within the vicinity of the entrance louver.

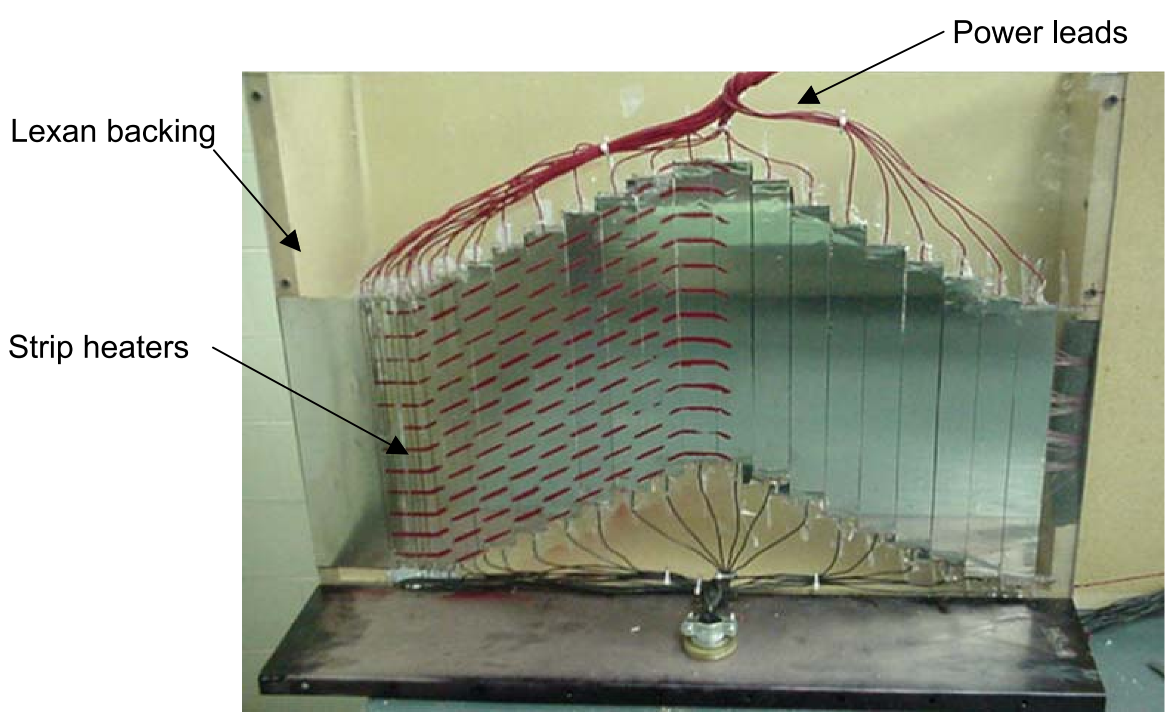

Figure B.3 Detail of the heaters used to create the experimental tube wall.

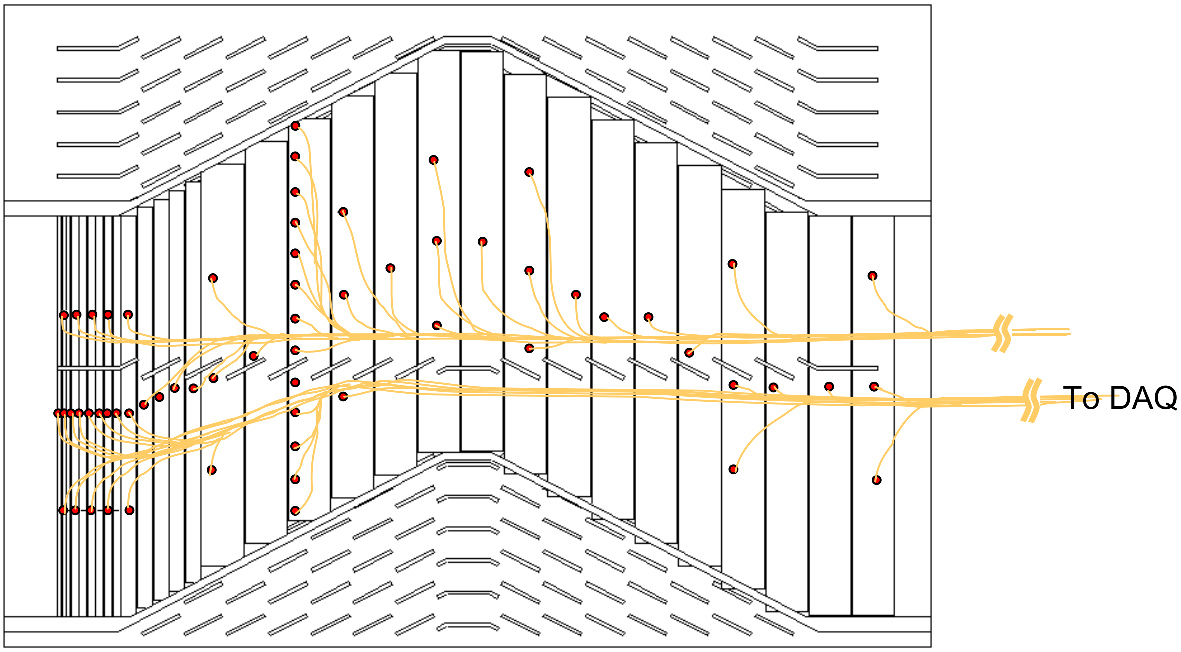

Figure B.4 Thermocouple map for the isothermal tube wall surface.

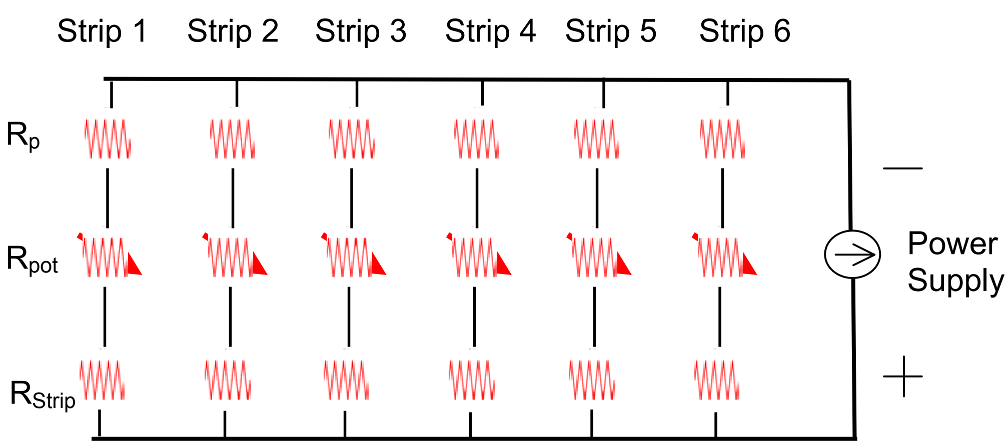

Figure B.5 Electrical diagram for a typical strip heater circuit illustrating multiple strips sharing the same positive and negative terminals for one power supply.

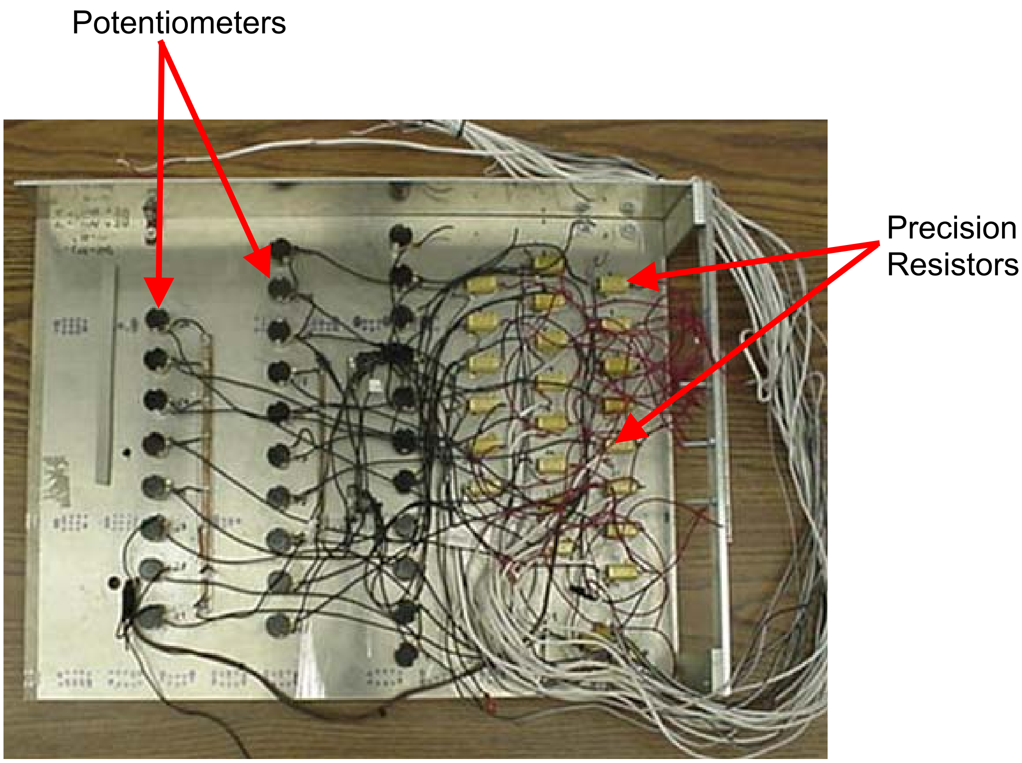

Figure B.6 Picture of the control panel used for adjusting the currents to each strip heater.

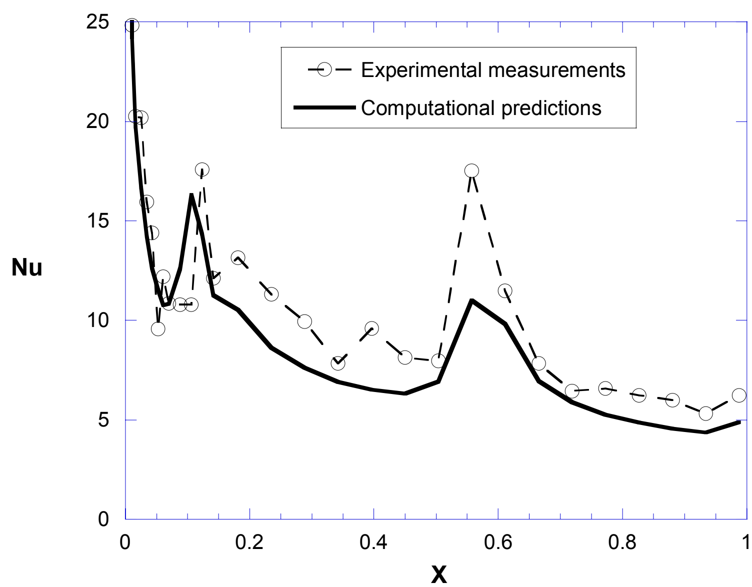

Figure B.7 Measurements and CFD predictions of Nusselt numbers along the isothermal tube wall Re = 1016.

Appendix C

Constant Heat Flux Tube Wall Design

As mentioned in the previous section, maintaining an isothermal tube wall boundary condition is experimentally unrealistic. The current chapter, Appendix C will build upon the experimental design of the constant heat flux tube wall already discussed in the paper. In addition to the experimental tube wall design, given in Section C.1, Appendix C will describe the various components incorporated into the test section used to resolve the tube wall heat transfer coefficients. In particular, Section C.2 will discuss the validity of assuming that balsa wood fins are adiabatic. Section C.3 discusses the design and operating procedures of the guard heaters. Detail on instrumentation and data acquisition is given Section C.4. The uncertainty analysis used for the experimental parameters is described in Section C.5. Finally, Appendix C concludes with Section C.6, which explains a method investigated for incorporating an IR camera to spatially resolve the heat transfer coefficients near one fin-tube junction.

C.1 Tube wall and Channel Design

The tube wall with the constant heat flux surface consisted of twenty stainless steel foils, as mentioned in the paper. Each strip heater was cut from 0.0508 mm thick grade 316 stainless steel foil with nominal electrical resistance of 74 μΩ-cm. Unlike the isothermal tube wall design, each strip heater used for the constant heat flux tube wall had equal widths and electrical resistances. 20 different foils were sampled showing that each had a nominal resistance of R = 0.14 Ω ± 1%. The power output of each strip was considered to be equal as a result of this resistance uniformity. To ensure uniform current distribution through the foil and provide a terminal for lead wires, copper bus bars were soldered to the ends of the strips. Application of liquid flux with the solder and the usage of a hot plate created a clean electrical connection between the foil and the copper bus bar. Groves milled in the lexan backing provided space for the 1.58 mm thick copper bus bars in which to rest. By resting the bus bars in groves, the wrinkling of the foil where it met the end wall was minimized. Unlike the experimental setup used by Lyman et al. (2002), the end walls were built from high quality poplar wood instead of foam. The poplar wood end walls strengthened the milled lexan, which prepared the wall to be fitted with an IR camera window for further tests. An extraordinarily smooth surface was created on the poplar end walls by sanding and polyureathaning the wood several times.

C.2 Fin Material Selection and Design

The primary goal for the experimental design of the constant surface heat flux consisted of minimizing all experimental heat losses, thereby causing the applied heat flux along the tube wall to be removed entirely by convection. For this study, it was imperative that the fins only disturb the flowfield and not conduct heat away from the tube wall. Balsa wood was chosen as the material for the louver since it has a low thermal conductivity (k_b = 0.055 W/m·K). In addition to having a low thermal conductivity, balsa wood is extremely formable. The shapes of the entrance, reversal, and the exit louver were obtained by softening the balsa wood in a water bath and then by compressing the desired shape between metal louver models.

As mentioned in the paper, the louvers were calculated as being inefficient in conducting heat from the tube wall using the semi-infinite approximation to louver efficiency. To further prove that the louver efficiency can be calculated by using the semi-infinite approximation, the two-dimensional heat conduction equation was solved for fin's temperature rise, θ, where $\theta = \left(T_s - T_{in}\right)$.

$$\frac{\partial^2\theta}{\partial x^2} + \frac{\partial^2\theta}{\partial z^2} - \frac{2\overline{h}_f}{\partial k_b}\theta = 0 \qquad \text{(C.1)}$$

For the typical straight fin, it was assumed that a lumped capacitance model was adequate throughout the thickness of the louver. This reduced the problem into two dimensions. The boundary conditions assigned to the fin are as follows: First, since experiments conducted by Lyman et al. (2002) reported high heat transfer coefficients at the louver's leading edge, the free-stream temperature ($\theta = 0$) was prescribed along the leading edge. Second, it was assumed that the trailing edge was insulated since heat transfer coefficients within the vicinity of the trailing edge were predicted to be small. Third, the tube wall heat flux was applied at the base of the louver where the tube-fin junction is created. Fourth, a symmetry boundary condition was applied at the base of the louver opposite the tube wall. The average heat transfer coefficient measured by Lyman (2000) for the first louver is used in equation C.1. Since the louvers in this study were not heated, all the louvers in the test section were assumed to have an average heat transfer coefficient similar to that of the first louver. Figure C.1 summarizes these assumptions in the form of boundary conditions along the louver.

Temperature distributions were calculated to exist only within 10% of the total fin's length near the wall as shown in Figure C.2 for a streamwise louver position Lp/2. The maximum temperature rise in the fin was calculated to be approximately 2.7 ^{o}C for Re = 1016 and 1.3 ^{o}C for Re = 230. From both the results of the analytical solution and the fin effectiveness, the assumption that the fin's base is adiabatic to conduction heat loss is valid. Conduction losses through the fin's base, therefore, were not incorporated into the energy balance shown as equation 1 in the paper.

C.3 Design of Tube Wall Guard Heaters

As in all convective heat transfer experiments, a temperature difference must exist between the heat transfer surface and a reference temperature to quantify the heat transfer coefficient. For this study, the inlet temperature was chosen as the reference temperature. By heating the tube wall above the inlet temperature, the potential for conduction losses through the lexan supporting wall and radiation losses to the louvers both existed. Since the outer walls of the test section as well as the majority of the louver surfaces were approximately at room temperature, all modes of heat transfer were grounded to the same reference temperature. Initial calculations of the conductive heat losses were performed for various types of insulating materials for the isothermal tube wall boundary condition. The highest sensitivity to conductive losses, as well as radiation losses, occurred in the latter half of the channel ($0.5 < X < 1$) for Re = 230, where the tube wall boundary layer was the thickest. To minimize the ratio of conductive losses to the applied tube wall heat flux to within 10%, a thickness of 2 ft of amofoam was required in the region following the flow reversal louver ($0.5 < X < 1$).

To make the test section independent of thick insulative materials, limiting ranges of ΔT, and to prepare it for the constant heat flux tube wall, guard heaters were used to set new reference temperatures for radiation and conduction exchange. The new reference temperatures, T_{p1} and T_{p2}, were elevated above the room temperature and set as close as possible to the tube wall temperature by the guard heaters. Each guard heater consisted of two 14.7 ohm resistive patch heaters that were glued to an aluminum plate as shown in Figure C.3. The purpose of the aluminum plate was to smooth temperature gradients that might exist between the patch heaters. To reduce the power requirements of the patch heaters, the aluminum plate and patch heaters were encased in an insulating wooden box. Figure C.4 shows the thermal resistance network between the tube wall and the heated plates of both the guard heaters. If the guard heaters were not present, all modes of heat transfer would be referenced to the room temperature, as discussed earlier and as illustrated in Figure C.1. The amount of heat lost due to conduction through the lexan backing and foam sheet between the strip heaters and the conduction guard heaters is given by

$$q_c^{''} = \frac{T_w - T_{p1}}{\frac{L_{lexan}}{k_{lexan}} + \frac{L_{foam}}{k_{foam}}} \tag{C.2}$$

It should be noted that the thermocouples that measured T_w and T_{p1} were placed directly inline with each other, separated only by the thickness ($L_{lexan} + L_{foam}$). In this manner, any heat losses that influenced the tube wall's center thermocouples were directly accounted for. Note that the denominator of equation C.2 is simply represented by the equivalent thermal resistance, R_c, in the paper. For all Reynolds numbers tested, the fraction of lost heat flux due to conduction, χ_c, ranged from 1% to 10% along the tube wall. This minimal loss was obtained by adjusting the power input to the conduction guard heater until the temperature difference between the tube wall and the guard was reduced. To obtain this minimal loss, a current of approximately 0.5 amps was applied to both patch heaters of the conduction guard heater, resulting in a total power dissipation of 7.4 Watts.

In a similar manner, radiation losses to the milled lexan wall were thought to be minimized using the same technique. Initially, the silver painted louvers were assumed to be near perfect reflectors and only radiation losses to the milled lexan wall were considered. By using the radiation guard heater to heat the milled lexan wall, it was thought that all radiation losses were nearly negligible. Unfortunately, matching the temperatures between the tube wall and the milled lexan wall did not minimize all the radiation losses. To prove that radiation exchange between the tube wall and the milled lexan wall hardly occurs, the tube wall's temperature response to the milled lexan wall was recorded. Figure C.5 shows that the tube wall is unaffected by the heating of the milled lexan wall by the radiation guard heater. Estimations of the view factor, F_{ij}, between the tube wall and the milled lexan wall also suggested that radiation losses to the milled lexan wall were negligible. Further details on F_{ij} and the radiation losses to the louvers are discussed in Appendix D.

C.4 Instrumentation and Data Acquisition

Air was drawn through the test section by a Dayton model 3N1786 1.5 hp, 3-phase motor driving a 4C108 centrifugal fan. The motor was controlled by a Dayton 3HX72 AC inverter. With the AC inverter, the speed of the fan was controllable to a resolution of 0.01 Hz, which allowed all the studied flow rates to be accurately controlled.

The flow rate of the air through the test facility was measured using a Meriam 50MC2-2 laminar flow element (LFE). The LFE had the capability to measure a maximum flow rate of 2.787 m^3/min with a corresponding pressure drop of 203.2 mm H_20. By measuring the pressure drop across the LFE, the flow rate could be determined using the following calibration correlation provided by the manufacturer:

$$Q = 0.028317 \cdot (B \cdot \Delta P + C \cdot \Delta P^2) \cdot \frac{\mu_{std}}{\mu_{flow}} \ (m^3/min) \qquad (C.3)$$

where:

$B = 12.6198$
$C = -4.03588 \cdot 10^{-2}$

Q = Volumetric flow rate in actual cubic meters per minute
μ_{std} = Viscosity of flowing gas at 70º F in micropoise
μ_{flow} =Viscosity of flowing gas at flowing temperature in micropoise

Pressure drop measurements across the LFE were made with a Meriam 2110F digital manometer. With this manometer, a resolution of 0.51 mm H_20 was possible.

Type E thermocouples provided the main instrumentation for the tube wall heat transfer experiments. Temperature data was obtained by National Instruments data acquisition hardware and processed with National Instruments LabVIEW software. The data acquisition system for the thermocouple measurements consisted of an SCXI-1000 chassis into which three SXCI-1102 and one SXCI-1100 modules were inserted. This system allowed up to 96 thermocouples and 32 voltage drops to be monitored simultaneously. It should be noted that the SXCI-1100 module was needed for the implementation of the isothermal boundary condition. This simplified the isothermal tube wall experiments by allowing the voltage drop across each precision resistor to be monitored in real time. For the constant heat flux tube wall experiments, only one voltage drop was required to calculate the current flow through the constant width strip heaters.

Thermocouple accuracy was based on the precision of the measurements and any thermocouple biases that can occur. The thermocouples used in this study were made in a TigTech 1165RL thermocouple welder. One end of 28-AWG, type E thermocouple wire was striped of its insulation and held in the air-purged chamber of the TigTech. Argon gas purged the welding chamber of air during all welding processes. Welding the thermocouple junction in a noble gas environment insured that no impurities were introduced into the weld, thus reducing thermocouple biases. Only short lengths of the 28-AWG thermocouple wire were used in conjunction with 20-AWG, type E extension wire. A thermocouple panel served as the junction between the thermocouple and extension wire. By extending the thermocouple wire with extension wire, signal noise was significantly diminished. Unlike Lyman (2000), voltage bias differencing was unnecessary. Ice bath and room temperature tests indicated that thermocouple biases remained constant to within 0.19 ^{o}C over a range of 25 ^{o}C. After the test section came to steady state, 100 data points for each thermocouple were taken. The sample of 100 data points gave a precision uncertainty of less than 0.01 ^{o}C.

C.5 Experimental Uncertainty Analysis

The uncertainties of experimental quantities were computed by using the method presented by Kline and McClintock (1953). The uncertainty calculation method used involves calculating derivatives of the desired variable with respect to individual experimental quantities and applying known uncertainties. The general equation presented by Kline and McClintock showing the magnitude of the uncertainty in $R(u_R)$ is

$$u_R = \pm\left[\left(\frac{\partial R}{\partial x_1}u_{x1}\right)^2 + \left(\frac{\partial R}{\partial x_2}u_{x2}\right)^2 + \ldots + \left(\frac{\partial R}{\partial x_n}u_{xn}\right)^2\right]^{1/2} \tag{C.4}$$

where $R=R(x_1,x_2,\ldots,x_n)$ and x_n is the variables that affect the results of R.

Specific uncertainties of all of the experimental parameters for measurements taken at three different streamwise locations (X = 0.025, 0.45, and 0.975) are given in Tables C.1-C.6 for Re = 230 and 1016. Tables C.1-C.6 correspond to uncertainties calculated on strip heaters 1, 10, and 20. Precision uncertainties of the temperature measurements were based on a 95% confidence interval. The uncertainty analysis accounts for both the precision and bias uncertainties of the temperature measurements.

Although uncertainties for the entire tube wall are not reported, Tables C.1-C.6 show the maximum and minimum uncertainties calculated along the tube wall. For both Reynolds number cases, the highest uncertainty (8%) of the tube wall Nusselt number existed at strip 1. Uncertainty of the tube wall Nusselt at strip 1 was high due to a thin boundary layer, resulting in a small ΔT. Positions along the where the thickest tube wall boundary layer existed (strips 10 and 19) the uncertainties fell to 4.8% and 5.9% for Re = 1016 and 230, respectively. Small uncertainties in the Nusselt number at these positions can be attributed to the effectiveness of the conduction guard heater. As explained earlier, the conduction guard heater reduced the potential for conduction losses and reduced the uncertainty of q'' in the energy balance represented as equation 1 in the paper. While there was no method to further reduce the radiation losses to the louvers, radiation losses were dependent on computational predictions of χ_L, as mentioned in the paper. An uncertainty of 7% was used in regard to the value of χ_L. This uncertainty represents the final change in the tube wall Nusselt number between the last two mesh adaptations.

C.6 IR Camera Measurements

In addition to the use of thermocouples, infra-red (IR) camera measurements were attempted to spatially resolve the heat transfer occurring at one fin-tube junction for the experimental tests. The fin-tube junction of the fifth louver, where the flow was considered to be louver directed, was selected for the IR camera measurements. To prepare the test section for the IR camera, a viewing port was cut out of the milled lexan wall as illustrated in Figure C.6a. The viewing port housed the 11.4 cm diameter crystal fluoride IR camera window shown in Figure C.7. By cutting the viewing port, the milled slots that support the opposite ends of the louvers no longer existed, as shown in Figure C.6b. With the milled slots no longer present, the loose louver ends were held in compression against the IR camera glass with the aid of lexan clamps. Alignment of the louvers against the IR camera glass was very critical since the glass scratched easily and the louvers needed to be level for accurate imaging.

IR camera imaging of the tube wall's temperature was performed with a ThermaCAM® P20 Infra-red camera, which is shown in Figure C.8. A Close Up 200 lens, illustrated in Figure C.9, was attached to the built-in 24 deg camera lens. Without the Close Up lens, the built-in IR camera lens could not focus across the channel depth, d. Detailed information regarding both lenses was provided by the manufacturer and is given in Tables C.7-C.8. By attaching the Close-up lens, a spot size of approximately 0.2 mm was achieved. In comparison to the louver thickness and pitch, the spot size represents 9% of the louver's thickness and 0.7% of the louver's pitch. Good resolution was obtained around the tube-fin junction since the spot size represented a small fraction of the louver's thickness and pitch.

Although IR camera measurements are an excellent approach to spatially resolving the heat transfer occurring at the tube-fin junction, data was not obtained due to louver shadows. Note that post measurement analysis was simplified by conducting the experiment with the IR camera tilted at 27°. By tilting the IR camera, the louver pitch was orientated horizontally with respect to the field of view. As shown in Figure C.10, shadows of the louver's body blocked a considerable amount of the temperature data surrounding a particular louver. To overcome this obstacle, several pictures were taken around the louver. However, regions where the trailing edge of one louver meets the leading edge of the downstream louver were impossible to resolve. Such a region is circled in Figure C.10. During the experimental test, the IR camera was position several ways. For all positions, a significant shadow existed such that accurate measurements could not be made. As an example, it was considerably difficult to conclude whether augmentation at the leading edge of the louver cooled the tube wall or a shadow of the louver's body (which was mostly at the free stream temperature) influence the IR measurements.

C.7 References

Kline, S.J. and McClintock, F.A. 1953. Describing Uncertainties in Single Sample Experiments. *Mech. Engineering*. pp. 3-8.

Lyman, A. C., Stephan, R. A., Thole, K. A., Zhang, L., Memory, S. 2002. Scaling of HeatTransfer Coefficients Along Louvered Fins. *Experimental Thermal Fluid Science*. 26 (5): 547-563.

Lyman, A. 2000. Spatially Resolved Heat Transfer Studies in Louvered Fins for Compact Heat Exchangers, MSME Thesis.Virginia Tech, USA.

Table C.1 Uncertainty values of experimental variables for Strip 1 at Re = 1016.

Quantity	Value	Uncertainty	Units	% Uncertainty		Uncertainty Explaination
Heat Transfer Parameters						
Width of strip heater	0.028	0.0005	Meters	1.8	%	.5 mm from length measurments
Length of strip heater	0.26	0.0005	Meters	0.2	%	.5 mm from length measurments
Surface area of strip heater	0.00728	0.00013	m^2	1.8	%	.5 mm from length measurments
Precision resistor resistance	0.10	0.001	Ohms	1.0	%	uncertainity given from manufacturer
Strip heater resistance	0.14	0.01	Ohms	7.3	%	Solved fomr other variables $R_s = V_s/I_s$
Voltage drop across presicion resistor	0.345	0.001	Volts	0.3	%	DAQ
Equivalent thermal resistance of lexan and foam back-wall	0.69	0.003	W/m^2K	0.46	%	.5 mm from length measurments
Applied current to strip heaters	3.45	0.0359	Amps	1.0	%	Solved from other variables $I = V_p/R_p$
Applied heat flux to strip heaters	244.09	17.12	W/m^2	7.0	%	Solved from other variables $q_{power}" = I^2R_s/A_s$
Temperature difference between tube wall and conduction guard heater	0.88	0.20	°C	22.9	%	Thermocouple error
Temperature difference between-tube wall and free stream	12.20	0.20	°C	1.6	%	Thermocouple error
Heat flux lost from tube-wall due to radiation	44.33	0.7000	W/m^2	1.58	%	CFD grid adaptions
Heat flux lost from tube wall through backside of test section	1.27	0.29	W/m^2	22.9	%	Solved from other variables $q_c" = \Delta T/R_c$
Local tube wall transfer coefficient	16.27	1.43	$W/m^2\,K$	8.8	%	Solved from other variables $(h = q"_{power} - q"_c - q"_r)/\Delta T$
Local tube wall Nusselt number	18.76	1.41		7.5	%	Solved from other variables $Nu = h \cdot Lp/k$
Test Facility Parameters						
Prandtl Number	0.711	0.000		0.00	%	Known value at room temp = 300K
Viscosity, μ	1.846E-05	0.000	$N{\cdot}s/m^2$	0.00	%	Known value at room temp = 300K
Density, ρ	1.170	0.000	kg/m^3	0.00	%	Known value at room temp = 300K
Specific Heat of air, c_p	1005.00	0.000	kJ/(kg K)	0.00	%	Known value at room temp = 300K
Louver Pitch, Lp	0.028	0.001	m	1.79	%	.5 mm from length measurments
Inlet Area	0.034	0.00013	m^2	0.38	%	.5 mm from length measurments
Pressure Drop Across the LFE	3.340	0.020	in H_20	0.60	%	0.02 in accuracy of nanometer
Pressure Drop Across the LFE	84.836	0.508	mm H_20	0.60	%	Unit conversion
Volumetric Flow Rate Through the Flow Facility	41.664	0.250	ACFM	0.60	%	Correlation from LFE
Volumetric Flow Rate Through the Flow Facility	0.020	0.00012	m^3/s	0.60	%	Unit conversion
Mass Flow Rate Through the Flow Facility	0.023	0.00014	kg/s	0.60	%	Multiply volumetric flow rate by density
Inlet Velocity	0.577	0.00410	m/s	0.71	%	Divide volumetric flow rate by inlet area
Inlet Reynolds number	1020	19.67		1.93	%	Solved from other variables $Re = \rho \cdot Uin \cdot Lp/\mu$

Table C.2 Uncertainty values of experimental variables for Strip 10 at Re = 1016.

Quantity	Value	Uncertainty	Units	% Uncertainty		Uncertainty Explaination
Heat Transfer Parameters						
Width of strip heater	0.028	0.0005	Meters	1.8	%	.5 mm from length measurments
Length of strip heater	0.26	0.0005	Meters	0.2	%	.5 mm from length measurments
Surface area of strip heater	0.00728	0.00013	m^2	1.8	%	.5 mm from length measurments
Precision resistor resistance	0.10	0.001	Ohms	1.0	%	uncertainity given from manufacturer
Strip heater resistance	0.14	0.01	Ohms	7.3	%	Solved fomr other variables $R_s = V_s/I_s$
Voltage drop across presicion resistor	0.345	0.001	Volts	0.3	%	DAQ
Equivalent thermal resistance of lexan and foam back-wall	0.69	0.003	W/m^2K	0.46	%	.5 mm from length measurments
Applied current to strip heaters	3.45	0.0359	Amps	1.0	%	Solved from other variables $I = V_p/R_p$
Applied heat flux to strip heaters	244.09	17.12	W/m^2	7.0	%	Solved from other variables $q_{power}'' = I^2R_s/A_s$
Temperature difference between tube wall and conduction guard heater	12.10	0.20	^oC	1.7	%	Thermocouple error
Temperature difference between-tube wall and free stream	24.30	0.20	^oC	0.8	%	Thermocouple error
Heat flux lost from tube-wall due to radiation	76.64	0.7000	W/m^2	0.91	%	CFD grid adaptions
Heat flux lost from tube wall through backside of test section	17.56	0.30	W/m^2	1.7	%	Solved from other variables $q_c'' = \Delta T/R_c$
Local tube wall transfer coefficient	6.17	0.71	$W/m^2\ K$	11.5	%	Solved from other variables $(h = q''_{power} - q''_c - q''_r)/\Delta T$
Local tube wall Nusselt number	7.11	0.34		4.8	%	Solved from other variables $Nu = h \cdot Lp/k$
Test Facility Parameters						
Prandtl Number	0.711	0.000		0.00	%	Known value at room temp = 300K
Viscosity, μ	1.846E-05	0.000	$N{\cdot}s/m^2$	0.00	%	Known value at room temp = 300K
Density, ρ	1.170	0.000	kg/m^3	0.00	%	Known value at room temp = 300K
Specific Heat of air, c_p	1005.00	0.000	kJ/(kg K)	0.00	%	Known value at room temp = 300K
Louver Pitch, Lp	0.028	0.001	m	1.79	%	.5 mm from length measurments
Inlet Area	0.034	0.00013	m^2	0.38	%	.5 mm from length measurments
Pressure Drop Across the LFE	3.340	0.020	in H_20	0.60	%	0.02 in accuracy of nanometer
Pressure Drop Across the LFE	84.836	0.508	mm H_20	0.60	%	Unit conversion
Volumetric Flow Rate Through the Flow Facility	41.664	0.250	ACFM	0.60	%	Correlation from LFE
Volumetric Flow Rate Through the Flow Facility	0.020	0.00012	m^3/s	0.60	%	Unit conversion
Mass Flow Rate Through the Flow Facility	0.023	0.00014	kg/s	0.60	%	Multiply volumetric flow rate by density
Inlet Velocity	0.577	0.00410	m/s	0.71	%	Divide volumetric flow rate by inlet area
Inlet Reynolds number	1020	19.67		1.93	%	Solved from other variables $Re = \rho \cdot Uin \cdot Lp/\mu$

Table C.3 Uncertainty values of experimental variables for Strip 20 at Re = 1016.

Quantity	Value	Uncertainty	Units	% Uncertainty		Uncertainty Explaination
Heat Transfer Parameters						
Width of strip heater	0.028	0.0005	Meters	1.8	%	.5 mm from length measurments
Length of strip heater	0.26	0.0005	Meters	0.2	%	.5 mm from length measurments
Surface area of strip heater	0.00728	0.00013	m^2	1.8	%	.5 mm from length measurments
Precision resistor resistance	0.10	0.001	Ohms	1.0	%	uncertainity given from manufacturer
Strip heater resistance	0.13	0.01	Ohms	7.7	%	Solved fomr other variables $R_s = V_s/I_s$
Voltage drop across presicion resistor	0.345	0.001	Volts	0.3	%	DAQ
Equivalent thermal resistance of lexan and foam back-wall	0.69	0.003	W/m^2K	0.46	%	.5 mm from length measurments
Applied current to strip heaters	3.45	0.0359	Amps	1.0	%	Solved from other variables $I = V_p/R_p$
Applied heat flux to strip heaters	226.65	17.05	W/m^2	7.5	%	Solved from other variables $q_{power}" = I^2R_s/A_s$
Temperature difference between tube wall and conduction guard heater	10.20	0.20	^oC	2.0	%	Thermocouple error
Temperature difference between-tube wall and free stream	23.70	0.20	^oC	0.8	%	Thermocouple error
Heat flux lost from tube-wall due to radiation	81.59	0.7000	W/m^2	0.86	%	CFD grid adaptions
Heat flux lost from tube wall through backside of test section	14.80	0.30	W/m^2	2.0	%	Solved from other variables $q_c" = \Delta T/R_c$
Local tube wall transfer coefficient	5.50	0.72	$W/m^2 K$	13.1	%	Solved from other variables $(h = q"_{power} - q"_c - q"_r)/\Delta T$
Local tube wall Nusselt number	6.34	0.35		5.6	%	Solved from other variables $Nu = h \cdot Lp/k$
Test Facility Parameters						
Prandtl Number	0.711	0.000		0.00	%	Known value at room temp = 300K
Viscosity, μ	1.846E-05	0.000	$N \cdot s/m^2$	0.00	%	Known value at room temp = 300K
Density, ρ	1.170	0.000	kg/m^3	0.00	%	Known value at room temp = 300K
Specific Heat of air, c_p	1005.00	0.000	kJ/(kg K)	0.00	%	Known value at room temp = 300K
Louver Pitch, Lp	0.028	0.001	m	1.79	%	.5 mm from length measurments
Inlet Area	0.034	0.00013	m^2	0.38	%	.5 mm from length measurments
Pressure Drop Across the LFE	3.340	0.020	in H_20	0.60	%	0.02 in accuracy of nanometer
Pressure Drop Across the LFE	84.836	0.508	mm H_20	0.60	%	Unit conversion
Volumetric Flow Rate Through the Flow Facility	41.664	0.250	ACFM	0.60	%	Correlation from LFE
Volumetric Flow Rate Through the Flow Facility	0.020	0.00012	m^3/s	0.60	%	Unit conversion
Mass Flow Rate Through the Flow Facility	0.023	0.00014	kg/s	0.60	%	Multiply volumetric flow rate by density
Inlet Velocity	0.577	0.00410	m/s	0.71	%	Divide volumetric flow rate by inlet area
Inlet Reynolds number	1020	19.67		1.93	%	Solved from other variables $Re = \rho \cdot Uin \cdot Lp/\mu$

Table C.4 Uncertainty values of experimental variables for Strip 1 at Re = 230.

Quantity	Value	Uncertainty	Units	% Uncertainty		Uncertainty Explaination
Heat Transfer Parameters						
Width of strip heater	0.028	0.0005	Meters	1.8	%	.5 mm from length measurments
Length of strip heater	0.26	0.0005	Meters	0.2	%	.5 mm from length measurments
Surface area of strip heater	0.00728	0.00013	m^2	1.8	%	.5 mm from length measurments
Precision resistor resistance	0.10	0.001	Ohms	1.0	%	uncertainity given from manufacturer
Strip heater resistance	0.14	0.01	Ohms	7.1	%	Solved fomr other variables $R_s = V_s/I_s$
Voltage drop across presicion resistor	0.242	0.001	Volts	0.4	%	DAQ
Equivalent thermal resistance of lexan and foam back-wall	0.69	0.003	W/m^2K	0.46	%	.5 mm from length measurments
Applied current to strip heaters	2.42	0.0262	Amps	1.1	%	Solved from other variables $I = V_p/R_p$
Applied heat flux to strip heaters	96.85	8.53	W/m^2	8.8	%	Solved from other variables $q_{power}" = I^2R_s/A_s$
Temperature difference between tube wall and conduction guard heater	2.55	0.20	^oC	7.8	%	Thermocouple error
Temperature difference between-tube wall and free stream	8.74	0.20	^oC	2.3	%	Thermocouple error
Heat flux lost from tube-wall due to radiation	27.12	0.70	W/m^2	2.58	%	CFD grid adaptions
Heat flux lost from tube wall through backside of test section	3.70	0.29	W/m^2	7.9	%	Solved from other variables $q_c" = \Delta T/R_c$
Local tube wall transfer coefficient	7.56	0.99	W/m^2 K	13.2	%	Solved from other variables $(h = q"_{power} - q"_c - q"_r)/\Delta T$
Local tube wall Nusselt number	8.71	0.67		7.7	%	Solved from other variables $Nu = h \cdot Lp/k$
Test Facility Parameters						
Prandtl Number	0.711	0.000		0.00	%	Known value at room temp = 300K
Viscosity, μ	1.846E-05	0.000	$N \cdot s/m^2$	0.00	%	Known value at room temp = 300K
Density, ρ	1.170	0.000	kg/m^3	0.00	%	Known value at room temp = 300K
Specific Heat of air, c_p	1005.00	0.000	kJ/(kg K)	0.00	%	Known value at room temp = 300K
Louver Pitch, Lp	0.028	0.001	m	1.79	%	.5 mm from length measurments
Inlet Area	0.034	0.00013	m^2	0.38	%	.5 mm from length measurments
Pressure Drop Across the LFE	0.760	0.020	in H_20	2.63	%	0.02 in accuracy of nanometer
Pressure Drop Across the LFE	19.304	0.508	mm H_20	2.63	%	Unit conversion
Volumetric Flow Rate Through the Flow Facility	9.566	0.252	ACFM	2.63	%	Correlation from LFE
Volumetric Flow Rate Through the Flow Facility	0.005	0.00012	m^3/s	2.63	%	Unit conversion
Mass Flow Rate Through the Flow Facility	0.005	0.00014	kg/s	2.63	%	Multiply volumetric flow rate by density
Inlet Velocity	0.132	0.00352	m/s	2.66	%	Divide volumetric flow rate by inlet area
Inlet Reynolds number	234	7.51		3.21	%	Solved from other variables $Re = \rho \cdot Uin \cdot Lp/\mu$

Table C.5 Uncertainty values of experimental variables for Strip 10 at Re = 230.

Heat Transfer Parameters						
Quantity	Value	Uncertainty	Units	% Uncertainty		Uncertainty Explaination
Width of strip heater	0.028	0.0005	Meters	1.8	%	.5 mm from length measurments
Length of strip heater	0.26	0.0005	Meters	0.2	%	.5 mm from length measurments
Surface area of strip heater	0.00728	0.00013	m^2	1.8	%	.5 mm from length measurments
Precision resistor resistance	0.10	0.001	Ohms	1.0	%	uncertainity given from manufacturer
Strip heater resistance	0.14	0.01	Ohms	7.1	%	Solved fomr other variables $R_s = V_s/I_s$
Voltage drop across presicion resistor	0.242	0.001	Volts	0.4	%	DAQ
Equivalent thermal resistance of lexan and foam back-wall	0.69	0.003	W/m^2K	0.46	%	.5 mm from length measurments
Applied current to strip heaters	2.42	0.0262	Amps	1.1	%	Solved from other variables $I = V_p/R_p$
Applied heat flux to strip heaters	96.85	8.53	W/m^2	8.8	%	Solved from other variables $q_{power}" = I^2R_s/A_s$
Temperature difference between tube wall and conduction guard heater	5.00	0.20	^oC	4.0	%	Thermocouple error
Temperature difference between-tube wall and free stream	16.20	0.20	^oC	1.2	%	Thermocouple error
Heat flux lost from tube-wall due to radiation	44.55	0.70	W/m^2	1.57	%	CFD grid adaptions
Heat flux lost from tube wall through backside of test section	7.26	0.29	W/m^2	4.0	%	Solved from other variables $q_c" = \Delta T/R_c$
Local tube wall transfer coefficient	2.78	0.53	$W/m^2\,K$	19.0	%	Solved from other variables $(h = q"_{power} - q"_c - q"_r)/\Delta T$
Local tube wall Nusselt number	3.21	0.19		5.9	%	Solved from other variables $Nu = h \cdot Lp/k$
Test Facility Parameters						
Prandtl Number	0.711	0.000		0.00	%	Known value at room temp = 300K
Viscosity, μ	1.846E-05	0.000	$N{\cdot}s/m^2$	0.00	%	Known value at room temp = 300K
Density, ρ	1.170	0.000	kg/m^3	0.00	%	Known value at room temp = 300K
Specific Heat of air, c_p	1005.00	0.000	kJ/(kg K)	0.00	%	Known value at room temp = 300K
Louver Pitch, Lp	0.028	0.001	m	1.79	%	.5 mm from length measurments
Inlet Area	0.034	0.00013	m^2	0.38	%	.5 mm from length measurments
Pressure Drop Across the LFE	0.760	0.020	in H_20	2.63	%	0.02 in accuracy of nanometer
Pressure Drop Across the LFE	19.304	0.508	mm H_20	2.63	%	Unit conversion
Volumetric Flow Rate Through the Flow Facility	9.566	0.252	ACFM	2.63	%	Correlation from LFE
Volumetric Flow Rate Through the Flow Facility	0.005	0.00012	m^3/s	2.63	%	Unit conversion
Mass Flow Rate Through the Flow Facility	0.005	0.00014	kg/s	2.63	%	Multiply volumetric flow rate by density
Inlet Velocity	0.132	0.00352	m/s	2.66	%	Divide volumetric flow rate by inlet area
Inlet Reynolds number	234	7.51		3.21	%	Solved from other variables $Re = \rho \cdot Uin \cdot Lp/\mu$

Table C.6 Uncertainty values of experimental variables for Strip 20 at Re = 230.

Heat Transfer Parameters						
Quantity	**Value**	**Uncertainty**	**Units**	**% Uncertainty**		**Uncertainty Explaination**
Width of strip heater	0.028	0.0005	Meters	1.8	%	.5 mm from length measurments
Length of strip heater	0.26	0.0005	Meters	0.2	%	.5 mm from length measurments
Surface area of strip heater	0.00728	0.00013	m^2	1.8	%	.5 mm from length measurments
Precision resistor resistance	0.10	0.001	Ohms	1.0	%	uncertainity given from manufacturer
Strip heater resistance	0.14	0.01	Ohms	7.1	%	Solved fomr other variables $R_s = V_s/I_s$
Voltage drop across presicion resistor	0.242	0.001	Volts	0.4	%	DAQ
Equivalent thermal resistance of lexan and foam back-wall	0.69	0.003	W/m^2K	0.46	%	.5 mm from length measurments
Applied current to strip heaters	2.42	0.0262	Amps	1.1	%	Solved from other variables $I = V_p/R_p$
Applied heat flux to strip heaters	89.90	8.53	W/m^2	9.5	%	Solved from other variables $q_{power}" = I^2R_s/A_s$
Temperature difference between tube wall and conduction guard heater	4.50	0.20	^oC	4.4	%	Thermocouple error
Temperature difference between-tube wall and free stream	16.10	0.20	^oC	1.2	%	Thermocouple error
Heat flux lost from tube-wall due to radiation	48.55	0.70	W/m^2	1.44	%	CFD grid adaptions
Heat flux lost from tube wall through backside of test section	6.53	0.29	W/m^2	4.5	%	Solved from other variables $q_c" = \Delta T/R_c$
Local tube wall transfer coefficient	2.16	0.53	W/m^2 K	24.6	%	Solved from other variables $(h = q"_{power} - q"_c - q"_r)/\Delta T$
Local tube wall Nusselt number	2.49	0.19		7.6	%	Solved from other variables $Nu = h \cdot Lp/k$
Test Facility Parameters						
Prandtl Number	0.711	0.000		0.00	%	Known value at room temp = 300K
Viscosity, μ	1.846E-05	0.000	$N \cdot s/m^2$	0.00	%	Known value at room temp = 300K
Density, ρ	1.170	0.000	kg/m^3	0.00	%	Known value at room temp = 300K
Specific Heat of air, c_p	1005.00	0.000	kJ/(kg K)	0.00	%	Known value at room temp = 300K
Louver Pitch, Lp	0.028	0.001	m	1.79	%	.5 mm from length measurments
Inlet Area	0.034	0.00013	m^2	0.38	%	.5 mm from length measurments
Pressure Drop Across the LFE	0.760	0.020	in H_20	2.63	%	0.02 in accuracy of nanometer
Pressure Drop Across the LFE	19.304	0.508	mm H_20	2.63	%	Unit conversion
Volumetric Flow Rate Through the Flow Facility	9.566	0.252	ACFM	2.63	%	Correlation from LFE
Volumetric Flow Rate Through the Flow Facility	0.005	0.00012	m^3/s	2.63	%	Unit conversion
Mass Flow Rate Through the Flow Facility	0.005	0.00014	kg/s	2.63	%	Multiply volumetric flow rate by density
Inlet Velocity	0.132	0.00352	m/s	2.66	%	Divide volumetric flow rate by inlet area
Inlet Reynolds number	234	7.51		3.21	%	Solved from other variables $Re = \rho \cdot Uin \cdot Lp/\mu$

Table C.7 ThermalCAM® P20 Optics Technical Data

Lens (deg)	HFOV (deg)	VFOV (deg)	IFOV (mrad)	Min. focus (m)	Length (cm)	Diameter (cm)	Weight (kg)
24 std.	24	18	1.3	0.3	-	-	-
Close Up 200	64mm	48mm	200 μm	0.15	2.4	7.1	0.14

Table C.8 Close-up Optics Data – (mm) inches

Lens	Spot Size	Working Distance	FOV (Hor. x Vert.)	Remarks
Close Up 200	(0.2) 0.008	(150) 5.9	(64 x 48) 2.5 x 1.9	Use with 24 deg. lens

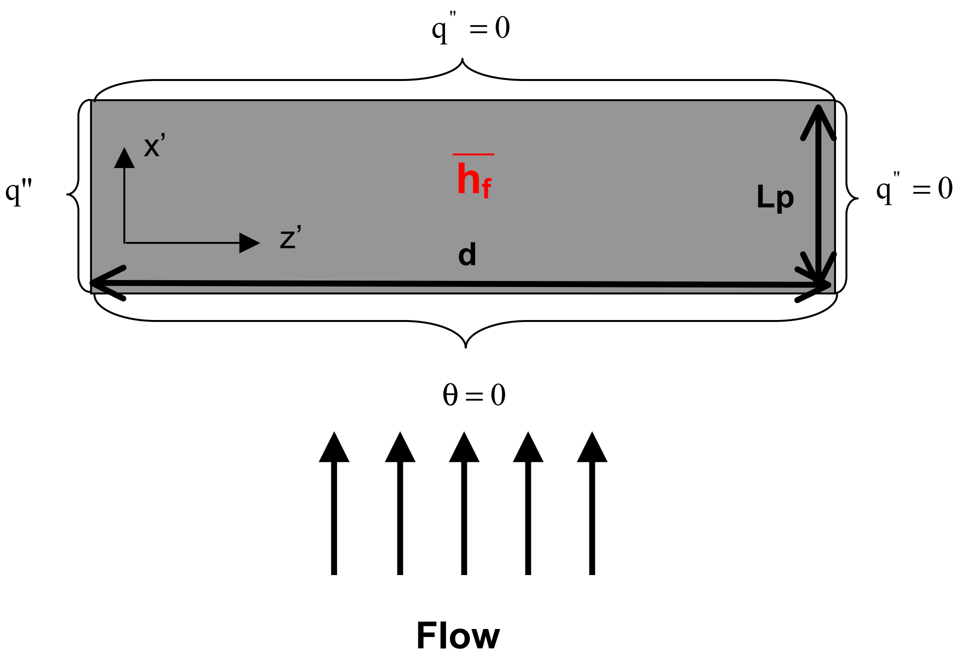

Figure C.1 Illustration of the boundary conditions placed on the two-dimensional fin.

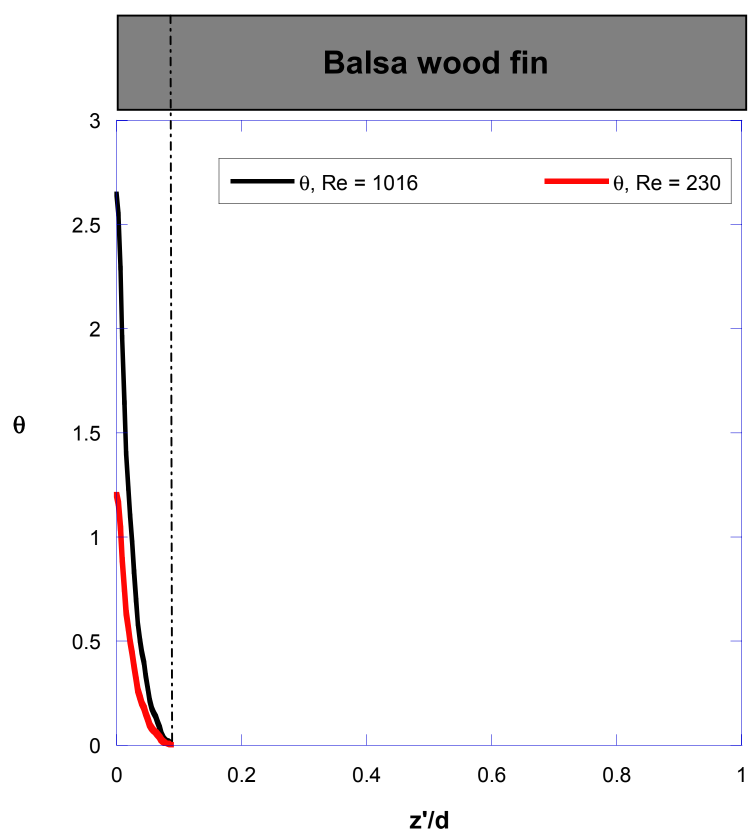

Figure C.2 Temperature distribution of a fin taken at $L_p/2$.

Figure C.3 Picture of the patch heaters and the aluminum plate used inside the guard heater assembly.

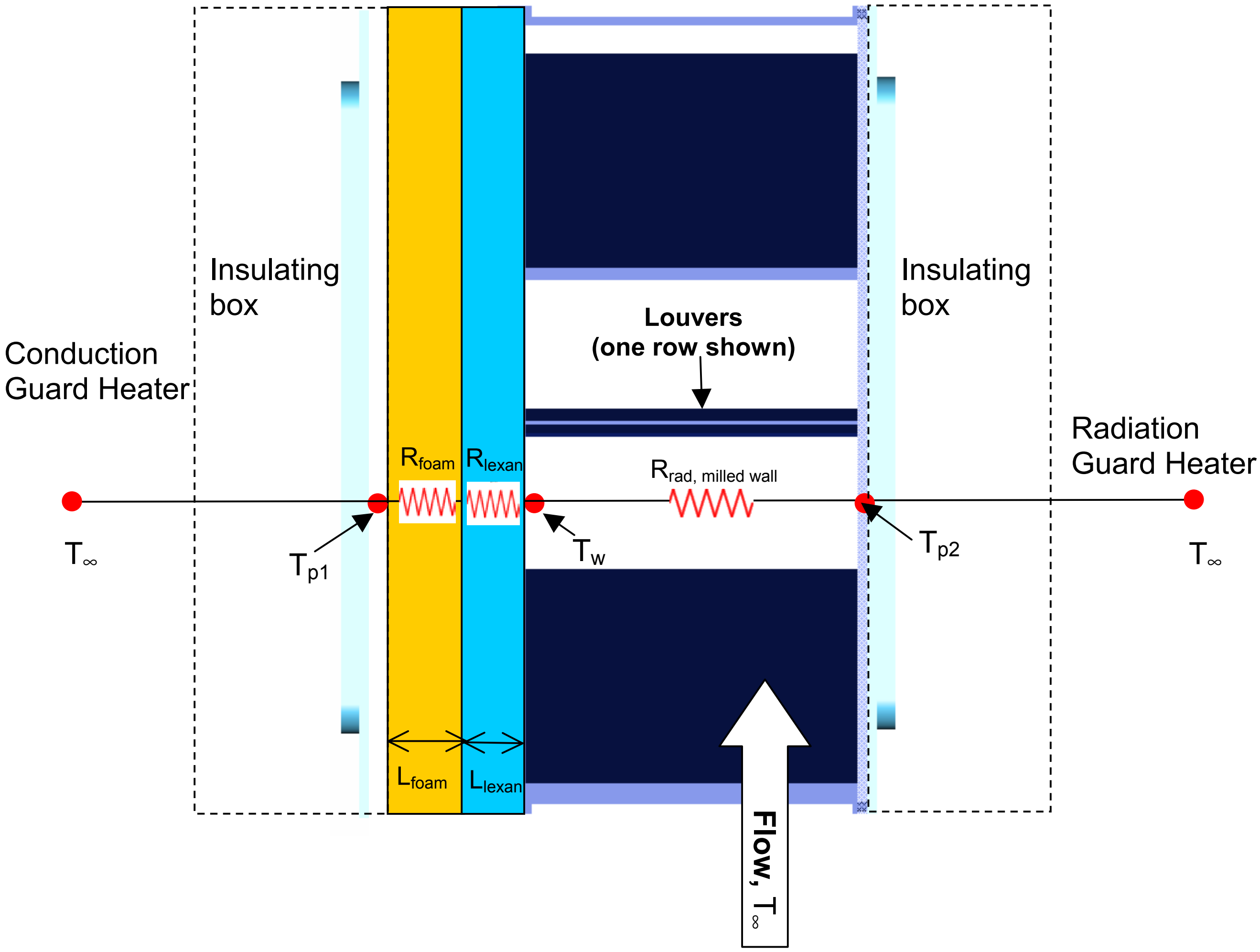

Figure C.4 Drawing of the test section detailing the thermal resistance network between the tube wall and the guard heaters.

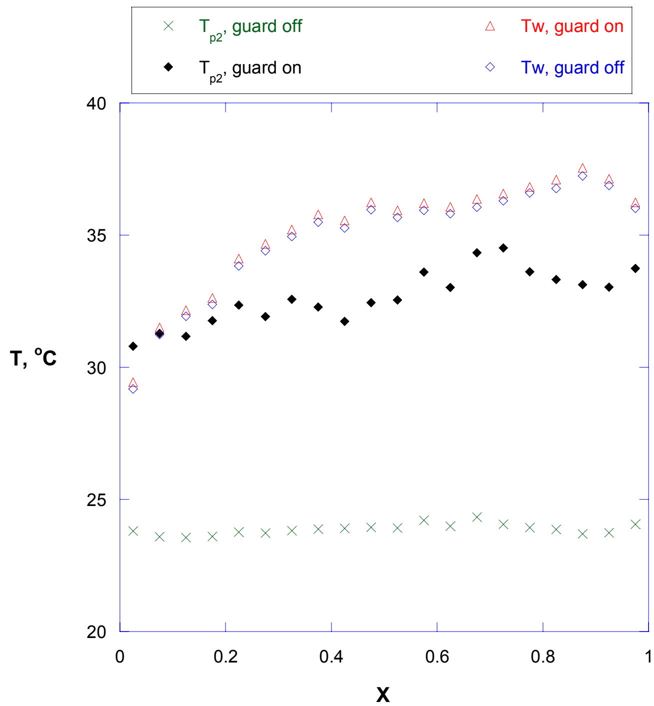

Figure C.5 Tube wall temperature responses to the radiation guard heater, Re = 230.

a)

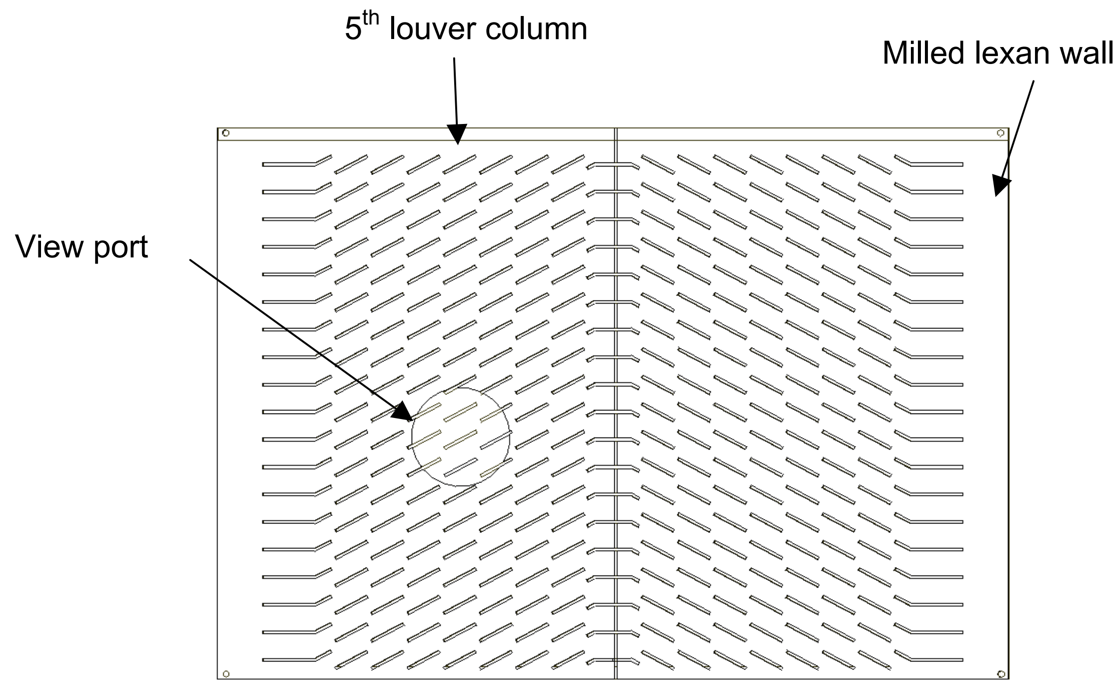

b)

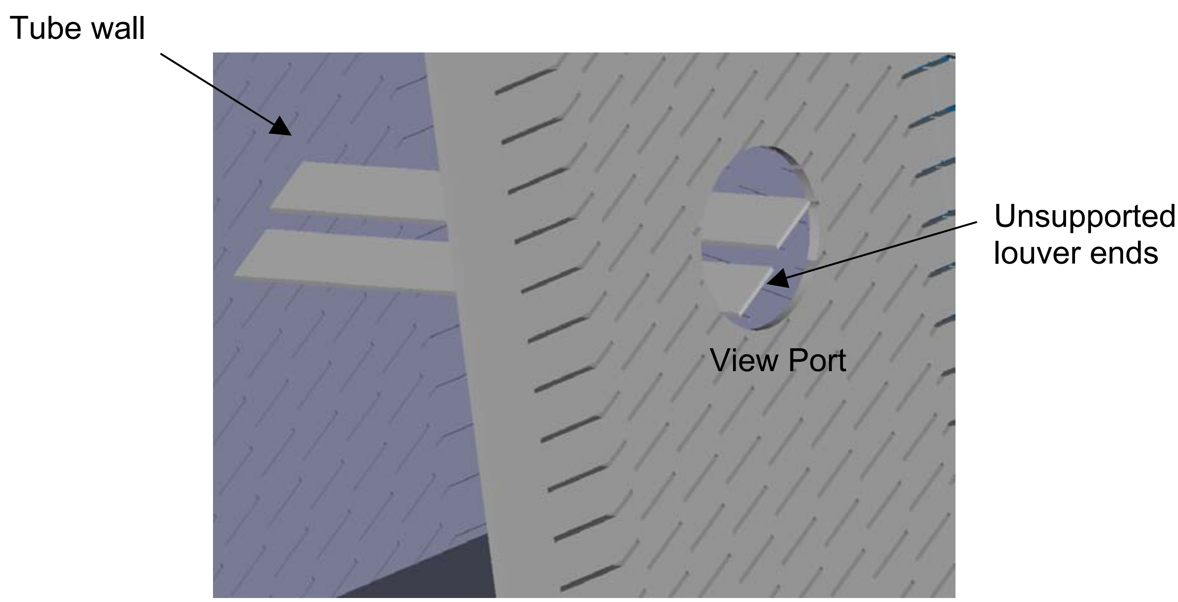

Figures C.6a-b Illustrations of the view port used for the IR camera measurements of tube-fin junction at the 5th louver.

Figure C.7 Picture of the IR camera glass that was mounted in the view port.

Figure C.8 Picture of the ThermalCAM® P20 IR camera.

Figure C.9 Picture of the Close Up 200 lens attached to the built-in 24 deg IR camera lens.

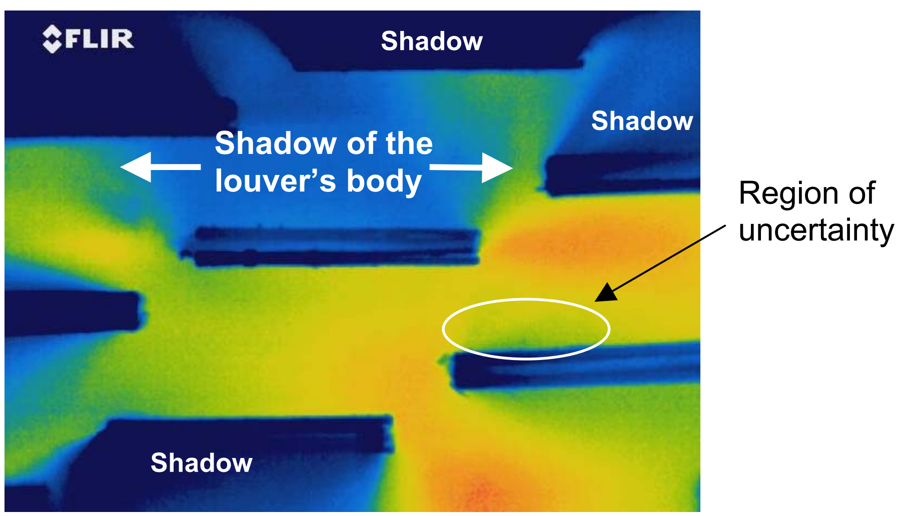

Figure C.10 IR camera image of the tube wall detailing a region near the leading edge of a louver where the louver's body blurred the temperature data.

Appendix D

Data Analysis Methods

This appendix further expands on how the heat transfer data presented in the paper for the constant heat flux tube wall was analyzed. As mentioned earlier, radiation and conduction heat losses made determining the heat flux removed by convection difficult. The following section, Section D.1, discusses the derivation of the energy balance shown as equation 1 in the paper. Since the energy balance derived in Section D.1 is highly dependent on the radiation losses to the louver surfaces, Section D.2 analyzes the three methods the radiation losses were quantified and discuss the final method chosen. Finally, Section D.3 discusses the experimental tests used to benchmark the test section. The conclusion that the heat transfer results are repeatable, with only weak buoyancy effects existing at Re =230, will be established.

D.1 Description of the heat transfer coefficient

Heat transfer caused by fluid movement is defined as convection. For an object subjected to convection, the change of temperature over the length (temperature gradient) is dependent on the rate at which the fluid carries the heat away. The rate at which heat is removed is defined as the convective heat transfer coefficient. This process is described by Newton's law of cooling, which is typically written as

$$h = \frac{q''}{T_w - T_{in}} \tag{D.1}$$

For this study, the tube wall is the surface being subjected to convection. Thermocouples measured the local tube wall temperatures, which are represented as T_w in the denominator of equation D.1. The proper convective heat flux was determined with the aid of computational simulations to estimate the tube wall radiation to the louvers.

The total power dissipation of the strip heaters was calculated from

$$q''_{power} = \frac{I^2 R_s}{A_s} \qquad \text{(D.2)}$$

To determine the convected heat transferred from the tube wall to the surrounding flowfield, any heat losses other than convection needed to be subtracted from equation D.2 before the heat transfer coefficients could be calculated from equation D.1. Equation C.2 accounted for any conduction losses that remained between the tube wall and the conduction guard heater. Radiation losses, on the other hand, were not dominated by that to the opposite wall with the radiation guard heater. Rather, the radiation losses to the louvers dominated.

As mentioned earlier, numerical predictions of the amount of radiation losses to the louvers was required due to the geometric complexity. From the computational predictions, the fraction of the total applied heat flux to louver radiation losses, χ_L, was used to account for radiation losses to the louvers. The energy balance used to determine the tube wall convective heat transfer is

$$h = \frac{q''}{(T_w - T_{in})} = \frac{q''_{power} - q''_c - q''_r}{(T_w - T_{in})} = \frac{\dfrac{I^2 R}{A_t} - \left[\dfrac{T_w - T_{p1}}{R_c}\right] - \left[q''_{power}(\chi_w + \chi_L)\right]}{(T_w - T_{in})} \qquad \text{(D.3)}$$

Although the milled lexan wall had a greater emissivity ($\varepsilon_w = 0.88$) then the louvers ($\varepsilon_L = 0.3$), the view factor between the tube wall and the milled lexan wall was estimated to be considerably small. By assuming that any two louvers make up a rectangular box with dimensions (F_p X L_p X d), the view factor was estimated to be $F_{ij} = 0.05$ (Incropera and DeWitt, 1996). A small view factor suggested that radiation exchange between the tube wall and the milled lexan wall was negligible and agrees with the experimental findings described in Section C.3 of Appendix C. The fraction of heat loss to the milled lexan, χ_w, therefore was dropped from the energy balance, reducing equation D.3 to

$$h = \frac{q''}{(T_w - T_{in})} = \frac{q''_{power} - q''_c - q''_r}{(T_w - T_{in})} = \frac{\frac{I^2 R}{A_t} - \left[\frac{T_w - T_{p1}}{R_c}\right] - \left[(\chi_L) q''_{power}\right]}{(T_w - T_{in})} \tag{D.4}$$

In order for the heat transfer coefficients of the tube wall to be applicable to other compact heat exchanger geometries, all measurements and predictions of the heat transfer coefficient are presented in terms of the Nusselt number; the Nusselt number is a non-dimensional version of the heat transfer coefficient and is defined as follows

$$Nu = \frac{h \cdot Lp}{k} \tag{D.5}$$

D.2 Modeling the Radiation Transport Equation

Figure D.1 shows the experimental measurements and computational predictions of the tube wall Nusselt number for Re = 230 where only radiation losses to the milled lexan wall for which were accounted. The minimized radiation losses to the milled lexan wall are plotted in Figure D.2 in terms of χ_w as well as the conduction losses, χ_C. Although the radiation losses to the milled lexan wall were nearly zero (which was set by the radiation guard heater), the measured Nusselt number in Figure D.1 is much higher than the predicted values. Similar trends were found for all Reynolds numbers and thus became the motivation for modeling the radiation exchange between the louver surfaces and the tube wall.

Initially, the tube wall radiation losses to the louver surfaces were estimated from Incropera and DeWitt, 1996. Since the louvers meet the tube wall at right angles, the view factor for perpendicular rectangles with a common edge was used (see Figure D.3). The louver's surface temperature for this estimation was set equal to the inlet temperature for reasons already discussed in Section C.2 in Appendix C. This estimation did not account for radiation losses towards the leading and trailing edges of the louvers as shown in Figure D.3. Calculations of χ_L based on this method over predicted radiation losses and did not account for the view factors between entrance, reversal, and exit louvers.

More accurate estimations on the radiation losses to the louver surfaces had been obtained by solving the multi-mode (convection and radiation) heat transfer problem. The multi-mode heat transfer problem was solved by modeling the radiation transport equation in Fluent 6.0, as previously mentioned in the paper. The radiation transport equation is given by

$$\frac{\partial I}{\partial x_i} + \underbrace{(\alpha + \sigma_s) I(r,s)}_{\text{absorption}} = \underbrace{\alpha n^2 \frac{\sigma T^4}{\pi}}_{\text{emission}} + \underbrace{\frac{\sigma_s}{4\pi}\int_0^{4\pi} I(r,s')\Theta(s \cdot s')\,d\Omega'}_{\text{Gain by scattering into the s-direction}} \qquad \text{(D.6)}$$

Equation D.6 represents the change in intensity along a path x, $\frac{\partial I}{\partial x_i}$, in the solid angle $d\Omega'$ about the direction of s´. The scattering coefficient for air, σ_s was considered to be zero since air is an optically thin medium. Each of the louver fin surfaces was assumed to be diffuse and the absorption coefficient, α, was set equal to ε_L. Modeling equation D.6 within the computational domain accounted for path dependent radiation released from the tube wall. In addition, radiation effects between the entrance, reversal, and exit louvers could be estimated. Fluent 6.0 discretizes equation D.6 into a number of different models. For this study, the following two models were applied: 1) The P-1 model, which integrates out directional dependence in equation D.6 and 2) The DO model, the full form discretized version of equation D.6. It was expected that the P-1 would render poor results since direction dependence was not included. By not including directional dependence, the radiation transport equation is reduced to a diffusion equation for incident radiation. Simply stated, a diffusion equation for incident radiation sums the amount of radiation which is absorbed and emitted and equates that sum to the radiation which is scattered. Usually, for radiation mediums which are optically thick, such as smoke and soot, directional dependence is negligible. In other words, radiation emitted into an optically thick medium is absorbed and scattered by the medium, with solid surfaces having no affect on the radiation transport. However, unlike smoke and soot, the air drawn through the louver array is considered optically thin. The P-1 model was only studied since convergence occurred quickly and it produced another benchmark for the DO model.

To adequately estimate the radiation exchange between the tube wall and the louver surfaces, the DO model was incorporated into the computational energy equation. It should be noted that the grid adaptations mentioned in the paper were performed without the DO model. Since the flowfield was already adapted upon, a fairly grid independent convective environment was believed to exist. This convective environment governed the temperature gradients along the tube wall which served as the potential for radiation exchange. Although the DO model took considerably longer to solve than the P-1 model, the predicted results of tube wall radiation losses were much more accurate. The DO model's ability to predict repeatable results for different surface to air temperatures at Re = 230, as discussed in the paper, placed confidence in the model to accurately predict the tube wall radiation losses for all the Reynolds numbers studied. Figure D.4 compares the predictions χ_L for the three methods discussed in this section. Note that the DO model predicts smaller values of χ_L in regions where high gradients in the heat transfer coefficient were predicted to exist, particularly near the reversal louver where the flow separates.

D.3 Benchmarking of the Test Section

From a flow standpoint, the facility was constructed exactly the same as reported by Lyman, 2000, therefore flow benchmarking was not repeated. The primary benchmarking for the test section included repeatability and periodicity measurements of the tube wall Nusselt number. Repeatability of the heat transfer measurements was established numerous times over the course of testing. In order to fully understand the heat transfer results, it was important to determine if natural convection was present. For a flat plate, it is generally accepted that the effects of natural convection can be neglected if the ratio $(Gr_L/Re_L^2) << 1$. The Grashof number is defined as

$$Gr_L = \frac{g\beta(T_w - T_\infty)L}{\nu} \tag{D.7}$$

The length scale, L, in equation D.7 was based on the length of the heated tube wall. Figure D.5 shows how the quantity (Gr_L/Re_L^2) varies along the tube wall for each Reynolds number studied. Unlike a flat plate, it was expected that the louvers would interfere with buoyancy driven flows, if any existed along the tube wall. Due to the louvers extending from the tube wall, it should be noted that criteria $(Gr_L/Re_L^2) << 1$ is only an approximation to the convective environment surrounding the tube wall. It was expected that the upper limit on this criteria might be slightly greater than one due to the more complicated tube wall boundary layer. However, as illustrated in Figure D.5, the quantity (Gr_L/Re_L^2) is much greater than one along the entire tube wall for Re = 230. As the Reynolds number is increased, the quantity (Gr_L/Re_L^2) drops off sharply. Even though $(Gr_L/Re_L^2) > 1$ for Re = 625 and Re = 1016, it is believed that the louvers break-up natural convective patterns, as mentioned before.

To experimentally determine effects of natural convection along the tube wall, repeatability of the tube wall heat transfer was measured for three different test section orientations. By rotating the test section into the positions illustrated in Figure D.6, the effect of gravitational acceleration on buoyancy driven flows would directly influence the tube wall Nusselt number. For Re = 1016, measurements of the tube wall Nusselt number fell within the experimental uncertainty for all test section positions as shown in Figure D.7. From the experimental results shown in Figure D.7, it can be concluded that only forced convection existed along the tube wall. However, for Re = 230, repeatability is no longer observed for the different test section positions as shown in Figure D.8. To ensure that natural convection caused the differences between the measurements shown in Figure D.8 and not the experimental uncertainty, repeatability for Re = 230 was checked for each test section position. As shown in Figures D.9-D.10, the measured tube wall Nusselt numbers for each test section position fell well within the experimental uncertainty for Re = 230.

From Figure D.8, general observations regarding natural convection could be made. First, assuming that the criteria $(Gr_L/Re_L^2) << 1$ for forced convection to dominate natural convection along the tube wall is too conservative. It is obvious that for values of $(Gr_L/Re_L^2) > 15$, corresponding to $X > 0.5$, scattering in the results of the tube wall Nusselt number begin to appear. However, it should be noted that the disagreement between measured values of the tube wall Nusselt number at different test section positions is minimal (only 5% greater than the maximum experimental uncertainty). Second, buoyancy forces contributed the highest augmentation in heat transfer rates for test section position 2. With the tube wall arranged as shown in Figure D.5 (position 2), it is quite obvious that warm fluid rising from the tube wall can be directly removed by bulk motion. Third, for test section positions 1 and 3, the tube wall Nusselt number was approximately the same. It is difficult to draw conclusions on which position 1 or 3 should have rendered larger tube wall Nusselt numbers due to the complicated geometry within the louver array. For position 3, it was impossible for buoyancy driven flows to exist and for position 1, if weak buoyancy driven flows did exist, the louvers interrupted the formation of any natural convective boundary layer. The last assumption can be further verified by studying Figures 6-8 in the paper. Figures 6-8 shows periodicity between the top, center, and bottom thermocouples existed for all the Reynolds numbers at test section position 1. If any natural convective boundary layer did form between the louvers for position 1, periodicity between the top, center, and bottom thermocouples would not fall within the experimental uncertainty as shown in Figure 8 for Re = 230. Since only weak buoyancy effects are noticed at Re = 230 and the ratio (Gr_L/Re_L^2) must be on the order of 15 before buoyancy effects begin to appear, it was assumed that only forced convection existed at Re = 625.

D.4 References

FLUENT/UNS User's Guide. 2002. Release 6.1. Fluent Inc., Lebanon, New Hampshire.

Incropera, F.P. and DeWitt, D.P. 1996. *Fundamentals of Heat and Mass Transfer*. p. 358. New York: Wiley.

Lyman, A. 2000. Spatially Resolved Heat Transfer Studies in Louvered Fins for Compact Heat Exchangers, MSME Thesis.Virginia Tech, USA.

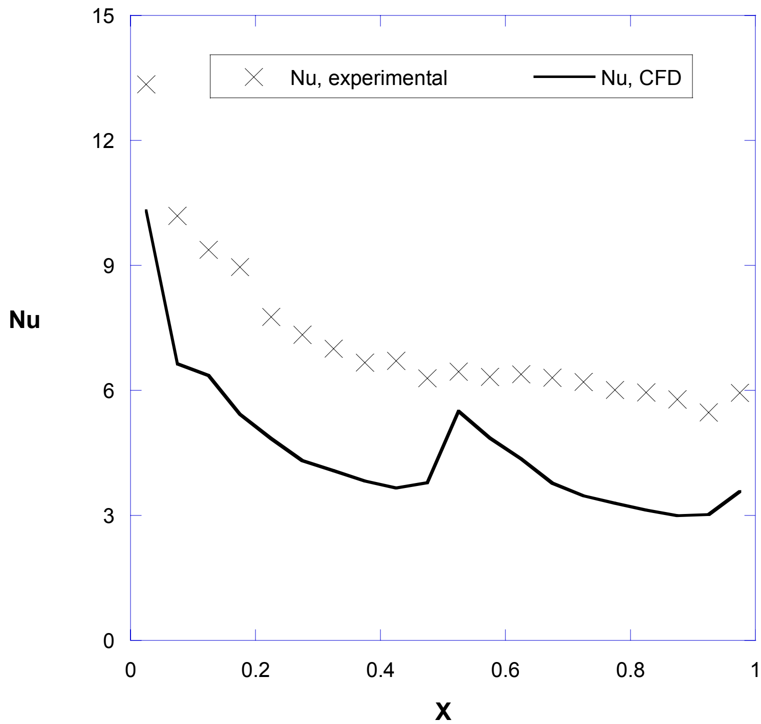

Figure D.1 Measurements and predictions of the tube wall Nusselt number for Re = 230 uncorrected for radiation losses to louver surfaces.

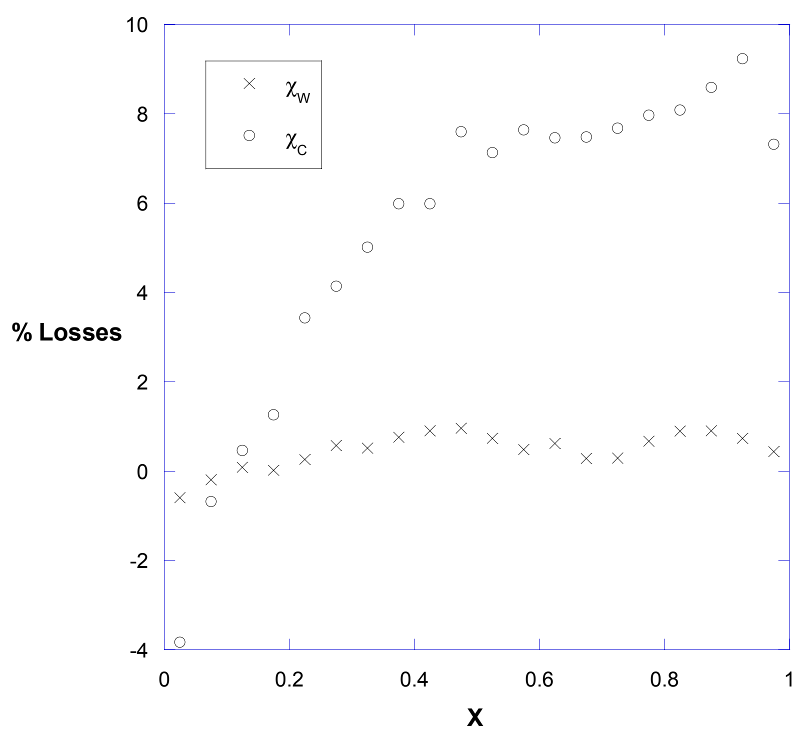

Figure D.2 Percentage of heat flux lost to the milled lexan wall and the test section's backside for Re = 230.

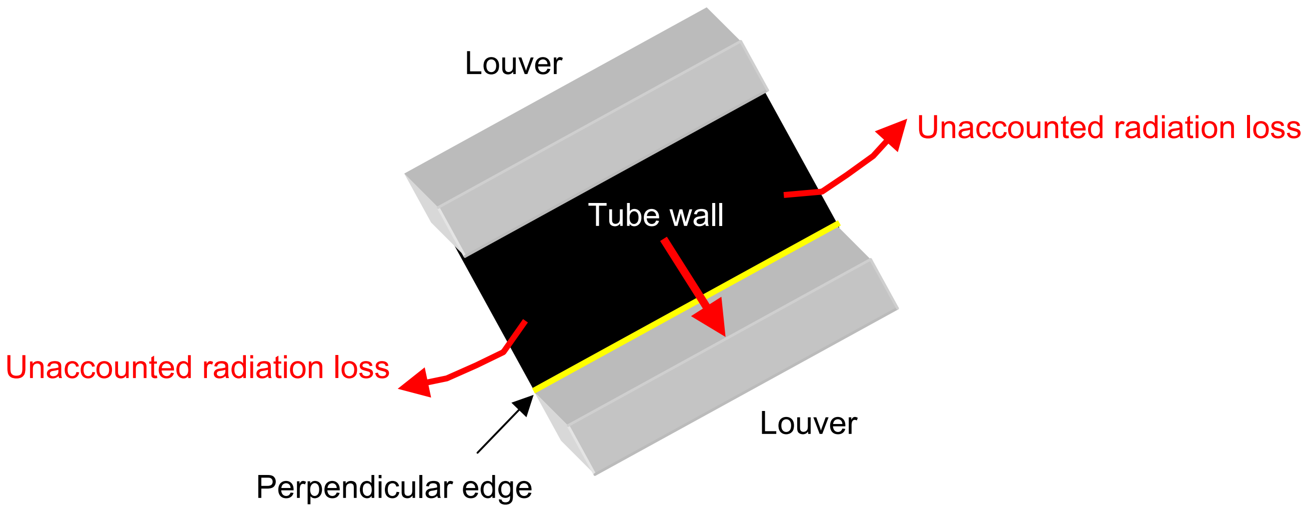

Figure D.3 Illustration of the perpendicular edge the tube wall and louvers share at the tube wall – louver junction.

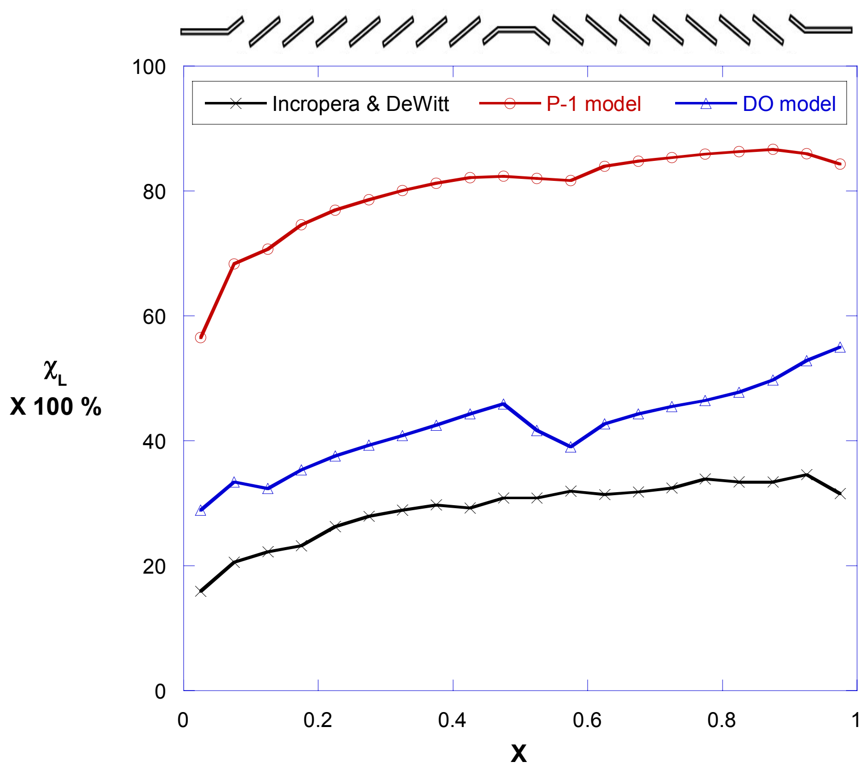

Figure D.4 Comparison of the three methods used to predict the radiation losses from the tube wall to the louvers.

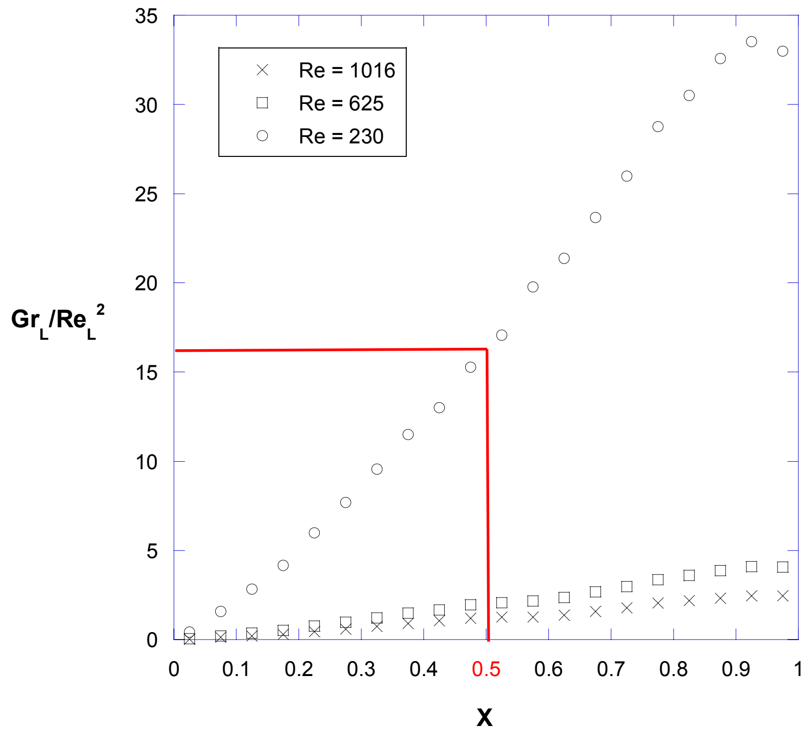

Figure D.5 Comparison of buoyancy forces to momentum forces for each Reynolds number studied. The red lines detail the value of Gr_L/Re_L^2 of where buoyancy forces were experimentally determined to affect the tube wall Nusselt number.

a) Position 1

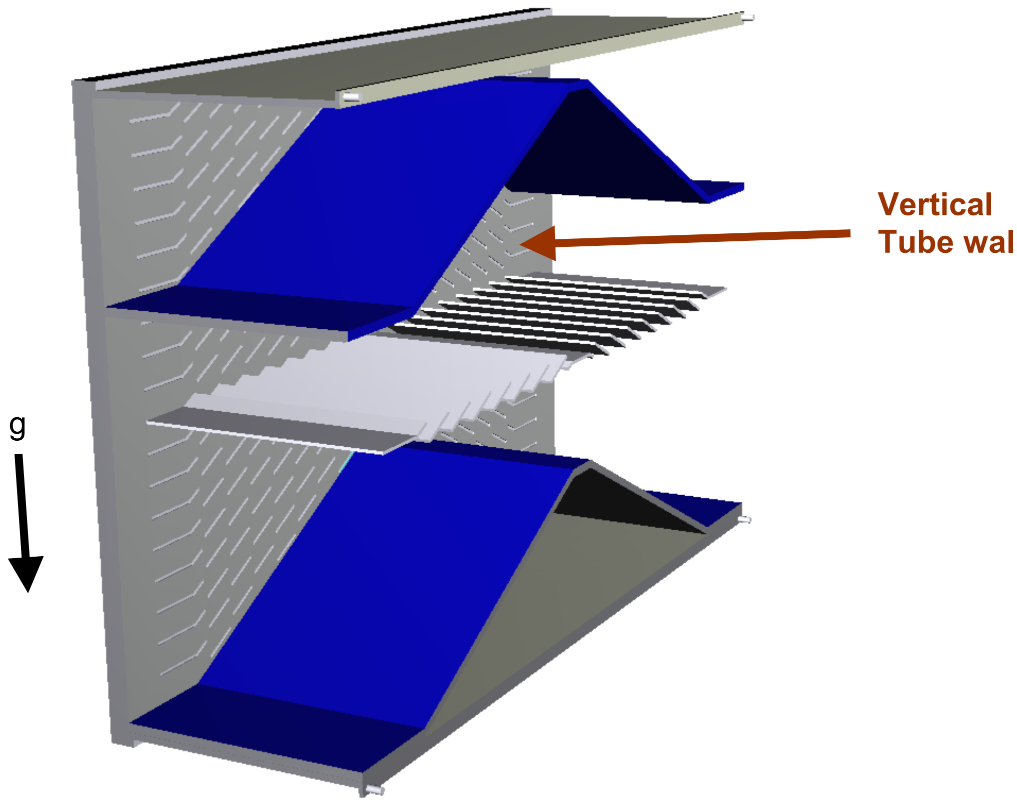

b) Position 2

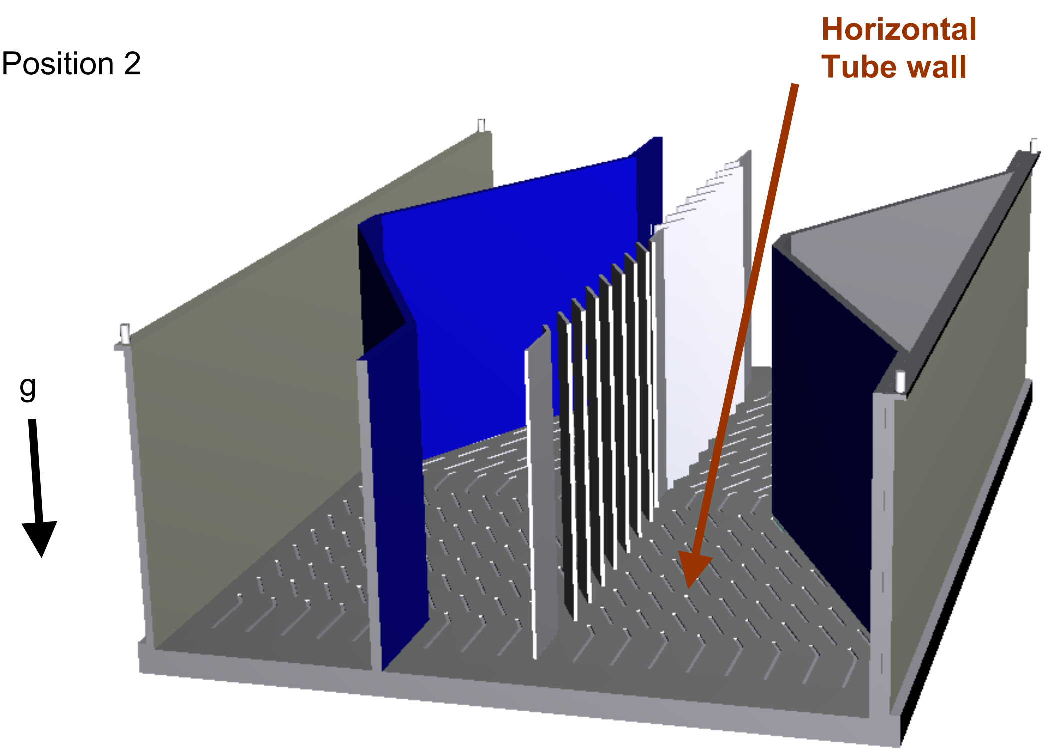

c) Position 3

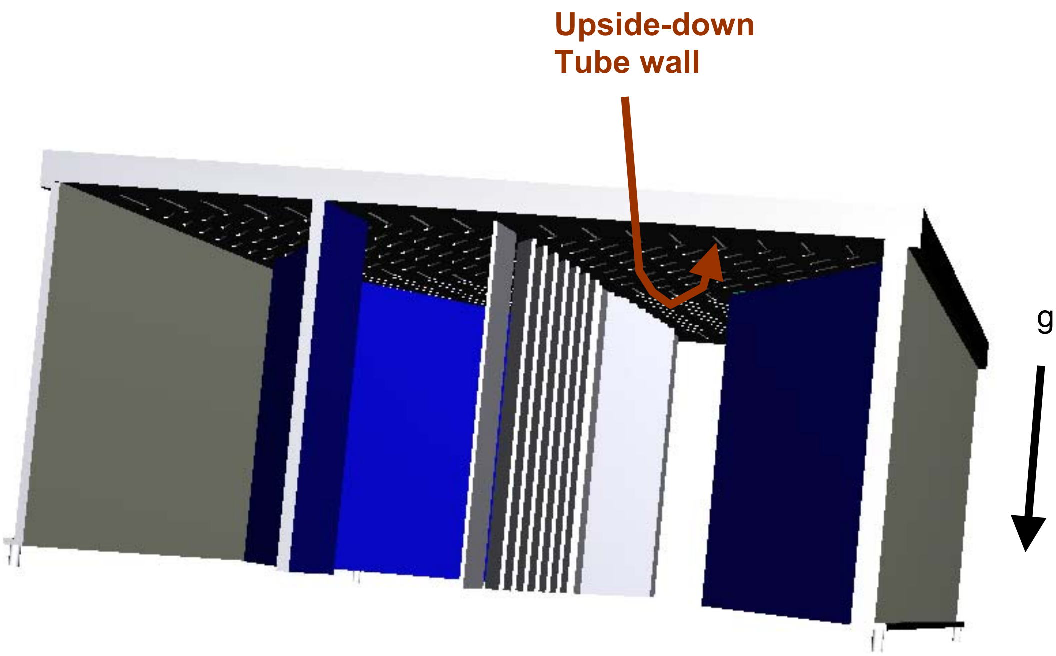

Figure D.6a-c Illustrations of the different tube wall positions tested with respect to gravitational acceleration.

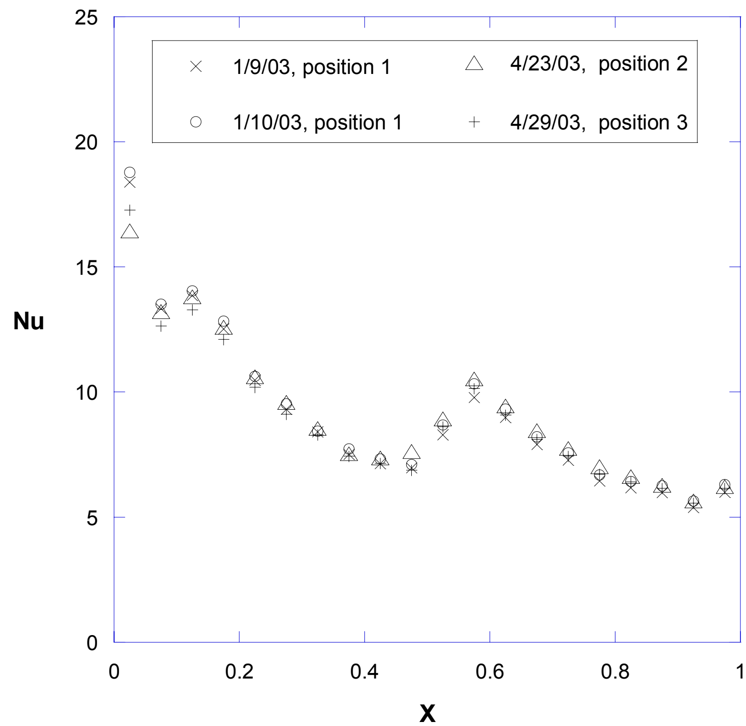

Figure D.7 Repeatability of the tube wall Nusselt number for Re = 1016.

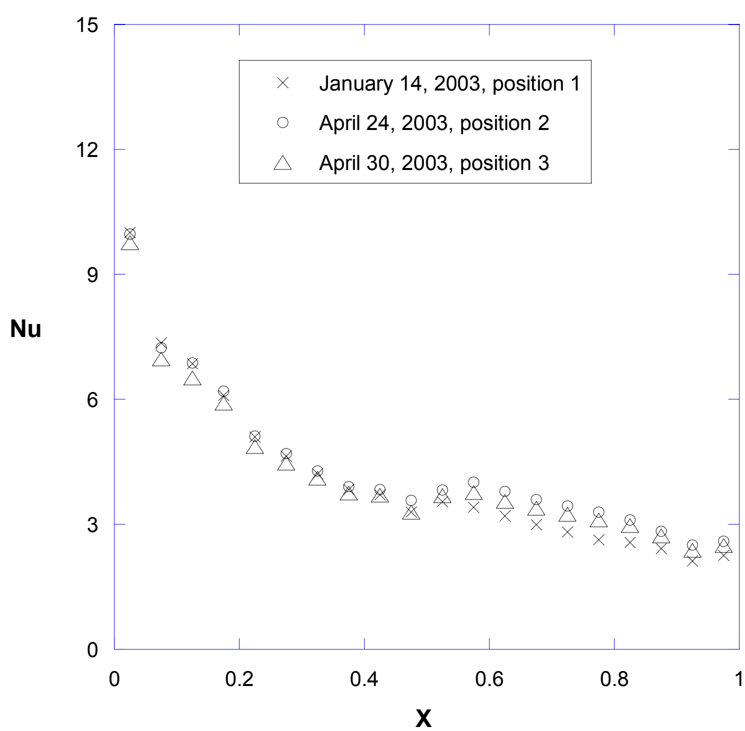

Figure D.8 Repeatability of the tube wall Nusselt number for Re = 230.

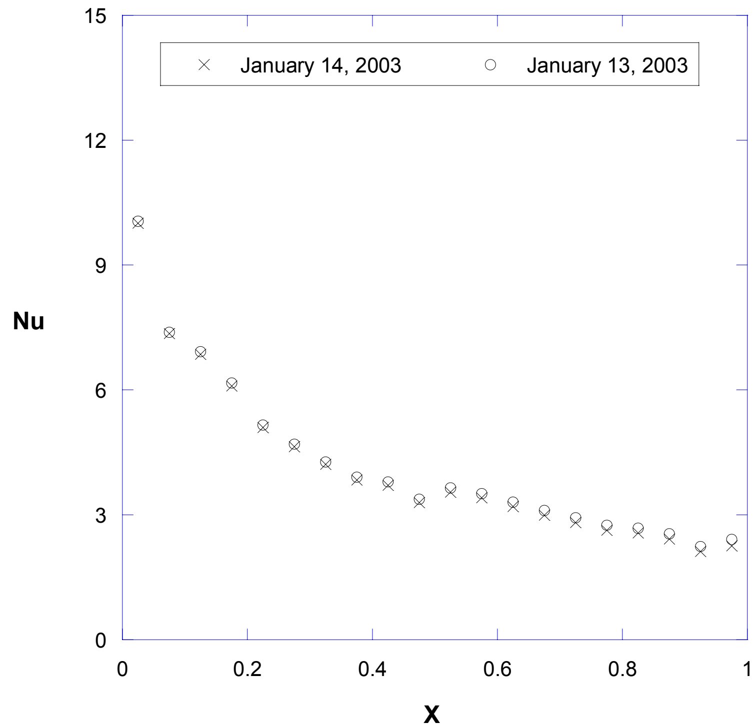

Figure D.9 Repeatability of the tube wall Nusselt number for Re = 230 and test section position 1.

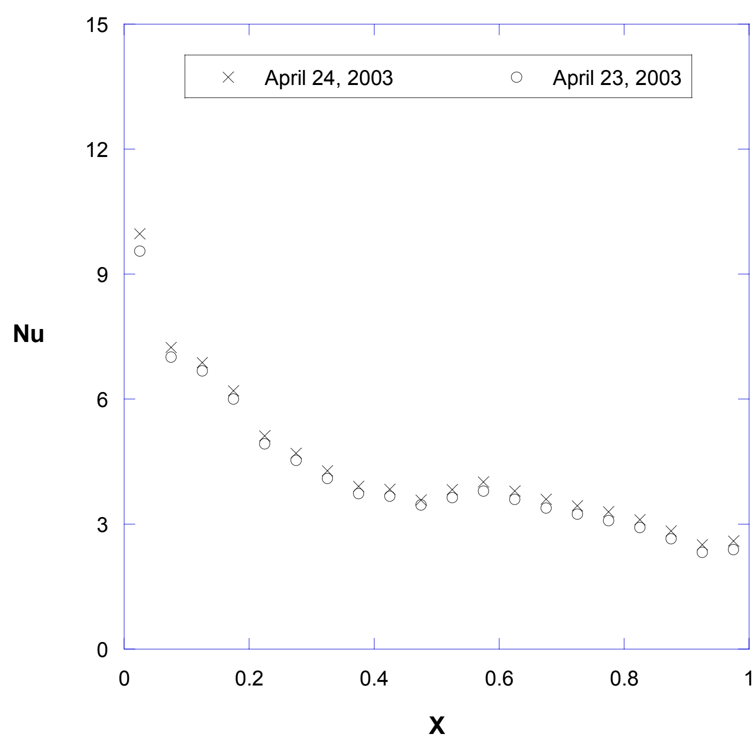

Figure D.10 Repeatability of the tube wall Nusselt number for Re = 230 and test section position 2.

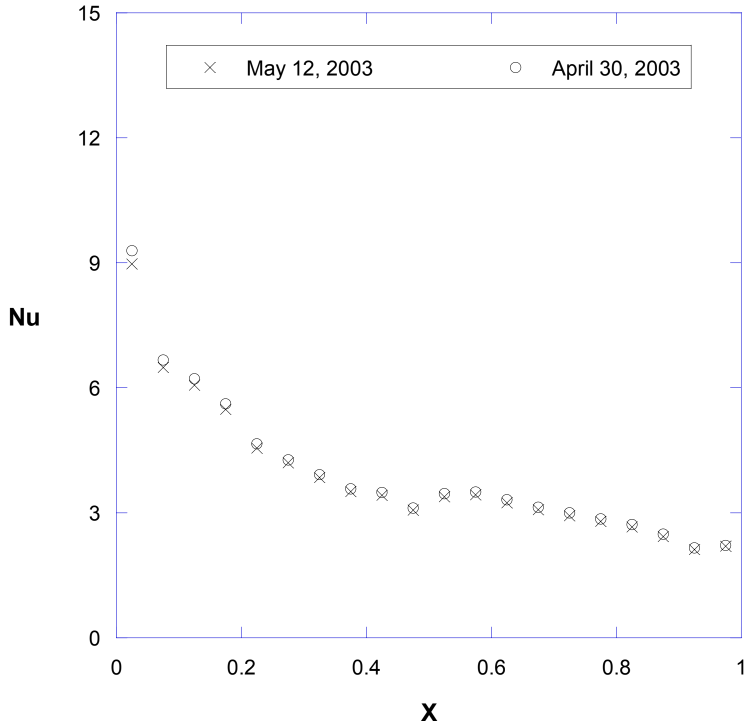

Figure D.11 Repeatability of the tube wall Nusselt number for Re = 230 and test section position 3.

Appendix E

Additional Computational Results

Experimentally, the heat transfer coefficients for the isothermal tube wall could not be measured for reasons already discussed in Appendix B. However, the heat transfer for an isothermal tube wall was computationally predicted. This appendix compares the tube wall Nusselt number for both the isothermal and constant heat flux tube wall. Predictions of the velocity and thermal boundary layer profiles for the constant heat flux boundary are also discussed.

As mentioned in the paper, the computational simulations of the tube wall consisted of an unstructured grid on which temperature gradient adaptations were performed. The unstructured data array exported from the tube wall was interpolated onto a 2-D, structured grid in MatLab 6.5. Comparisons of the Nusselt number for both the isothermal and constant heat flux tube wall in this section are based on pitch-wise averages of the data from the structured grid. For the isothermal case, pitch-wise averages of the tube wall surface heat flux were taken along Y´ for the entire tube wall. Similarly, for the constant heat flux case, pitch-wise averages of the tube wall surface temperature were calculated. Figures E.1-E.3 illustrates the pitch-wise average tube wall Nusselt numbers as well as that of the flat plate (equation B.1) for the two boundary conditions. Figures E.1-E.3 also indicate that the heat transfer performance of the tube wall is dependent on the boundary condition applied. For the tube wall subjected to a constant heat flux boundary condition, the heat transfer results were approximately 23% greater than the isothermal case for Re = 1016. Similarly, it was predicted that the tube wall's heat transfer was 36% greater for the constant heat flux boundary condition as compared to that of the isothermal case for Re = 230. The higher rates in heat transfer for the constant heat flux tube wall suggests that a thinner boundary layer exist for the constant heat flux tube wall as compared to the isothermal tube wall.

To further explain the higher rates in the tube wall heat transfer for the constant heat flux boundary condition, consider two flat plates: the first flat plate is subjected to heating caused by a constant heat flux and the other is heated isothermally. For the plate subjected to a constant heat flux, the temperature gradient at the wall is constant along the entire length of the plate. However, for the isothermal plate the temperature gradients at the wall decreases along the length of the plate. In order for the temperature gradients at the wall to decrease along the length of the plate, the thermal boundary layer must thicken to cause gradients near the wall to decrease. While developing, the dependence of the isothermal plate's surface heat flux on the streamwise position of the plate, results in a thicker thermal boundary layer than the plate subjected to a constant surface heat flux. Now consider the tube wall. In general, the basic heat transfer trend is the same for the tube wall subjected to both boundary conditions; larger heat transfer rates are predicted for the constant heat flux boundary condition as compared to the isothermal tube wall. However, since the thermal boundary layer is thicker for the isothermal tube wall, augmentation at the entrance, reversal, and exit louver as well as at the leading edges of the straight louvers is locally more pronounced. As an example, consider Figures E.1-E.3 and compare the spikes in the tube wall Nusselt number at the leading edges of the louvers for both boundary conditions. It is obvious that the isothermal tube wall is more sensitive to thermal field mixing. However, shortly downstream of the mechanism that causes mixing (whether it is a louver's leading edge, the reversal louver, etc.), the tube wall Nusselt number falls below the predicted values of that of the constant heat flux tube wall.

For all Reynolds numbers studied the average tube wall heat transfer for both the constant and isothermal tube wall is shown in Figure E.4. In addition to tube wall results, the expected averaged heat transfer for a flat plate subjected to the two boundary conditions is also plotted in Figure E.4. The difference in Nusselt number for a flat plate subjected to both boundary conditions is approximately 26% for all Reynolds numbers. For both boundary conditions, the averaged tube wall Nusselt number is much higher than that of the flat plate. Previously discussed in the paper were mechanisms such as the leading edge vortex and separation which augment tube wall heat transfer. To supplement the thermal and velocity fields already presented in the paper, boundary layer profiles were taken between straight louvers shown as blue dots in Figure E.5. Boundary layer profiles were taken between straight louvers to avoid the separation effects illustrated in

Figures 13-15 in the paper. From Figure E.5, it is obvious that the presence of the louvers maintain a thinner thermal and velocity boundary layer than that of the flat plate.

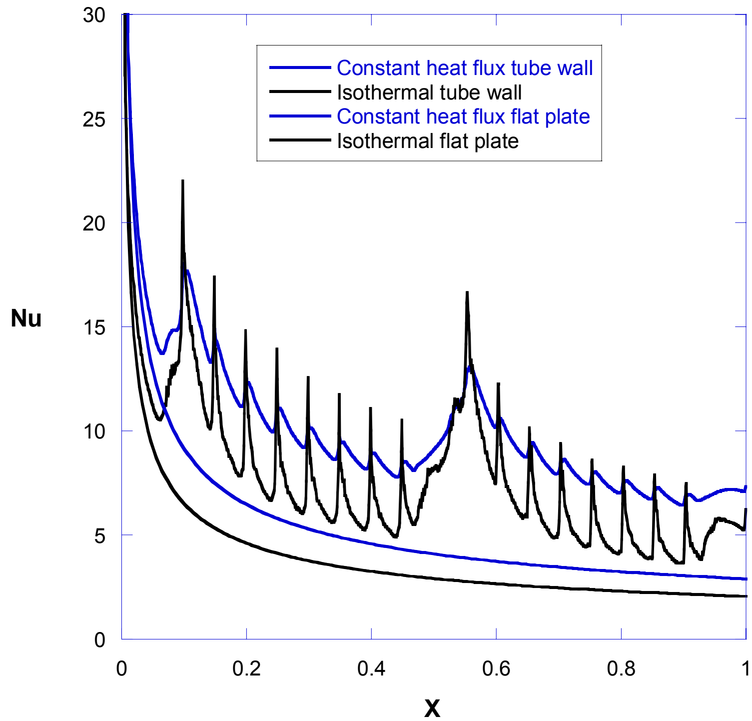

Figure E.1 Comparison of pitch-wise averaged tube wall Nusselt numbers compared to that of the flat plate for both the isothermal and constant heat flux boundary conditions for Re = 1016.

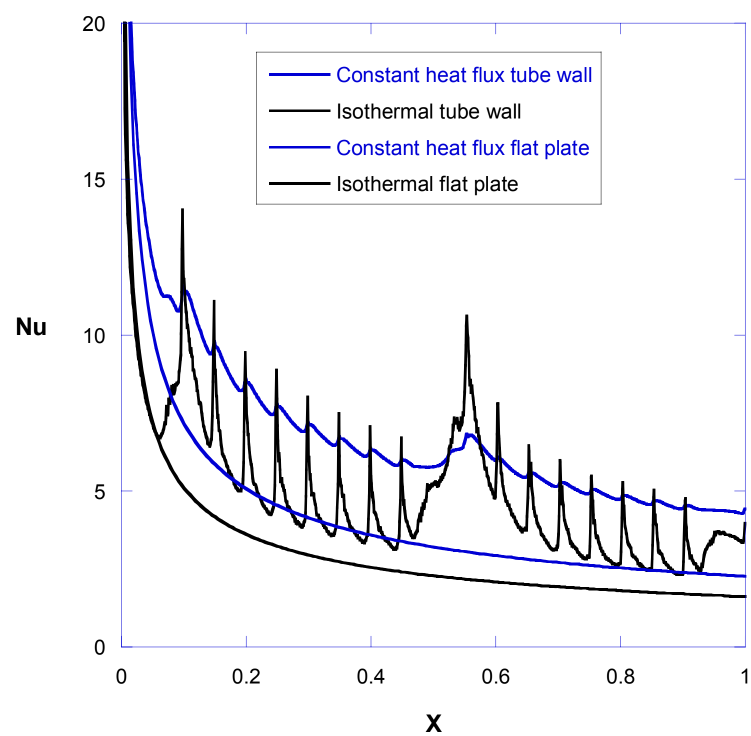

Figure E.2 Comparison of pitch-wise averaged tube wall Nusselt numbers compared to that of the flat plate for both the isothermal and constant heat flux boundary conditions for Re = 625.

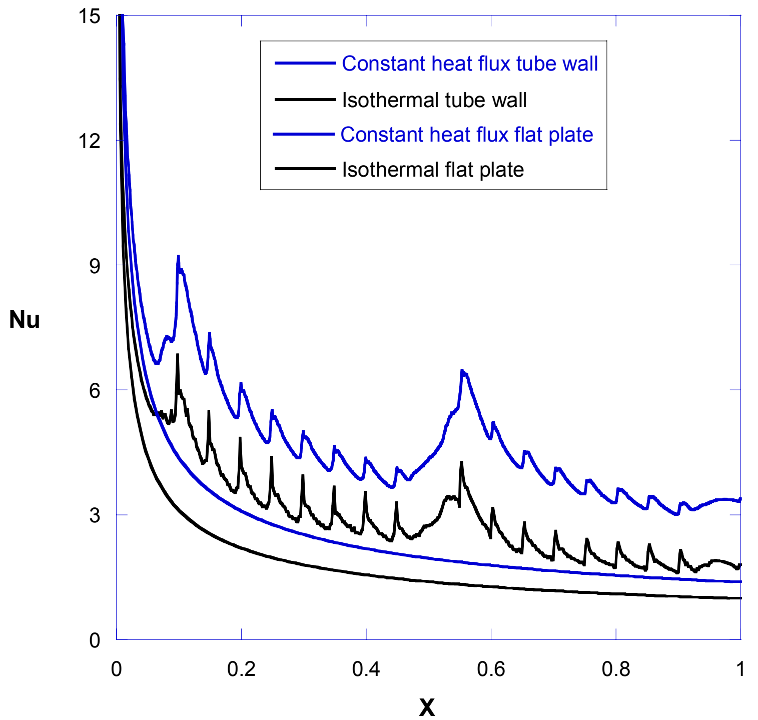

Figure E.3 Comparison of pitch-wise averaged tube wall Nusselt numbers compared to that of the flat plate for both the isothermal and constant heat flux boundary conditions for Re = 230.

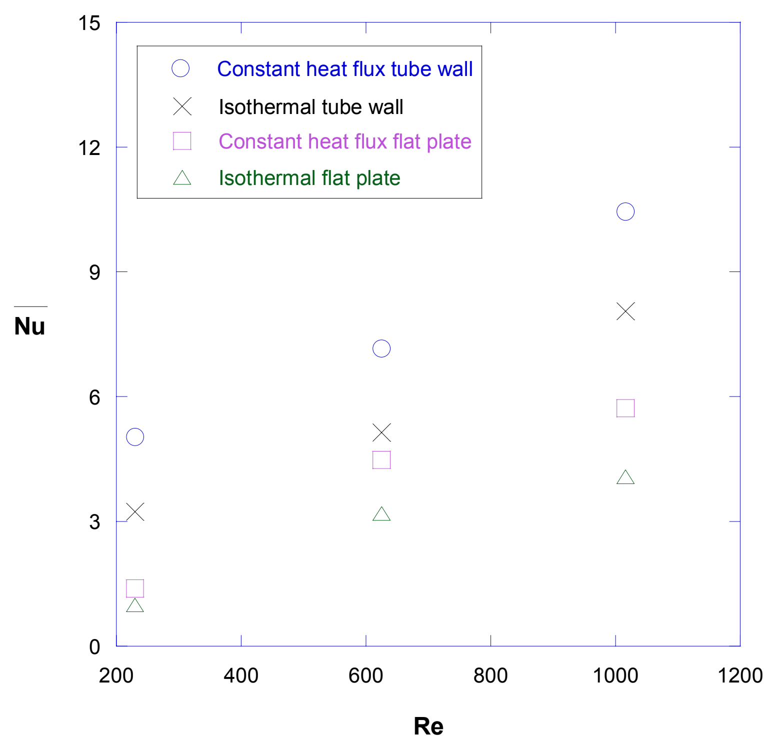

Figure E.4 Predictions of the averaged tube wall Nusselt number compared to that of the flat plate as a function of Re for both the isothermal and constant heat flux boundary conditions.

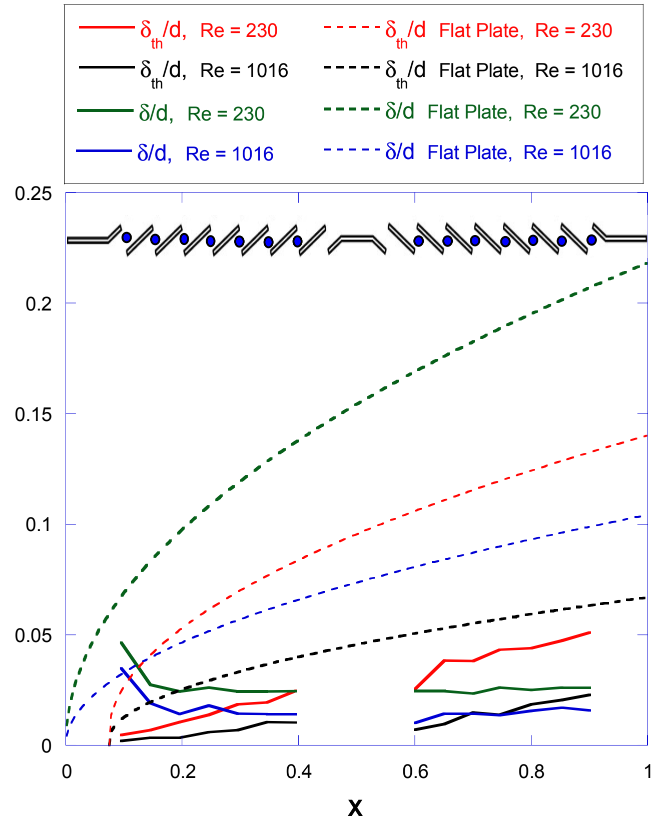

Figure E.5 Predictions of the velocity and thermal boundary layer thicknesses between straight louvers compared to a flat plate for the constant surface heat flux boundary condition.

Appendix F

Summary of Findings and Recommendations for Future Work

Both experimental and computational methodologies aided in the investigation of the heat transfer that occurs along the tube wall in compact heat exchangers. The collections of data presented in this study are baseline results of tube wall heat transfer. With the aid of a scaled test section, an idealization of the louver-tube junction was experimentally built. Since true heat exchange at the tube wall occurs for mix boundary conditions, initial experiments were to be carried out for both the isothermal and constant heat flux tube wall. However, experimental control of the tube wall's surface heat flux became impractical and experimental studies of the heat transfer occurring along the tube wall were only carried out for the constant heat flux boundary condition. Greater resolution of the heat flux removed by convection was obtained by experimentally minimizing unwanted heat losses. The integration of two guard heaters into the experimental design reduced the temperature potential between the tube wall and the surroundings. In this manner the majority of conduction losses were minimized. However, for radiation exchange to be adequately accounted for within the test section, numerical predictions of the radiation losses from the tube wall was required.

In addition to experimental tests, a three-dimensional mesh of the tube-louver geometry was created using a commercially available CFD code. Relatively good agreement between the experimentally measured and predicted heat transfer results was achieved. When compared to a flat plate, both measurements and predictions showed that the presence of louvers can augment heat transfer up to 3 times. Unlike a flat plate, the tube wall heat transfer is strongly influenced by: 1) vortices created at the leading edges of the louvers and 2) separation within the vicinity of the flow reversal louver. Leading edges of the louvers served to thin the thermal boundary layer by brining cooler bulk flow to the tube wall. These vortices help augment heat transfer after the flow becomes louvered directed. As the flow moves downstream and meets the reversal louver, the flow was predicted to separate. As separation occurs, it was determined that the surrounding thermal field is considerably mixed with cooler bulk flow. Due to the mixing that separation causes, development of the thermal boundary layer after the reversal louver starts from a thinner boundary layer thickness than if the reversal louver was not present. Therefore, the heat transfer that occurs for the entire second half of the tube wall is dependent on the fluid structures that break up the boundary layer at the reversal louver. Although computational results of separation are believed to be over predicted, experimental measurements follow a less pronounced, but similar trend within the vicinity of the reversal louver.

From the baseline data presented in this study, it is possible to project new augmentation strategies that could potentially increase the heat transfer occurring along the tube wall. As mentioned earlier, the leading edges of the louvers augment tube wall heat transfer by introducing the tube wall to cooler bulk flow. To transport a greater quantity of cooler bulk flow to the tube wall, redesign of the straight louvers should be considered. Currently, the straight louvers are rectangular in design. If the louvers were redesigned with a three-dimensional curve, such that the flow from the free stream is forced to be projected towards tube wall, significant thinning of the tube wall's thermal boundary layer could occur. Figure F.1 illustrates a possible design for a curved fin. Since the louvers are punched from metal, manufacturing processes would only have to adapt to a newly shaped punch to produce such a louver.

The separation effects mentioned in this study, particularly around the reversal louver, suggests that additional reversal louvers might also augment tube wall heat transfer. Instead of allowing the flow to become louver directed, a reversal louver could replace the straight louvers at the positions where the flow becomes nearly louver directed. As an example, consider Figure F.2, which illustrates a tube wall with three reversal louvers. With this design, it is expected that tube wall's boundary layer would be re-set three times along the tube wall. However, employing this design will surely increase the pressure drop through the louver array.

With new augmentation techniques, a method for spatially determining the tube wall heat transfer will be needed. As mentioned in Appendix B, taking IR camera pictures of the tube wall from across the channel was impossible due to shadows created by the louvers. If additional three-dimensional geometry is ever added to the fin such as the before mentioned curve, vortex generators, etc., even more blockage of the tube wall's image would be present. Therefore, it is suggested that images of the temperature gradients along the wall be obtained from behind the tube wall's heaters. Careful consideration of the conduction losses would have to be taken in to account if the conduction guard heater is removed. Images of the tube wall's temperature gradient should be taken at test section position 2. In this manner, natural convection will not interfere with the tube wall's backside (the imaging surface) and only weak buoyancy forces will be present for Re = 230 along the tube wall.

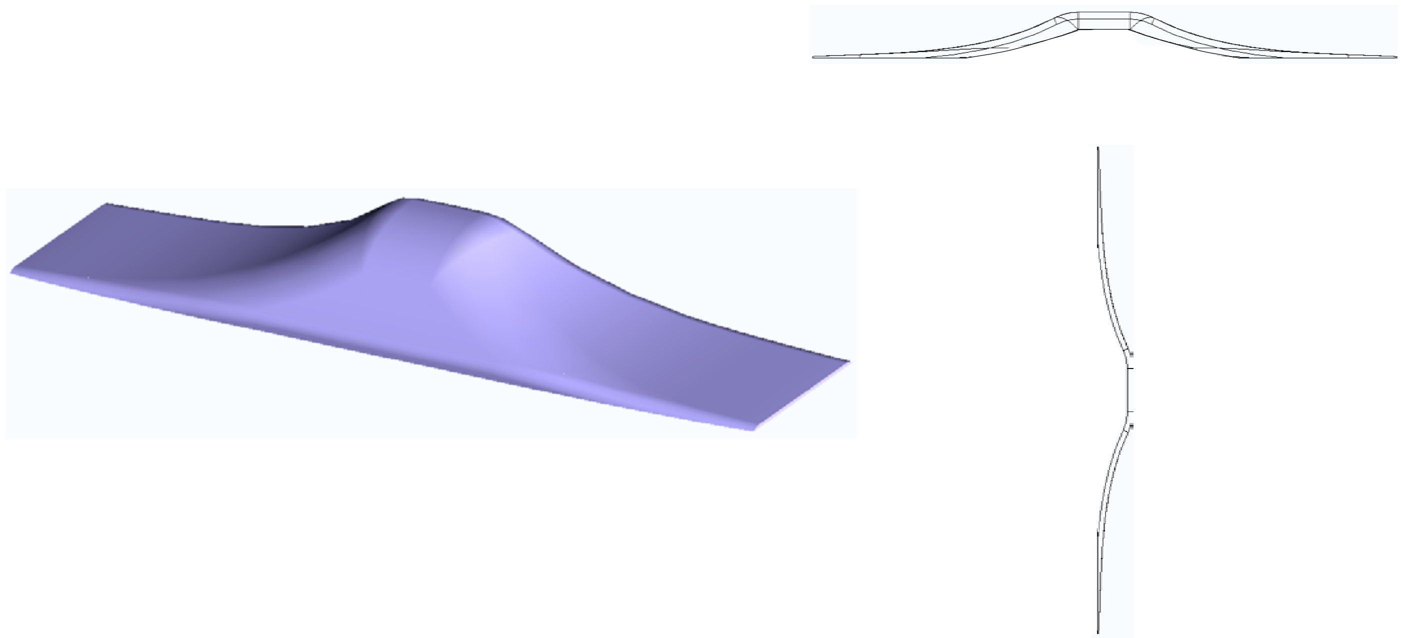

Figure F.1 Illustration of possible fin concept that could augment tube wall heat transfer.

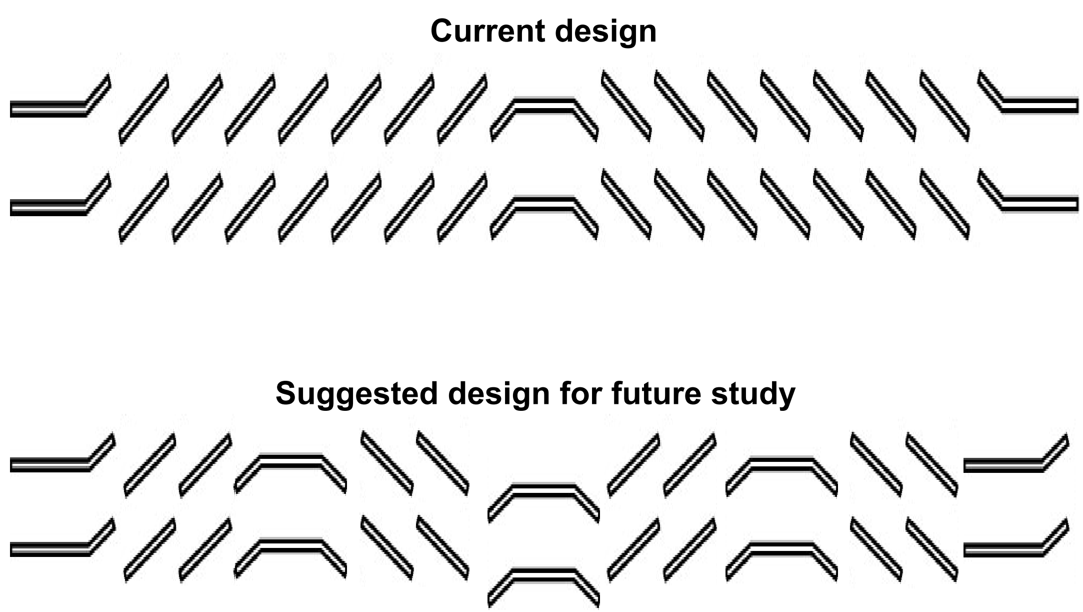

Figure F.2 Comparison of the current and the suggested fin design including three flow reversal louvers which could possibly augment tube wall heat transfer.

Appendix G

Vitae

Christopher P. Ebeling was born on October 29, 1979 in Passaic county, New Jersey. Since an early age, mechanical devices intrigued Christopher. Throughout his early education at St. Leo's grammar school and his high school education at Don Bosco Preparatory High School, Christopher constructed dirt bikes, catapults, cannons (one in particular was able to launch a potato 200 ft), a glockenspiel, and a two-rank pipe organ. Interests in mechanical objects lead Christopher to pursue a degree in mechanical engineering at Gannon University in Erie, PA. At Gannon University, Christopher excelled in several subjects, especially heat transfer and music. Through an internship with General Electric, Christopher gained valuable insights on the cooling systems of locomotives. At the same time he also studied pipe organ performance at St. Paul's Episcopal Cathedral in Erie, PA and gave frequent performances to the music classes at Gannon University. This unusual combination of interests (engineering and music) allowed Christopher to incorporate creativity into any engineering project he undertook. After receiving his B.S. degree in mechanical engineering from Gannon University, Christopher decided to attend Virginia Tech in June, 2000 for graduate studies. On Friday 13, 2003, Christopher successfully defended his thesis and graduated from Virginia Tech with his Master's of Science degree in mechanical engineering. His future plans include a six month internship with BMW in Munich, Germany before returning to Virginia Tech to pursue a Ph.D in mechanical engineering.